Improving OTM mechanical properties by controlling the pore architecture

Jordi Seuba Torreblanca

THÈSE

Pour obtenir le grade de

Docteur

Délivré par l'**Université Montpellier 2**

Préparée au sein de l'école doctorale **Sciences Chimiques Balard**
Et de l'unité de recherche **LSFC, Cavaillon**

Spécialité: **Chimie séparative matériaux et procédés**

Présentée par **Jordi SEUBA TORREBLANCA**

Improving OTM mechanical properties by controlling the pore architecture

Soutenue le 10 Décembre 2015 devant le jury composé de

Mr. Paolo COLOMBO	Pr.	Univ. of Padova (Italie)	Rapporteur
Mr. Sylvain MEILLE	Pr.	Univ. de Lyon, Villerbaunne	Rapporteur
Mr. Christian GUIZARD	Pr.	IEM, Montpellier	Directeur
Mr. Adam J. STEVENSON	Dc.	Saint-Gobain/CNRS,Cavaillon	Co-encadrant
Mr. André AYRAL	Pr.	IEM, Montpellier	Président
Mr. Sylvain DEVILLE	Pr.	Saint-Gobain/CNRS, Cavaillon	Invité

Abstract

ENGLISH

Macroporous ceramics are widely used in applications such as filtration, thermal insulation, scaffolds for tissue engineering, Solid Oxide Fuell Cells, and Oxygen Transport Membranes. They must combine mechanical stability with at least one other functional property such as high permeability, low thermal conductivity, or biocompatibility. However, strength is usually increased by decreasing the total pore volume even though this may degrade the other functional properties.

In the present work we used ice-templating as a tool to produce anisotropic macroporous structures that maximize simultaneously permeability and strength. First, we identified the main experimental parameters that control pore volume, size, and morphology and linked processing with microstructure. Second, this understanding was applied to characterize the mechanical behavior of unidirectional porous materials and subsequently link microstructure with mechanical performance.

We investigated the effect of porosity (between 50% and 80%), pore size (3μm - 20μm), and pore morphology (lamellar and honeycomb) on compressive strength and reliability. The results were compared with isotropic porous materials with equivalent pore volume and size prepared by organic burn-out. The maximum strength (286 MPa) was achieved in the less porous ice templated samples, with the smallest pore size, independently of the pore morphology. Additionally, we show that the honeycomb out-of-plane model derived by Gibson and Ashby can be applied to describe the compressive behavior of unidirectional porous materials. Furthermore, we found that the suitability of the model is restricted to structures where buckling is the dominant failure mode.

We also analyzed the applicability of Weibull analysis to unidirectional macroporous materials prepared by ice-templating. We assessed the effect of the same pore descriptors (volume, size, densification of the walls, and morphology) on Weibull modulus and the subsequent probability of failure. We found a remarkable correlation between wall thickness reduction and increase in reliability in perfect agreeement with the *weakest link hypothesis*. The highest Weibull modulus (m = 13,2) was obtained for the samples with the smallest and narrowest wall thickness distribution.

Third, we investigate the gas flow behavior in ice-templated materials. The maximum permeability (k_1 =1,39$\times 10^{-11}$ m^2) was exhibited by samples with the highest total pore volume (72%) and pore size (20,0 μm). However, we demonstrate how it is possible to achieve a similar permeability (k_1 =1,09$\times 10^{-11}$ m^2) at 54% pore volume by modification of the pore morphology. We evaluate the applicability of Ergun and capillary model in the prediction of permeability of unidirectional porous materials.

Fourth, we applied all the knowledge gathered processing ice-templated monoliths to develop a new system to ice-template tubes (length 150 mm and external diameter 10 mm) with controlled pore volume (49,1% - 69,4%), pore size (3,3 μm - 14,6 μm), and tube thickness (1,2 mm - 2 mm). Finally, we characterized the mechanical and gas flow behavior of ice-templated tubes to determine the structural parameters governing strength and permeability.

By performing this detailed characterization and validating appropriate models, we hope to provide the information necessary to deterministically target unidirectional porous structures to specific applications.

Introduction

Different applications require porous materials with high strength and permeability. However, the combination of both properties is difficult to achieve, and permeability is usually enhanced by increasing the total pore volume, even though increasing porosity decreases strength.

One example of this trade-off between strength and permeability is found in asymmetric oxygen transport membranes (OTMs), which are shown and described in Fig. 1. After our experience as an active partner in several European projects (HETMOC and CARENA) dealing with OTMs, we realized that the limiting factor of this technology is the performance of the porous mechanical support. These supports must exhibit high permeability to provide high oxygen flux, and high strength to withstand thermomechanical stresses from sealing and operating conditions. In this work, we used the problems of current generation of OTM supports as motivation and inspiration to better understand the role of microstructure on strength and permeability, so that we may enable new, specifically tailored pore architectures to simultaneously improve both properties.

Morphological parameters such as pore size, shape, and tortuosity can become crucial to maximize the gas flow while maintaining high strength. In principle, a significant improvement in strength can be achieved by engineering anisotropic structures to mechanically reinforce the direction of the main stress and simultaneously reduce the resistance to air flow [1].

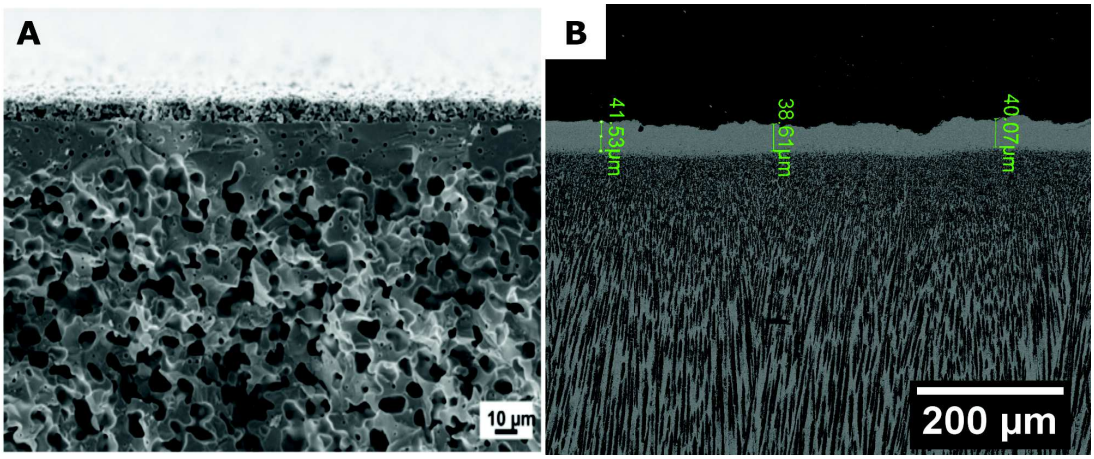

Figure 1: SEM images of two asymmetric membranes processed by different techniques. The dense layer on top provides the required selectivity and its performance can be maximized reducing its thickness. However, when the dense layer is too thin it is necessary to attached a porous support to provide mechanical stability. This porous substrate also has to be permeable enough to allow the oxygen be released out of the membrane. A) The porous support was obtained by pore formers and consequently there is no control on the pore orientation. The content of pore formers has to be quite high to overcome the percolation limit and ensure a minimum permeability. The dense layer was made with the same material as the support and was obtained by dip-coating [2]. B) Porous and dense support were obtained in one step using a modified ice-templating. The porosity created in this technique is typically unidirectional, so the pore volume required to reach the percolation threshold is lower.

In this work we used ice-templating to obtain unidirectional porous materials with accurate control over pore volume, size, and shape. The technique is based on the growth of solvent crystals in a colloidal suspension to tailor the final porous structure and it is described in Fig. 2. Ice-templating allows a quasi-independent control of structural parameters like total pore volume, pore size, and pore morphology. This flexibility will be used to elucidate the specific impact of each structural parameter on the strength and permeability. We took advantage of the knowledge and experience of the LSFC in ice-templating to quickly and reproducibly create samples with architectured porous structures.

Although, the mechanical characterization of ice-templated materials has been extensively reported [3], a systematic analysis describing the effects of microstructural parameters on mechanical properties in a large porosity range is still missing. Similarly, the literature on reliability of porous ceramics is scarce, and the very few articles published rarely try to understand the phenomena and simply report the results. This lack of information is even more severe in the case of permeability, where very few articles have been published relating the microstructure of ice-templated materials and gas flow [4] [5]. **The main objective of this work is to identify and understand the structural parameters that govern the mechanical and gas flow properties on unidirectional porous materials and provide the information necessary to target microstructures to specific applications that require strength and permeability**. These applications include OTM, SOFC, filtration, and heterogeneous catalysis.

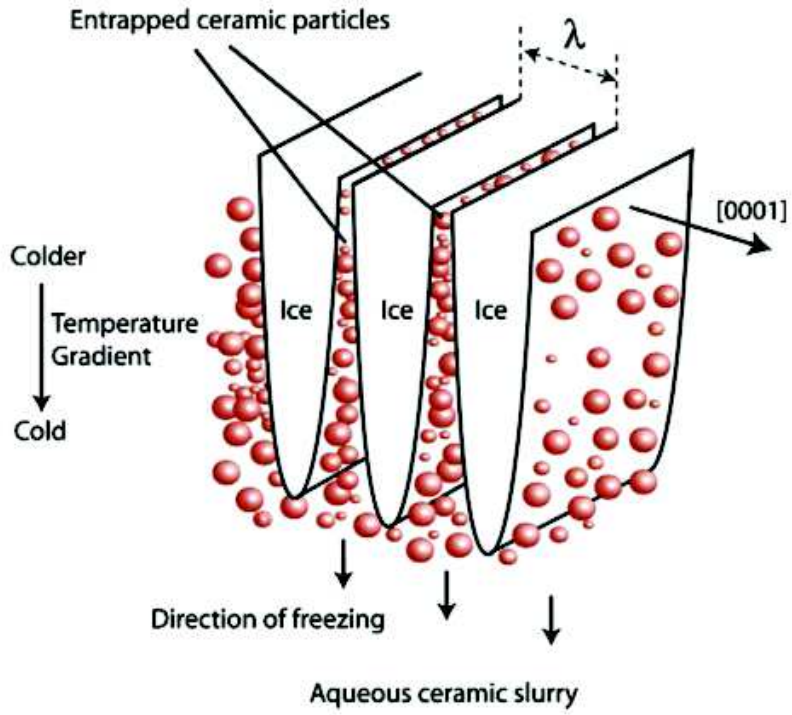

Figure 2: Schematic of the ice-templeating process [6].

This manuscript is organized in seven chapters. The first chapter is a brief literature review on porous ceramics, ice-templating, and OTMs. Chapter 2 details the experimental procedure used to process and to characterize the different types of samples. The third chapter explores the main experimental parameters controlling the different aspects of pore morphology (pore volume, pore size, pore shape, and wall thickness). This microstructural characterization will be used in the next chapters to then link microstructure with properties. Chapter 4 describes the mechanical behavior of unidirectional porous materials and the results will be compared with the isotropic microstructures obtained by other techniques. We realized that the strength is highly dependent on the pore structure, and consequently it can be enhanced designing structures which failure is buckling-dominated instead of bending-dominated. Further, this chapter also reports a complete study on reliability of porous materials, a property rarely characterized but with capital importance in industrial application. We control the reliability of porous structures adjusting the wall thickness distribution. The effect of the same microstructural parameters on air permeability will be discussed in chapter 5. Controlling pore size and shape we have been able to process samples with high permeability and mechanical resistance. Most of the applications previously mentioned require a tubular configuration to maximize the production per area. Chapter 6 describes a new method to produce ice-templated tubes and reports their strength and air flow. Finally, the seventh chapter summarizes the main conclusions and proposes a list of important topics that could follow this work.

Contents

Chapter 1

Literature Review

Contents

1.1 Porous ceramics

Much of the literature on porosity in technical ceramics was considered it to be a defect compromising mechanical stability [7]. However, in certain applications such as filters, insulators or catalytic supports, pores enable functionality and are introduced deliberately. Recent progress in fabrication procedures has considerably widened the range of morphologies and properties achievable, resulting in an expanding range of applications. The introduction of porosity is therefore an extremely versatile and powerful tool for greatly extending the range of properties offered by a ceramic component [8], Fig. 1.1.

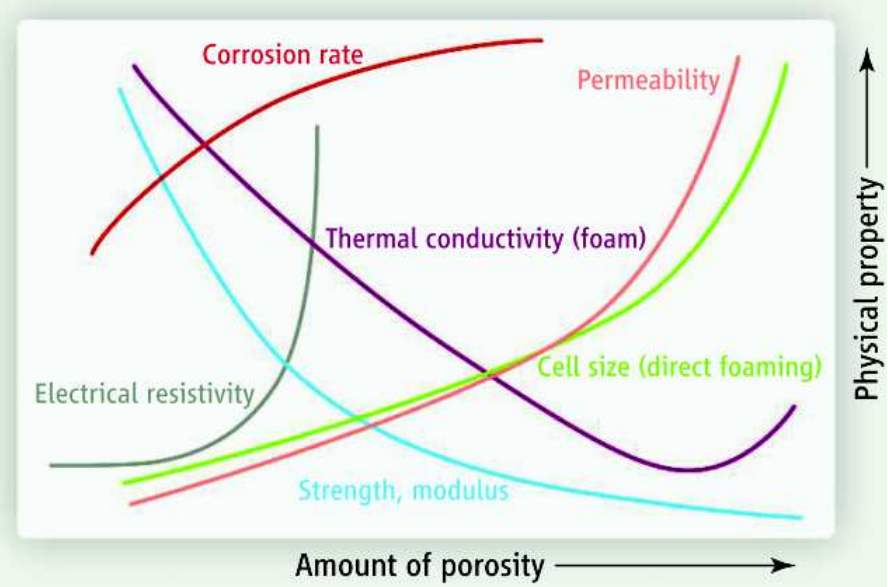

Figure 1.1: A wide range of physical properties can be achieved by changing the amount of porosity through processing [8]

1.1.1 Structure vs. Properties

Materials with a porous structure are common in nature. Their design efficiently optimizes characteristics such as the strength-to-density and stiffness-to-density ratios. Moreover, there is the matter of the morphology. Some porous materials, such as wood and cork, have prismatic and unidirectional honeycomb-like cells, while others, such as trabecular bone and sponges have randomly oriented polyhedral cells [9] [10]. In all cases, their properties are strongly linked to the microstructure (optimized during thousands of years) and the material.

It is difficult to summarize the effect that porosity can have in all the properties due to the complexity and the different nature of the interactions. However, it is possible to highlight some general trends. A simple and broad consideration is that there are three levels of porosity dependance increasing in complexity Table 1.1 [11]:

Level of dependence	Properties
I) No dependence	Lattice parameter, thermal expansion coefficient, emissivity
II) Amount of porosity	Density, dielectric constant, heat capacity
III) Amount and character of porosity	Mechanical properties, electrical and thermal conductivity, surface area, etc

Table 1.1: Impact of porosity on different properties

At the simplest level, there are properties that have no dependency on porosity. These depend only on atomic scale phenomena and are not affected by the long range interference of the pores. The second category consist of those properties dependent only on

the amount, and not the character of porosity. Such properties can be characterize using a rule of mixtures for the pore volume (P) and the solid phase (1-P):

$$X = X_s(1 - P) + X_pP \tag{1.1}$$

where X is the property of the porous material, X_s the same but referred to the solid, and X_p the property of the pore phase (usually zero, but there are some exception like the refractive index or the dielectric constant). The last category is the largest, most complex and important category that consists of those properties dependent on both the amount and the character of porosity. Properties like strength, elasticity, permeability, etc. require a more exhaustive description of the structure to fully characterize the material [12]. In this case, it is necessary to consider porosity as a three dimensional microstructure, and consequently a large number of structural parameters can be used to describe it. Some of the most important structural parameters are [13]:

- Cell size and its distribution
- Strut thickness and its distribution
- Strut shape and morphology (i.e. dense or hollow struts)
- Cell window opening
- Degree of anisotropy (of porosity, pore size, etc.)
- Surface to volume ratio

1.1.2 Mechanical properties

Mechanical properties of porous ceramics play an important role in their different applications. This is clear for the cases in which the component serves exclusively a structural function. However, mechanical properties are also quite important for other cases where the primary function is non-mechanical. In such applications, stresses arise and must be survived for the component to continue serving its desired non-mechanical functions.

Porosity's mechanical properties has been characterized mainly experimentally and in the last decades addressed by the use of models. There are several models relating the structural parameters of porous materials and the mechanical behavior [14][15][16][17][12][18]. However, the most extensively used those based on the MSA (Minimum Solid Area) approach developed by *Rice* [19], and the mechanistic models proposed by Gibson and Ashby [10].

Minimum Solid Area method: MSA modeling assumes first that the body can be represented as a dense uniform packing of identical cells (Fig. 1.2a). Each cell consists of either a pore whose center is also the center of the cell surrounded by the solid phase (Fig. 1.2c) or a spherical particle whose center is the center of the cell surrounded by the pore phase (Fig. 1.2b) [11].

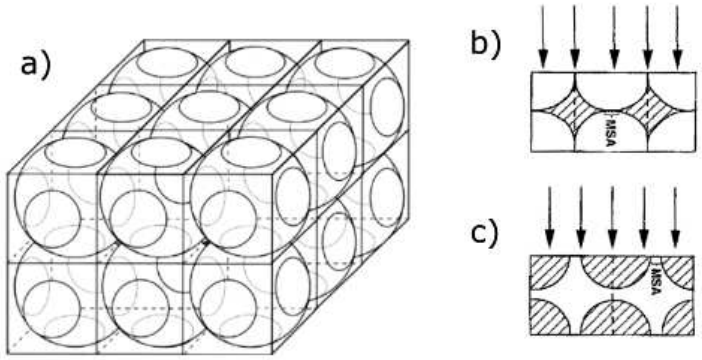

Figure 1.2: Example of idealized pore architecture used in MSA for property modeling a) spherical pores and b) spherical particles

Once a representative cell structure has been selected based on the type of the porosity being modeled, a complete evaluation of the range of porosity can be made by incrementally changing the size of the pore or spherical particle. Afterwards, a purely geometric parameter equal to the minimum area normal to a given direction (MSA) is defined, similarly to the concept of load bearing area Fig. 1.2. *Rice* states that the strength (and also elasticity, electrical resistivity, thermal conductivity, permeability, etc) scale directly to the MSA. The output of MSA modeling is generally a plot of the MSA values (and hence porosity) over the property of interest (Fig. 1.3).

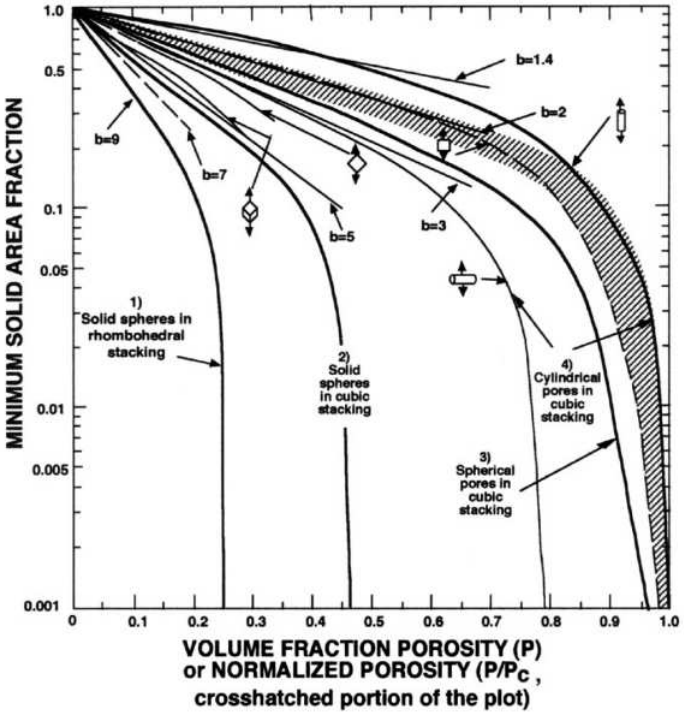

Figure 1.3: Example of the relationship between porosity and MSA for different pore configurations [12]

Most MSA models are generally not presented as an equation, since the individual calculations of each MSA value are complex. However, in some cases where the pore morphology is close to an ideal system, it is possible to reduce the behavior in a simple equation of the form of Eq. 1.2.

$$X/X_0 = (\rho/\rho_0)^n = (1-P)^n \tag{1.2}$$

All the different models based on MSA cover a broad range of pore structures ranging from low to high porosity. Unfortunately, MSA is based in a rigorous set of assumptions and it is only effective in ideal systems [12], something difficult to achieve by conventional processing techniques.

Mechanistic models: The Gibson and Ashby model (G-A) idealize the microstructure of a porous material to a representative unit cell composed by an arrangement of struts, Fig. 1.4. Afterwards, it is possible to scale the mechanical properties (strength, elasticity, fracture toughness, creep rate, etc) with the key microstructural parameters calculating the behavior of each truss when a load is applied [20]. An important factor in this approach is that it can differentiate between substantially different pore architectures (honeycomb, open cells, and closed cells foams) and modes of fracture (brittle crushing,

plastic yielding, and elastic buckling) and therefore describing materials of different nature i.e. polymers, metals, and ceramics [9] [21] [20]. A limitation of this model is that there is less basis for predicting the properties at high and low P% and it does not take into consideration the interaction between pores [11] and the effect of cell size. A more complete discussion about the applicability of these models will be covered in Chapter 4.

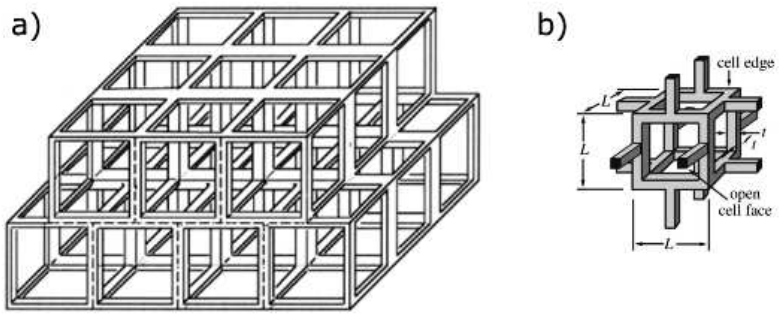

Figure 1.4: Idealized unit cell in an open cell foam

1.1.3 Permeability

Permeability is regarded as a macroscopic measure of the ease with which a fluid driven by a pressure gradient flows through the voids of a porous medium [13]. This property can be expressed as a function of the fluid, flow, and medium properties and usually is obtained by fitting the experimental data with permeability equations. The most common expression is Forchheimer's equation (Eq. 1.3) and states that the pressure drop (ΔP) through a macroscopically homogeneous porous medium exhibits a non-linear dependence on fluid velocity (ν_s) along the flow direction (L) as [22]:

$$\frac{\Delta P}{L} = \frac{\mu}{k_1}\nu_s + \frac{\rho}{k_2}\nu_s^2 \tag{1.3}$$

where μ and ρ are respectively the absolute viscosity and the density of the fluid, and k_1 and k_2 are known as Darcian and non-Darcian permeabilities. These parameters incorporate only the structural features of the porous medium and therefore are considered constant even if the fluid or the flow conditions are changed. The importance of Forchheimer's equation is that the fluid and the porous medium are considered to have an influence on the pressure drop independent of each other [23]. Therefore, once the medium influence is quantified (through k_1 and k_2), it is possible to obtain its pressure drop estimated for a variety of operating conditions, such as velocity, temperature, and pressure. The term μ/k_1 of Forchheimer's equation represents the contribution to flow resistance due to friction between the fluid and the pore walls. The term ρ/k_2 represents

the contributions of inertia and turbulence [22].

Permeability is expected to change according to several structural features (pore volume, cell size, strut thickness, etc) that reflect different aspects of fluid-solid interaction. However, despite the importance of porous ceramics for fluid-flow applications, only in recent years the modeling of permeability based on microstructural parameters has been addressed consistently in the literature [24] [25]. Most of the models used in prediction of permeability are derived from correlations originally developed for granular beds, like:

- Kozeny-Carman equation

$$k_1 = \frac{\epsilon^3}{K_k(6/d_p)^2(1-\epsilon)^2} \tag{1.4}$$

  where ϵ is the total pore volume, K_k the Kozeny parameter usually ranging from 4.8 to 5.0 , and d_p the particle diameter.

- Ergun equations

$$k_1 = \frac{\epsilon^3 {d_p}^2}{150(1-\epsilon)^2} \tag{1.5}$$

$$k_2 = \frac{\epsilon^3 d_p}{1.75(1-\epsilon)} \tag{1.6}$$

  where all the parameters are the same as previously referred.

However, applying these equations on other porous morphologies often leads to inaccuracies [26]. The major difficulty in derivation of such models is identifying a characteristic length that represents the cellular media realistically and thus replaces the particle size d_p[27] [28].

1.1.4 Processing techniques

Pore morphologies exhibited in conventional and novel applications cover a wide range of structures such as foams (open and closed), honeycombs, interconnected rods, interconnected fibers, interconnected hollow spheres, etc. Additionally, most of them require a specific range of pore volume, size, and distribution to be functional. All of these microstructural features are in turn highly influenced by the processing route [8]. Therefore, it becomes critical to know the benefits, drawbacks, and limits of techniques to manufacture macroporous ceramics. Due to the large number of processing routes this section summarize the most important features of the conventional techniques. For a more detailed description see reference [13].

Partial Sintering: Partial sintering of powder compact is the most conventional and frequently employed approach to fabricate porous ceramic materials. Particles of powder compact are bonded due to sintering processes, and a homogeneous porous structure forms when sintering is terminated before the compact fully densified (Fig. 1.5). Pore size and porosity are controlled by the size of starting powders and degree of partial sintering [29]. Porosity decreases with increased forming pressure, sintering temperature, and time. In addition, processing factors such as the type and amount of additives, green densities, and sintering conditions (temperature, atmosphere, pressure, etc.) also greatly affect the microstructures of porous ceramics [30]. The mechanical properties depend largely on the degree of neck growth between grains, as well as porosity and pore size [31].

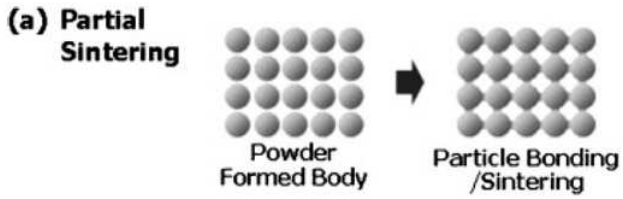

Figure 1.5: Scheme of the concept of partial sintering to obtain macroporous materials [29]

Replica: The replica method is based on the impregnation of a cellular structure with a ceramic suspension or precursor solution in order to produce a macroporous ceramic exhibiting the same morphology as the original porous material (Fig. 1.6). Many synthetic and natural cellular structures can be used as templates to fabricate macroporous ceramics through the replica technique. Porous ceramics obtained with the sponge replica method can reach total open porosity levels within the range 40% - 95% and are characterized by a reticulated structure of highly interconnected pores with sizes between 200 μm and 3 mm [32]. The high pore interconnectivity enhances the permeability of fluids and gases through the porous structure, making these reticulated materials very suitable for filtration [33]. A disadvantage of the sponge replica technique is that the struts of the reticulated structure are hollow and often cracked during pyrolysis of the polymeric template, degrading the final mechanical strength of the porous ceramic [34].

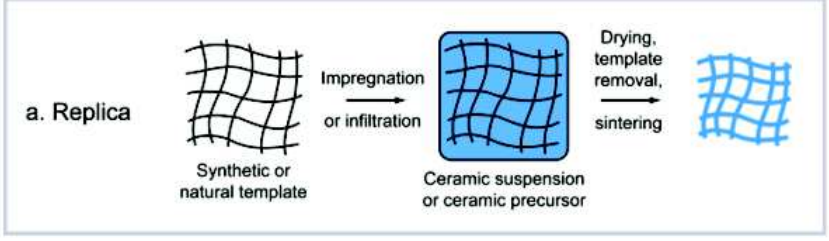

Figure 1.6: Representation of the replica method [32]

Sacrificial Template: The sacrificial template technique consists of preparing a biphasic composite comprising a continuous matrix of ceramic particles and a homogeneously dispersed sacrificial phase. Afterwards, the sacrificial phase (or pore former) is extracted to generate pores within the microstructure (Fig. 1.7). This method leads to porous materials displaying a negative replica of the original sacrificial template. One of the main advantages of the sacrificial template method in comparison with the other fabrication routes is the possibility to deliberately tailor the porosity, pore size distribution, and pore morphology of the final ceramic component through the appropriate choice of the sacrificial material [32]. The range of porosity and pore sizes that can be achieved with this technique is very broad (20% - 90% and 1 - 700 μm, respectively), as they only depend on the volume fraction and size of the sacrificial template used [35].

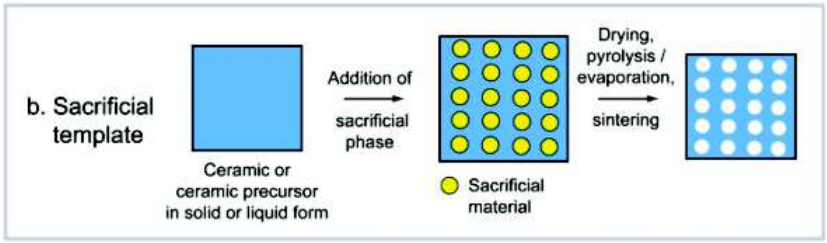

Figure 1.7: Scheme of the steps involved to obtain porous ceramics by the sacrificial template method [32]

Direct Foaming: In direct foaming methods, porous materials are produced by incorporating air into a suspension or liquid media, which is subsequently set in order to keep the structure of air bubbles created (Fig. 1.8). In most cases, the consolidated foams are afterwards sintered at high temperatures to obtain high-strength porous ceramics. The total porosity of directly foamed ceramics is proportional to the amount of gas incorporated into the suspension or liquid medium during the foaming process. The pore size, on the other hand, is determined by the stability of the wet foam before setting takes place [32]. The macroporous ceramics obtained after sintering exhibit porosities from 45 to 95% and cell sizes between 10 and 300 μm.[35]

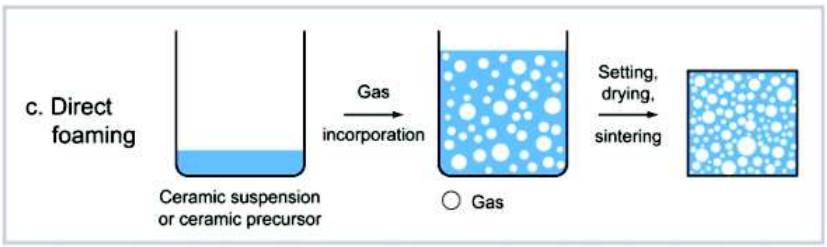

Figure 1.8: Schematic of a direct foaming technique [32]

1.2 Ice-templating

The processing techniques for porous ceramics previously discussed usually lack control of the directionality of the pores, yielding a non optimized microstructures. Ice-templating is a very flexible technique, allowing an almost independent control of several important structural features, including directionality, in a wide range of length scales. Due to its versatility, and because it is mostly based on physical interactions, the process has been applied to a broad range of materials, from polymers to ceramics and metals.

1.2.1 Principle

Ice-templating is a processing technique adapted for producing anisotropic macroporous materials. It is based on the unidirectional freezing of colloidal suspensions and the subsequent segregation of the particles by the solidification front [36]. It comprises four main processing steps: slurry preparation, unidirectionally solidification, sublimation, and sintering (Fig. 1.9).

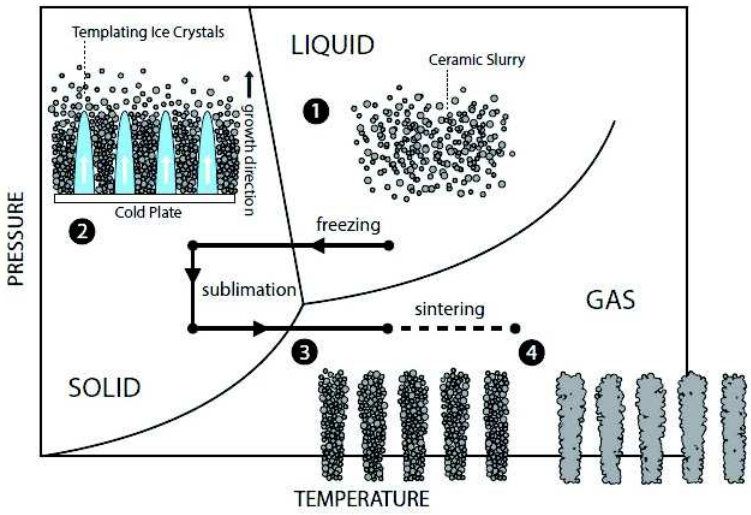

Figure 1.9: Processing steps of ice-templating [36]

1) Slurry preparation: This step is essentially identical to the preparation of slurries for conventional ceramic processing techniques. The ceramic powder must be properly dispersed in the solvent (usually water), so additives such as dispersant are often used. The amount of solids loading can range between 10 vol.% and 40 vol.%, depending on the desired amount of porosity [36]. The use of binder is necessary to provide enough strength to the green body to be handled after the sublimation. Finally, additional additives (zirconium acetate(ZRA), glycerol, polystyrene, sucrose, etc.) can be used to produce certain effects on the pore morphology such as modifying the shape of the

pores, creating roughness on the walls, or increasing the brunching between the walls [37].

2) Controlled freezing: Once the slurry is subjected to a directional temperature gradient, the solvent crystals start growing along the gradient. Simultaneously, the particles are rejected from the moving solidification front and stacked between the ice crystals. This is the critical step where the structure is formed and the characteristics of the future porosity are determined. In order to obtain a unidirectional porous structure, the velocity of the ice front is one of the most critical parameters [6]. If the solidification velocity is very low (less than 1 $\mu m s^{-1}$) the ice front will be planar pushing the particles ahead. The resultant structure contains no macroporosity [38]. On the other hand, when the ice growth is too fast (critical velocity, ν_s) the particles have insufficient time to segregate from the suspension, resulting in complete encapsulation of them within the ice front. Several parameters seem nevertheless to affect this critical velocity, the most important being probably the solid content in the slurry, the particle size and the properties of the solvent [39] [6]. This behavior is schematically summarized in Fig. 1.10

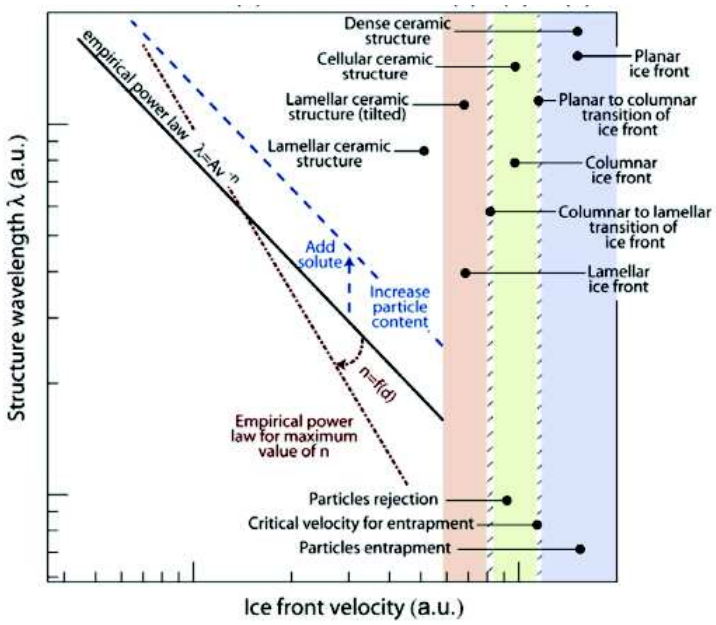

Figure 1.10: Limits for controlling the pore structure based on the ice front velocity [6]

3) Sublimation of the solvent: Once complete solidification of the sample is achieved, the sample is kept at conditions of low temperature and pressure to convert the solidified solvent into gas. Porosity is created where the solvent crystals were, so that a green porous structure is obtained. The porosity is a direct replica of the solidified solvent structure.

4) Sintering: Finally, the green body can be sintered with conventional sintering techniques. During this stage, porosity in the ceramic walls can be removed by carefully selecting the sintering temperature, but the macroporosity created by the solvent crystals is retained.

1.2.2 Pore architecture

Looking at the cross-section, ice-templated specimens can be divided in three different zones based on their pore shape and dimensions, Fig. 1.11. In zone 1, the closest to the cold source, no macroporosity is observed and the layer is dense. In the second zone, the material is characterized by a cellular, randomly oriented morphology. Finally, in the zone 3, the porosity is long, lamellar (in the case water is the solvent) and aligned in the moving direction of the ice front [40]. It is the later zone (also called *Steady-State Zone*, SSZ) that attracted most of the interest, mainly because its pores exhibit a low tortuosity and their microstructure can be related easier with the experimental conditions.

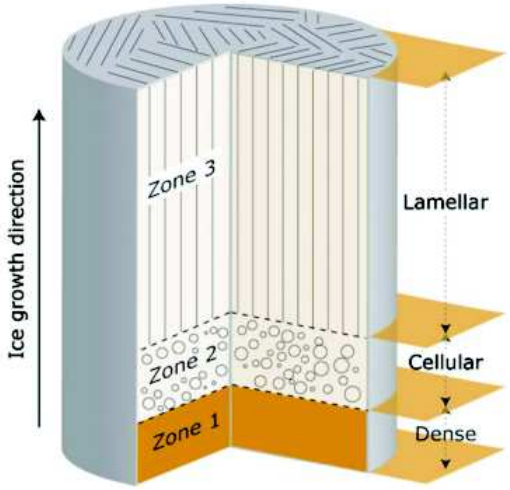

Figure 1.11: Typical porosity microstructure of an ice-templated samples showing the three distinctive zones [40]

Within this zone, the microstructure can be controlled based on the physics of solvent solidification [41]. Particularly, the ice-tip radius (and as a consequence the thickness of the ice crystals) can be modified by increasing or decreasing the cooling rate during freezing. For fast cooling rates, supercooling becomes larger and the ice crystals smaller. Under a very slow cooling regime, the ice crystals become thicker. Frequently, the microstructure in this zone is defined by its wavelength (λ), which is the average thickness of a single ceramic wall plus its adjacent macropore [6], Fig 1.12. Several publications have reported the effects of solidification kinetics in ice-templated materials [6] [42] [43] [44] showing that λ follows an empirical relationship with the ice front velocity

(ν), Eq. 1.7.

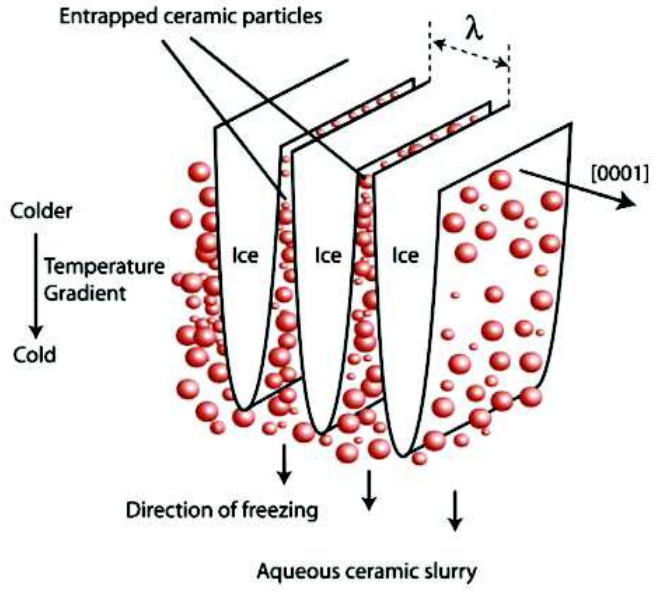

Figure 1.12: Ice crystal formation and particle segregation during ice-templating [6]

$$\lambda = A\nu^{-n} \tag{1.7}$$

where *A* and *n* are fitting parameters dependent on viscosity, solids loading, particle size [6] [45]. However, it is clear that it is extremely complex to predict the pore size (or any microstructural parameter) through a simple analytical expression because the freezing kinetics depend on a large number of factors (the interfacial free energy between the particles, the water and the ice front; the particles size, distribution and content; the interactions of the particles with themselves; the anisotropic effects of the surface tension of ice; the buoyancy forces acting on the particles; the viscosity of the slurry; the diffusion of the solute away from the interface; the latent heat diffusion; etc [6]) and additionally most of these factors are interlinked. Nevertheless, it is possible to broadly classify (Table 1.2) the experimental tools used to modify, and hence to tailor, the porosity in ice-templated materials in:

1. *Chemistry of the slurry*: solvent, material, particle size, additional binders, dispersants or other additives additives.

2. *Operational conditions*: temperature profile, mold material, freezing surface, etc

Structural Feauture	Control	Length Scale	Reference
Orientation and alligment of llamella	Patterning, temperature gradient, applied electric field	100 μm	[37]
Shape of the pores	Additives solid content, solvent, solidification velocity	5 - 200 μm	[37]
Thickness of llamellae, pore dimensions	Solidification velocity, particle size, solid loading	2 - 200 μm	[46][40]
Surface roughness of llamellae	Additives, solidification velocity, particle size	50 nm - 10 μm	[37]
Ceramic bridges	Additives	2 - 50 μm	[37]
Pore interconnectivity	Solids Content	μm	[40]

Table 1.2: Structural features of ice-templated materials [37]

1.3 Oxygen transport membranes

1.3.1 Transport mechanism

Essentially, OTMs consist of a thin (10 μm - 3mm.), dense ceramic membrane where oxygen ions diffuse across the membrane, usually via crystallographic defects [47]. Among many crystal structures available for this kind of materials, most of the high of oxygen permeation materials exhibit either a fluorite or perovskite structure. The reason is because these structures tolerate a large amount of nonstoichiometry that permits them to obtain high number of oxygen vacancies and/or interstitial sites and consequently enhance the oxygen ionic conduction.

The oxygen transport is shown schematically in Fig. 1.13 and involves three progressive steps:

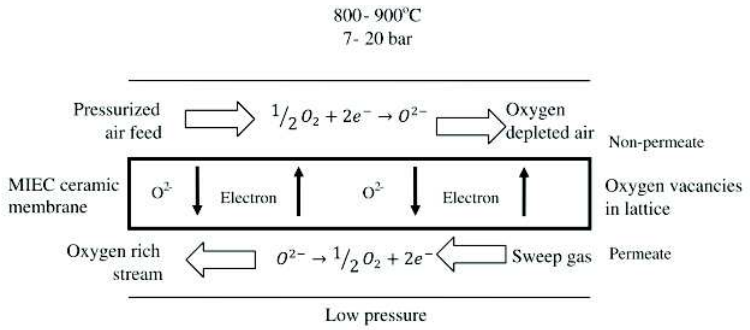

Figure 1.13: Different steps involved in oxygen transport during oxygen permeation [47]

1. Dissociation of oxygen molecules into oxygen anions at the high partial pressure side. This process is known as surface-exchange and can be described by:

$$\frac{1}{2}O_{2(g)} + 2e^- + V_o{}^{**} \longrightarrow O_o{}^x \tag{1.8}$$

2. Ambipolar bulk-diffusion of oxygen anions and electron/holes across the membrane.

3. Recombination of oxygen anions into oxygen molecules on the low partial pressure side of the membrane. In this step, the surface-exchange reaction can be described by:

$$O_o{}^x \longrightarrow \frac{1}{2}O_{2(g)} + 2e^- + V_o{}^{**} \tag{1.9}$$

Each mechanism has the potential to become the rate-controlling step and the slowest process will limit the overall permeation flux. The rate of each process is determined by the composition and geometry of the membrane as well as the operating conditions. For relatively thick membranes (thickness > 100 μm), solid state diffusion commonly controls the process and oxygen flux can be described by the Wagner equation (Eq. 1.10)[48]:

$$J_{O_2} = \frac{RT}{16F^2L}\int_{P_{O_2}{}''}^{P_{O_2}{}'} \frac{\sigma_{el} * \sigma_{ion}}{\sigma_{el} + \sigma_{ion}} \mathrm{d}LnP_{O_2}{}' \tag{1.10}$$

where J_{O_2} is the oxygen permeation flux, R is the gas constant, F is the Faraday constant, L is the membrane thickness, $P_{O_2}{}'$ and $P_{O_2}{}''$ are the oxygen partial pressures at the high pressure side and low pressure side, respectively, σ_{el} is the electronic conductivity, and σ_{ion} is the ionic conductivity.

1.3.2 Performance and limitations in oxygen permeation flux

Eq. 1.10 shows that J_{O_2} can be increased by controlling the operating parameters, pressure and temperature, but changing these parameters can also affect the membrane stability. For instance, increasing the feed gas pressure difference between both surfaces generates an increase in the oxygen flux; but also yields a mismatch of the mechanical stress state for both surfaces. The greater the pressure drop across the membrane, the greater the internal stresses which may finally lead to catastrophic failure of the membrane. Consequently, this approach is mechanically limited by the membrane strength. Moreover, as can be seen in Eq. 1.10, temperature directly affects the oxygen flux and additionally it has a strong impact on the ionic/electronic conductivity. Fig. 1.14 shows that the temperature dependence is increasingly important at temperatures above 800 °C. Thus, operating temperatures are typically at or above 800 °C. At these temperatures, membranes are exposed to different gas environments for an extended period of time that could lead to chemical and structural degradation of the membrane, particularly if reducing atmospheres are used. The maximum oxygen partial pressure gradient

across an OTM is also limited by the membrane's ability to withstand differential chemical expansion arising from the different oxygen occupancy levels on the low $P_{O_2}{}''$ and high $P_{O_2}{}'$ sides of the membrane. This chemical expansion derived stress compounds with stresses resulting from pressurized feed gases, as discussed above.

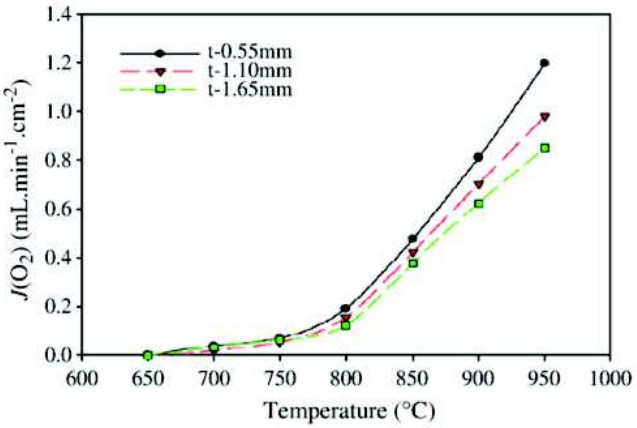

Figure 1.14: Oxygen permeation fluxes at different temperatures and membrane thickness. [47]

Clearly, OTMs must withstand harsh thermomechanical stresses before and during high temperature operation for an extended period of time without any chemical or structural changes. This combination of continuous stress at high temperatures causes irreversible time-dependent deformation (creep) that can even lead to a catastrophic failure of the membrane. This behavior becomes an important factor in the OTM performance and emerges as a critical factor that severely limits industrial application of current generation OTM.

With the previous discussion it is apparent that the oxygen permeation flux, for a given composition, has a performance limit depending on the operating parameters. So, it becomes crucial to find other ways to maximize the oxygen flux beyond simple varying pressure and temperature. According to the Eq. 1.10, the oxygen permeation performance could be improved with a proper material choice based on its ionic/electronic conductivity (i.e. maximizing $\sigma_{el} * \sigma_{ion}/\sigma_{el} + \sigma_{ion}$). However, this approach could be difficult to achieve because a significant increase in the ionic conductivity also results in a higher creep rate (Fig. 1.15), since both phenomena are governed by the same mechanism, diffusion. For instance, at normal operating temperatures (800-900 °C), temperatures needed to obtain a sufficient ionic/electronic conductivity, a low creep rate is required to ensure mechanical stability. Generally, decreasing the creep rate is accomplished by means of forming stronger, more covalent bonds between atoms that hamper diffusion. However, this will also have a detrimental effect on the oxygen diffusion necessary to provide a reasonable flux. The fact that both properties (creep rate and ionic conductivity) are highly interconnected makes it difficult to improve the performance by

modifying composition since there must be a compromise between mechanical stability and oxygen flux.

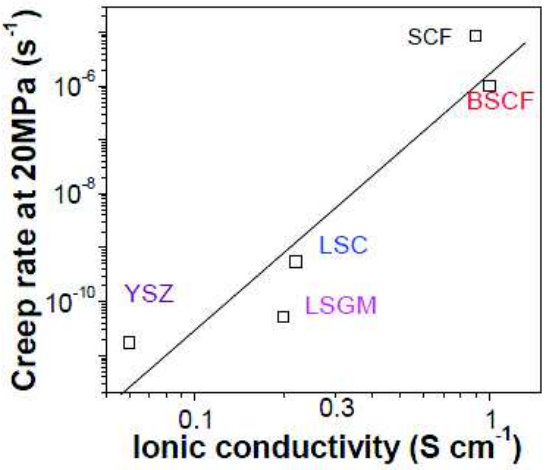

Figure 1.15: Relation between ionic conductivity and creep rate for different ceramics. Yttria Stabilized Zirconia (YSZ), LaSrGaMgO(LSGM), LaSrCoO(LSC), BaSrCoFeO (BSCF), and SrCoFeO(SCF).

Because oxygen flux is inversely proportional to the membrane thickness (Eq. 1.10), one of the most used approaches is reducing the membrane thickness as low as possible, Fig. 1.16. However, it has to be noted there is a limit to this behavior caused by changing the rate limiting mechanism from diffusion to the surface exchange reaction when the thickness is reduced, which means that Wagner equation (Eq. 1.10) is no longer applicable. Thus, there is a limit in the thickness reduction, beyond which the oxygen flux does not improve and the membrane is too thin to support the mechanical stresses. From a reliability point of view, it is very important to determine this point to maximize the oxygen flux without overly impacting mechanical stability.

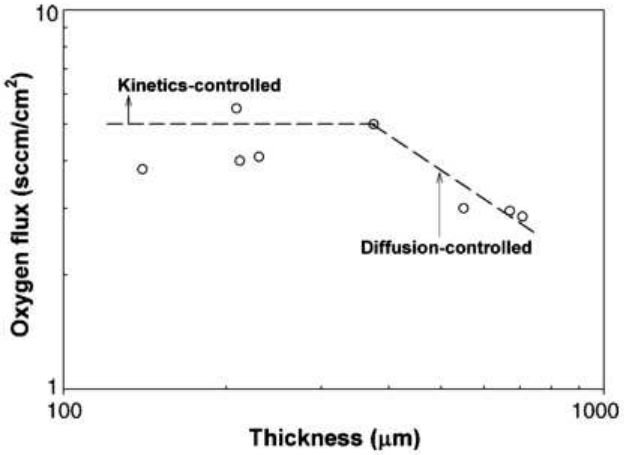

Figure 1.16: Relationship between oxygen flux and membrane thickness in $La_{0.2}Ba_{0.8}Co_{0.8}Fe_{0.2}O_{3-x}$ [49]

1.3.3 Asymmetric membranes

When the membrane thickness becomes very low (<100 μm), a porous support is needed to provide the mechanical strength required and facilitate the gas transport.

This configuration is called an asymmetric membrane (Fig. 1.17), and it has led to recent performance improvements [50]. However, this approach brings mechanical stability issues at high-temperature, mainly caused by the high coefficient of thermal expansion (CTE) observed in most of OTM ceramic materials. A CTE mismatch between the dense layer and the substrate may generate cracks that could compromise performance. To prevent this problem, the porous substrate may be fabricated with the same material as the dense layer, or the CTEs of the two materials should be matched.

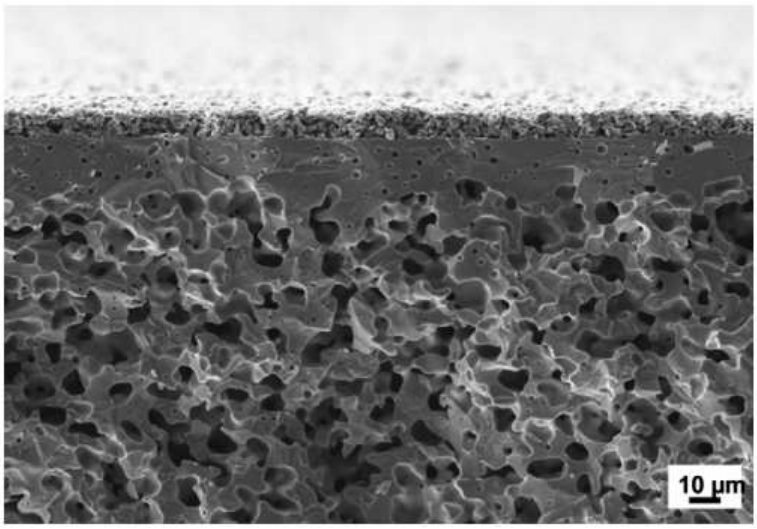

Figure 1.17: Cross section of an asymmetric membrane assembly consisting of porous support, dense membrane layer, and porous surface activation layer made from $Ba_{0.5}Sr_{0.5}Co_{0.8}Fe_{0.2}O_{3-\delta}$ [2]

In addition, the introduction of a porous substrate also generates a source of resistance to the oxygen flow. Since gas diffusion through the pores is the main transport mechanism through the support, the architecture of the pore structure should provide a compromise between maximizing gas flow and mechanical properties. All of these resistances (surface exchange, solid state diffusion across the membrane, and gas diffusion through the porous structure) are intrinsic to the process and thus cannot be removed. As a result, it is critical to understand the controlling mechanisms and ameliorate them as a function of membrane composition, membrane architecture, and operation conditions.

Chapter 2

Materials and Methods

Contents

2.1 Sample processing

2.1.1 Ice-templated specimens (unidirectional porosity)

Ceramic suspensions were prepared by mixing distilled water with 3 mol% yttria-stabilized zirconia (TZ-3YS, particle size $d_{p\ 50}$ = 0.6 μm, Tosoh, Tokyo, Japan) at different weight ratios (from 40% to 70%), 0,75 wt% of dispersant (Prox B03, Synthron, Levallois-Paris, France), and 3 wt% of organic binder PVA (PVA2810, Wacker, Burghausen, Germany). The slurry was magnetically stirred during 5-10 mins before adding a new component and then, ball milled for a minimum of 18 h to break up the agglomerates to ensure a good dispersion. Table 2.1 shows the specific composition for the slurries investigated in this work.

Component	40 wt.% SL	50 wt.% SL	55 wt.% SL	60 wt.% SL	65 wt.% SL	70 wt.% SL
Water	29,90g	34,32g	31,57g	28,70g	25,26g	21,60g
TZ-3YS	21,67g	39,00g	45,22g	52,50g	60,36g	70,00g
Prox B03 0,75 wt.%	0,16g	0,29g	0,34g	0,39g	0,45g	0,52g
PVA2810 3 wt.%	3,25g	5,85g	6,78g	7,88g	9,05g	10,50g

Table 2.1: Details of the standard slurry studied in this work. All the weights are calculated to obtain 50 ml of slurry.

Also, a small set of experiments was prepared based on composition in Table 2.1 and using Ca(Ti,Fe)O_3 (CTF) with a density of $\rho_{ctf} = 4,0gcm^{-3}$) as a raw material instead of YSZ. The results will be compared with YSZ as a model material. The choice of these two materials is twofold:

- 1) to assess that the source of the concerned properties (strength and permeability) is the pore architecture rather than the nature of the material
- 2) the applicability of both materials on energy production purposes, so this information can be useful for future work.

Additionally, the composition of a second set of samples was modified to obtain a different pore morphology. First, distilled water was mixed with 5 wt.% of PEG 6M as a binder (Merck), and zirconium acetate (ZRA) as a pore modifier in a concentration of 20 g/L. The specimens prepared with this composition will be referred later on as a "Honeycomb" due to the ability exhibited by ZRA to generate hexagonal pores [51]. Finally, 3 mol% yttria-stabilized zirconia (TZ-3YS, Tosoh, Tokyo, Japan) was added to the slurry, stirred, and ball milled. The details of the "Honeycomb" slurry are shown in Table 2.2.

Component	50 wt.% SL	55 wt.% SL	60 wt.% SL	65 wt.% SL
Water	34,78g	33,88g	32,55g	31,21g
TZ-3YS	39,00g	46,44g	54,75g	65,00g
ZRA 20 g/L	5,42g	5,28g	5,07g	4,86g
PEG 6M 5 wt.%	1,95g	2,32g	2,74g	3,25g

Table 2.2: Details of the "Honeycomb" slurry. All the weights are calculated to obtain 50 ml of slurry.

The ice templating process consisted of pouring 10 ml of slurry into a PTFE mold (20mm diameter 25mm height) placed on a copper cold surface. The cooling rate was controlled adjusting the temperature of the freezing source. The top of the samples was exposed always to air and kept at room temperature. So the freezing of the slurry occurred unidirectionally following the temperature gradient (from bottom to top). Two different systems have been used to achieved a clearly differentiated freezing conditions. Fig. 2.1-A shows the set-up used for the slowest cooling rate. The freezing temperature was controlled by circulating silicone oil regulated by a cryothermostat (Hubert CC 905). This system is capable to control accurately the freezing rate between 1 - 3 °C/min. In

this work, the cooling rate was set at 2 °C/min and monitored by a thermocouple placed inside the copper plate, Fig. 2.1-B. The cooling rate was determined to be 2 °C/min.

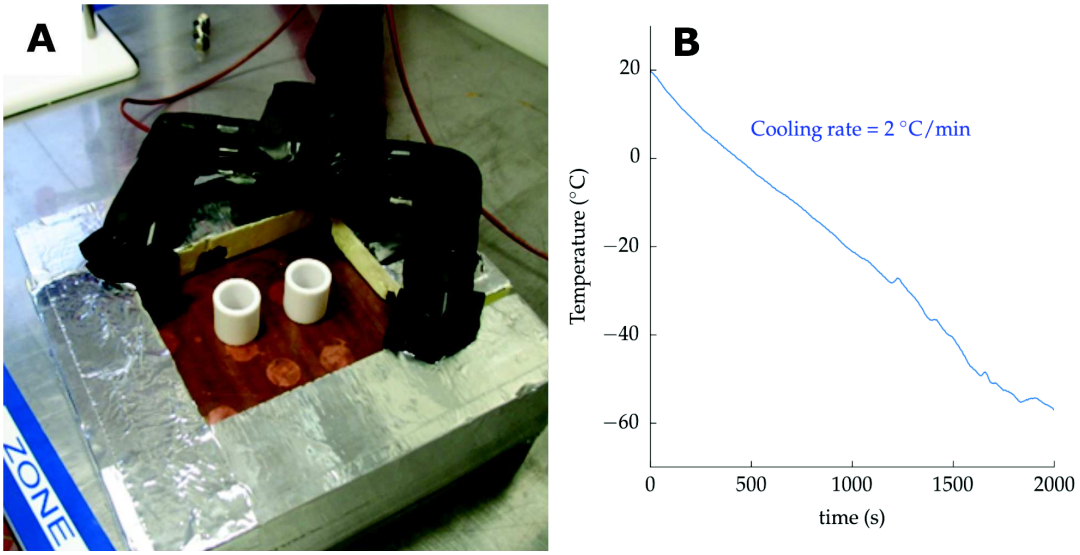

Figure 2.1: A) Freezing set-up used to achieve the cooling rate of 2 °C/min. B) Evolution of temperature with time for the set-up shown in a).

A faster cooling rate was achieved by dipping a copper finger in a container with liquid nitrogen (Fig. 2.2-A). The same molds were placed on top of the copper rods and the temperature was tracked by a thermocouple set near the freezing surface. This system allows a less accurate control of the cooling rate determined by holding the liquid nitrogen level in a specific height. In this work, the volume of liquid nitrogen was kept constant and the cooling rate was determined to be ≈ 30 °C/min, Fig. 2.2-B.

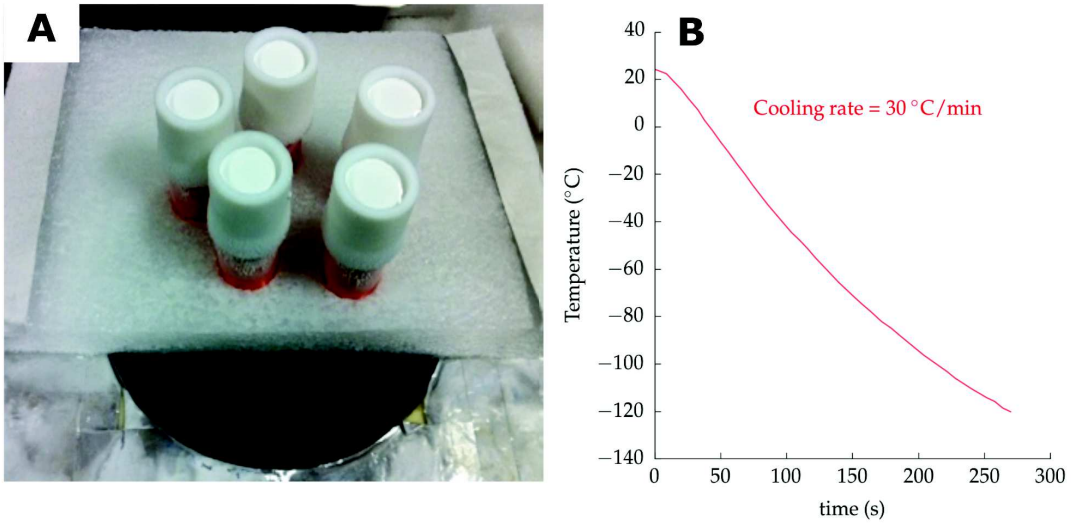

Figure 2.2: A) Freezing set-up used to achieve the cooling rate of 30 °C/min. B) Evolution of temperature with time for the set-up shown in A).

After solidification, samples were removed from their molds and sublimated for at least 48 h at 0.2 mbar in a commercial freeze-dryer (Free Zone 2.5 Plus, Labconco, Kansas City, Missouri, USA).

2.1.2 Pore formers specimens (isotropic porosity)

Samples with a non-oriented porosity were also prepared to be compared with those made by ice templating. The same zirconia powder was mixed with commercially available polypropylene (Propyltex 140S, particle size $d_{p\ 50} = 50\ \mu m$, Micro Powders Inc, Tarrytown, USA) as a pore former at different weight ratios (50%, 60%, and 70%). The blend of powders was added in a distilled water and then, magnetically stirred and ball milled for a minimum of 24 h to break up the agglomerates and ensure an homogeneous mix. Afterwards, the slurry was frozen by dipping the container in liquid nitrogen and freeze-dried to remove the water. Then, 8g of the obtained mix of powders was pressed at 0,8 MP in a mould of 20 mm diameter. The size and amount of pore formers was adjusted to be comparable with the samples prepared by ice templating and isolate the effect of pore directionality.

2.1.3 Ice templated tubes

The set up used to ice templated tubes consisted on a cryothermostat (Hubert CC 905), a freezing liquid, a metallic container, a tube-shape mould and a rotation system attached to it, Fig. 2.3.

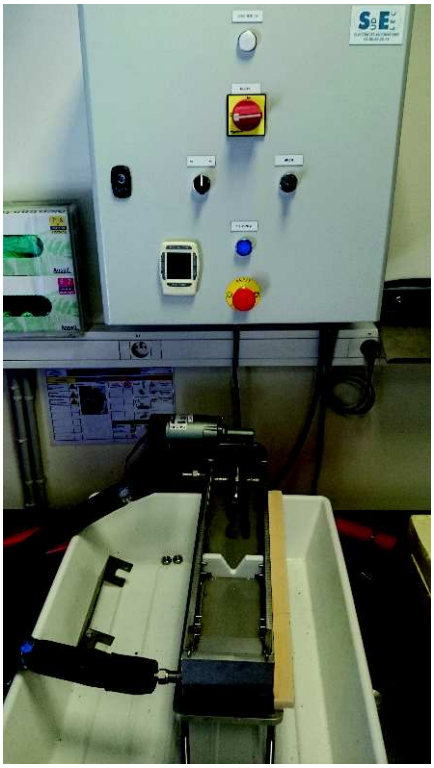

Figure 2.3: Set-up developed to freeze under rotation and produce ice-templated tubes.

The procedure started preparing a ceramic slurry in the same way as it was done to ice template monoliths (Fig. 2.4-a). The tube-shape mould was first cleaned with ethanol (Fig. 2.4-b) and the two half tubes and the bottom cap were assembled. A clean and scratch-free surface are critical points to minimize the presence of defects on the tubes. Silicon grease was applied in the junction of the pieces to avoid leaks of slurry. Then, a controlled quantity of slurry was poured into the mould and the second cap was assembled (Fig. 2.4-c). Like in any system used to produce samples by ice templating, it is necessary to precisely control the temperature of the freezing agent. In this case, the metallic container was first cooled down circulating the freezing liquid during 10-15 min at a preset temperature. Once the temperature of the system was constant the silicon oil was pumped out of the container and the tube was attached to a rotation system. All the tests were performed at a rotation speed of 70 rpm. Then, the silicon oil is pumped in again in the container until it achieves a steady flow. Afterwards, the slurry is left 5 mins under rotational freezing (Fig. 2.4-d). The next steps are similar as in any ice templating process: demoulding (Fig. 2.4-e), freeze drying (Fig. 2.4-f), and sintering (Fig. 2.4-g).

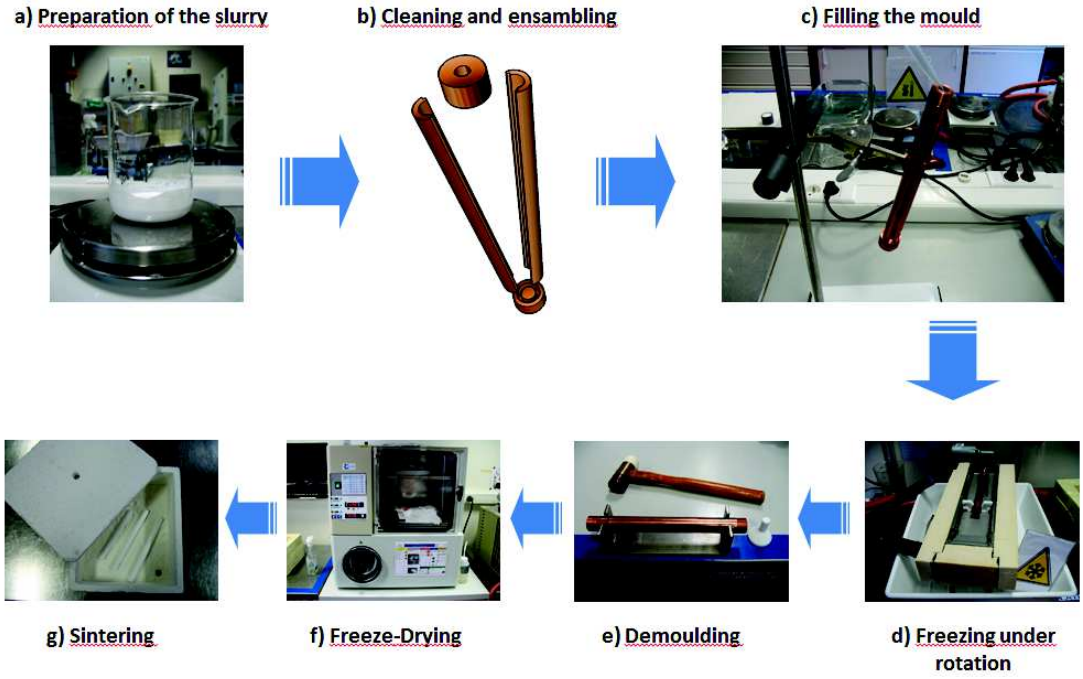

Figure 2.4: Schematic of the process to obtain ice-templated tubes

This process was repeated several times with few variations on the experimental conditions to assess the effect of each one on the pore morphology of the tubes. The experimental conditions studied were: solids loading of the initial slurry (50 wt.%, 55 wt.% and 65 wt.%), temperature of the freezing medium (-30 °C and -80°C), and amount of slurry poured into the mould (16, 18, and 20 ml).

2.1.4 Sintering

Specimens were sintered in air by heating to 500°C at 3 °C/min with a 5h hold to ensure a proper organic burn out. Afterwards, they were sintered between 1300°C and 1400°C at 5 °C/min and held 3h to evaluate the effect of densification in the walls. Then, samples were cooled down to room temperature at 5 °C/min. An schematic of the complete sintering cycle is shown in Fig. 2.5. Specimens with isotropic porosity were sintered following a similar cycle with an extra step at 900°C and a heating rate of 0,25 °C/min to ensure a proper pore formers burn out and crack free samples.

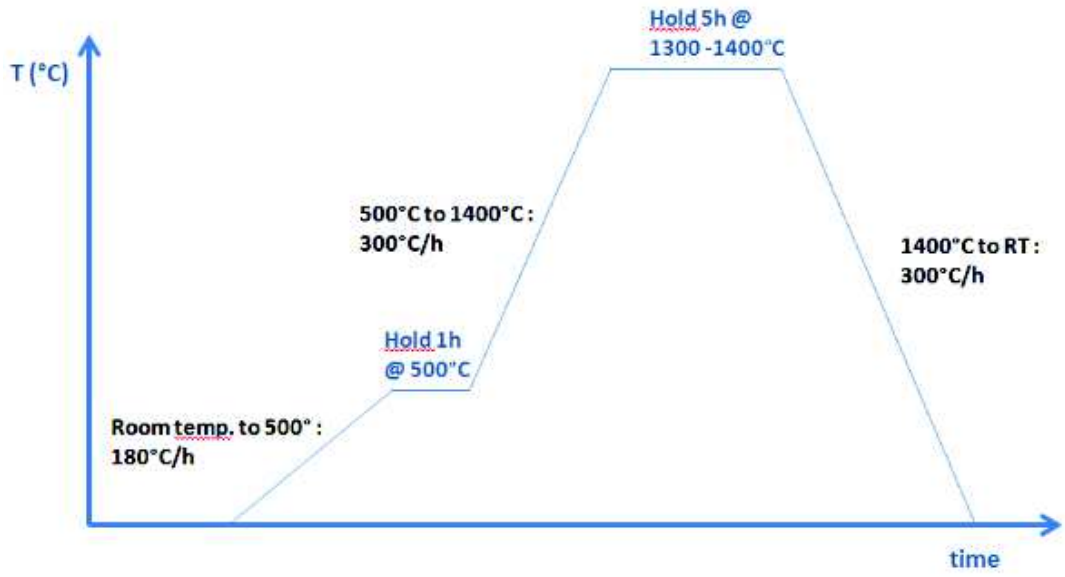

Figure 2.5: Description of the sintering cycle used in ice templated samples.

2.2 Characterization

2.2.1 Morphological

The overall porosity, P(%), was calculated based on the mass (m) and volume (V) of the samples with respect to that of fully dense TZ-3YS ($\rho_{ysz} = 5,8 gcm^{-3}$), as:

$$\rho_{rel} = \frac{\rho}{\rho_{ysz}} = \frac{mV^{-1}}{\rho_{ysz}} \tag{2.1}$$

$$P(\%) = (1 - \rho_{rel}) \times 100\% \tag{2.2}$$

The results were confirmed in some specimens by the Archimedes method (ASTM B962-13) and a good agreement was found. The determination of pore size and wall thickness distributions were performed by image analysis using the "Local thickness" plug-in of the Fiji software [52]. First, the plug-in requires a binarized form of the image to separate between solids and voids. Afterwards, it fits the diameter of the largest sphere inside the void. This process is repeated until the totality of the pore is filled.

The sample preparation was; first, the specimen was sonified in water during 15 mins to remove the debris entrapped in the macroporosity and dried afterwards at 40°C for 24h. Then, it was infiltrated in vacuum with an epoxy resin (EpoFix, Struers, Denmark) and cured for at least 24 h. Next step was manual polishing using pads of 58 μm, 40 μm, 26 μm, 15 μm, and 10 μm . In order to homogenize the data and give a result more

representative of the sample, all the images were taken from different locations in a cross section perpendicular to the freezing direction (7 mm from the bottom of the sample) with a scanning electron microscope (FEI Nova NAnoSEM) at 10-15 kV. The resolution of the images used to evaluate pore size and wall thickness was 0.5 - 1.5 μm/pixel, a value relatively smaller compared with the final polishing pad size. The results were confirmed by mercury intrusion porosimetry (AutoPore IV 9500, Micromeritics) with an applied pressure up to 0,31 bar.

2.2.2 Mechanical testing

Monoliths

The mechanical properties of specimens with isotropic (pore formers) and anisotropic (ice-templated) porosity were measured by a compression test (Lloyd Instruments) at a crosshead speed of 0.5 mm/min to evaluate the effect of each pore descriptor on strength and reliability. The ice-templated specimens were tested with the pores aligned parallel and perpendicular to the load. The crush tests were carried out at a crosshead speed of 0.5 mm/min. The bottom and the top of the samples were removed with a slow speed saw leaving a final dimensions around 15 mm diameter and 17 mm height. In order to minimize the effect of superficial defects and misalignment, a cardboard pad was placed on both sides of the samples. In all the tests, the maximum load right after finishing the elastic stage was recorded and used to calculate the compressive strength. Fig. 2.6 shows the equipment used.

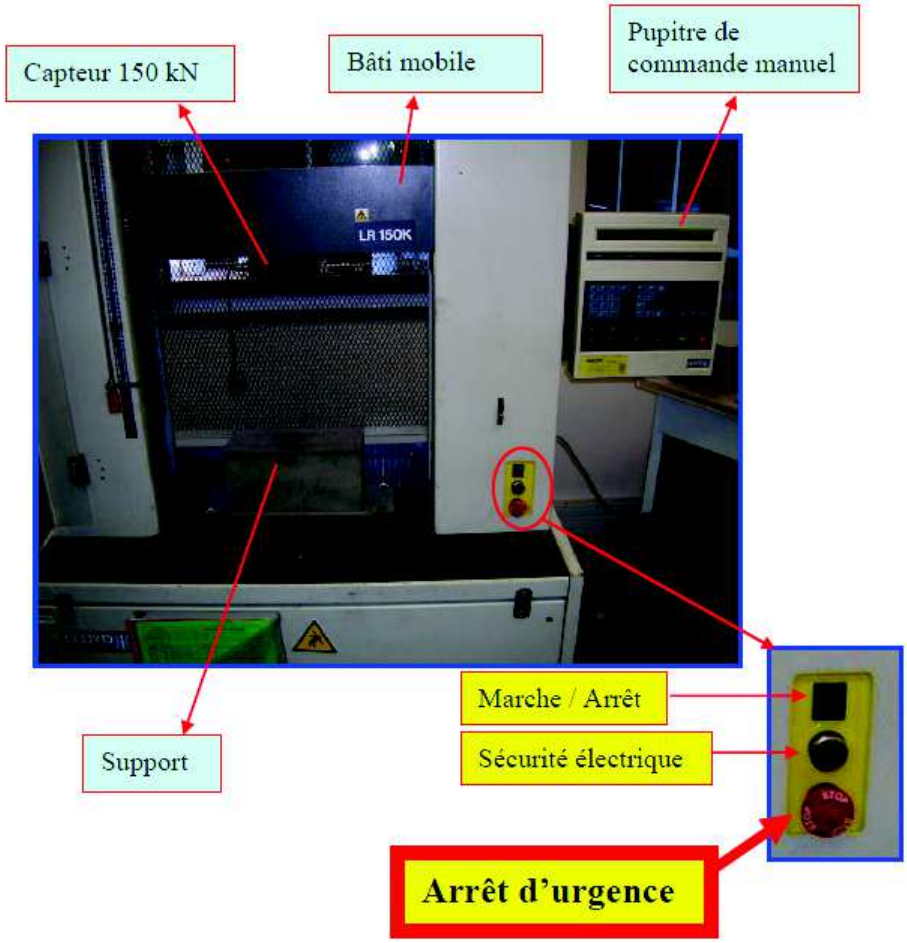

Figure 2.6: Description of the equipment used in the compressive tests.

Afterwards, a two-parameter Weibull analysis was applied to the compressive strength data to predict the probability of failure (P_f) for a given stress (σ) through the expression:

$$P_f = 1 - exp\left[-\left(\frac{\sigma}{\sigma_0}\right)^m\right] \tag{2.3}$$

where *m* is the Weibull modulus and σ_0 the characteristic strength where P_f = 0,632. To obtain an unbiased measurement of *m*, a minimum number of 15 samples were tested.

The Weibull modulus (m) was calculated as follows. For each of the 5 groups, the strength values were ranked in ascending order, i = 1, 2, 3, ..., N, where N is the total number of specimens in the group and *i* is the *ith* position in the same group. This allows a ranked probability of failure to be assigned to each result according to:

$$P_f = \frac{i - 0,5}{N} \tag{2.4}$$

The next step was to plot the data in a LnLn(1/1-Pf) vs. Ln σ form and fit a linear regression. The slope of the line is the Weibull modulus (m).

If we want to compare the Weibull modulus of the various samples and interpret differences between them, it is important to understand the statistical confidence interval that result from our data and fitting procedures. Therefore, we fit the data using two different techniques. First, m and σ_0 were determined from an ordinary least squares (OLS) fit of ($LnLn(1/(1-P_f))$) versus ($Ln\sigma_f$) where the slope of the resulting line is m and (σ_0) is the solution to $LnLn(1/(1-P_f)) = 0$. Second, a Bayesian Markov Chain Monte Carlo (MCMC) was applied to directly fit the data to the nonlinear Eq 2.3

Tubes

Mechanical properties of ice-templated tubes were characterized through three different tests: 1) Four-point bending on half tubes, 2) O-Ring test, and 3) compression test. All the experiments were conducted in a testing machine Shimadzu, AGSX with a 10kN load cell and a crosshead speed of 0,2 mm/min.

- **1)** Samples were cut with a low-speed saw first in the radial direction and then in the longitudinal one with a final length (L) = $\geq$ 55 mm, and external diameter (D_{ext}) = 10 mm. The spacing between the outer supports was adjusted to S_1 = 40 mm whereas the span between the inner supports was S_2 = 20 mm. Fig. 2.7a and 2.7b show the equipment used and a representation of the distribution of forces during the test, respectively

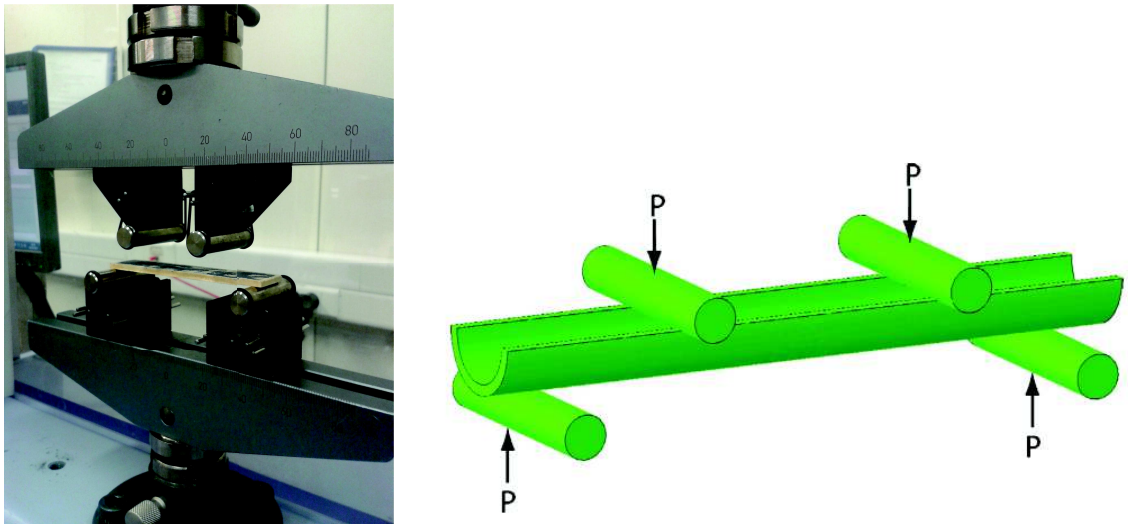

(a) (b)

Figure 2.7: Detail of the equipment used in the characterization of flexural strength of half tubes b) Test configuration of four-point bending of half tubes [53].

- **2)** Eight tubes were sliced in the radial direction with a low-speed saw leaving

specimens with an external diameter (D_{ext}) = 10 mm, height (h) ≈ 4 mm, and thickness (t) ≈ 2 mm. Tests were performed with a piece of alumina supporting the samples to avoid the rotation and distribute evenly the load through the surface. An schematic of the system used and a sample description are shown in Fig. 2.8a) and b).

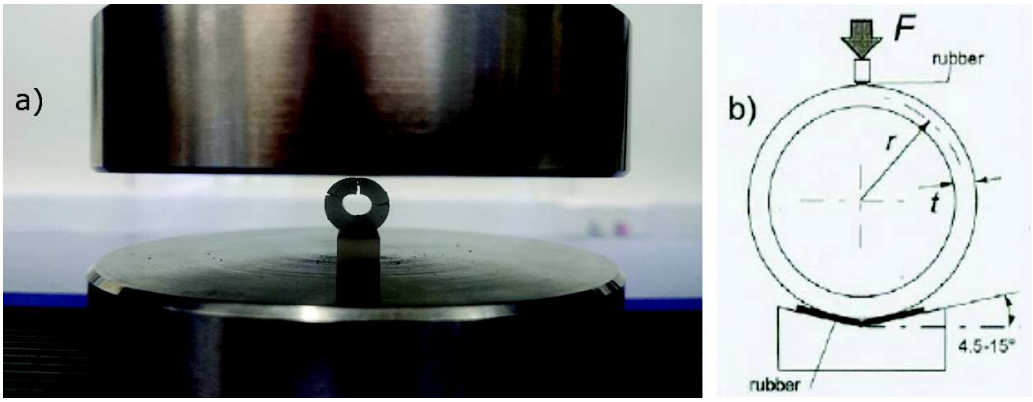

Figure 2.8: a) Characterization of the radial strength by an O-ring test. b) Detail of the test configuration.

- **3)** Sample preparation for the compression test was carried out similarly as the O-Ring test. The final dimensions were: external diameter (D_{ext}) = 10 mm, and height (h) ≈ 12 mm. Specimens were loaded in the axial direction until a significant drop in the load ($\geq$ 10%) was observed. Afterwards, the compressive strength was calculated based on the peak stress divided by the contact area.

2.2.3 Pressure drop (Permeability)

Gas permeability was measured using an equipment build in house (Fig. 2.9) and based on the ASTM standard C577-99. Synthetic air was passed through the samples which were held by a silicon ring. A preliminary test was performed to evaluate the existence of leaks. The air flow studied ranged between 0-25000 ml/min (0-2 m/s) and it was controlled by an electrovalve. Two sensors were placed right before and after the specimens to record the inlet and outlet pressure at room temperature and afterwards calculate the pressure drop. Due to experimental limitations, the pressure drop could not exceed 350 MPa.

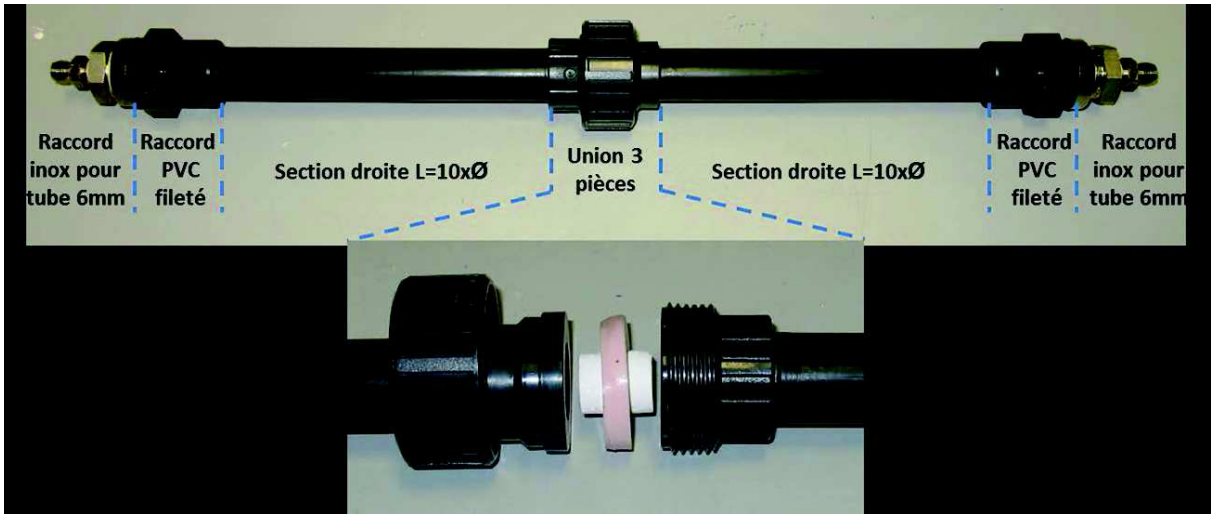

Figure 2.9: Set-up used to measure the pressure drop

The pressure drop was measured in ice templated samples with different pore structure (pore volume, size, and morphology) and in samples processed by pore formers. At least 3 samples per condition were tested. In the case of ice templated specimens, it was cut off 2 mm from the bottom to remove the *transition zone* (part with non-directional porosity) and test exclusively the part with lower tortuosity. The pressure drop test was performed with the pores aligned parallel to the flow. The final dimensions of all the specimens were 12-15 mm thickness (L) and 15 mm diameter. The same type of test was performed in ice templated tubes with one closed side. Their dimensions were; 120 mm length (L), 10 mm external diameter (D_{ext}), and 6-7,5 mm internal diameter (D_{int}).

Permeability was evaluated using the Forchheimer's equation adapted for compressible fluids, Eq. 2.5:

$$\frac{\Delta P}{L} = \frac{{P_i}^2 - {P_o}^2}{2P_oL} = \frac{\mu}{k_1}\nu_s + \frac{\rho}{k_2}{\nu_s}^2 \tag{2.5}$$

where L is the thickness of the sample (parallel to the flow), μ and ρ are the viscosity and the density of the fluid (air at 25 °C), ΔP is the pressure drop, k_1 and k_2 are the Darcian and non-Darcian permeabilities, and ν_s is the fluid velocity (air flow divided by the cross-sectional area of the sample).

Chapter 3

Microstructural characterization of ice-templated samples

Contents

This chapter briefly presents the effect of experimental parameters on pore volume, pore size, wall thickness, and pore shape of ice-templated materials. Further discussion on microstructural control will be addressed in the subsequent chapters, highlighting the important features related with the property studied in each section. Table 3.1 summarizes the most relevant pore descriptors and their respective processing conditions. Most of the discussion presented here is referred to these samples and they will be the baseline to understand the microstructural control. Fig. 3.1 shows the representative cross sections obtained for each condition reported in Table 3.1.

3.1 Pore volume fraction

Total pore volume is mainly determined by the volumetric ratio between ceramic particles/water, and referred hereinafter as solids loading. Table 3.1 shows that increasing the solids loading from 50 wt.% to 65 wt.% reduces porosity from 69,5% to 52,5%. The main mechanism to create pores is the rejection of particles from the advancing solidification front, so increasing the solids loading will increase the amount of particles rejected and consequently lead to a higher relative density. This behavior is independent of the cooling rate, so two samples with the same solids loading and frozen at different

rates will have the same total pore volume. This effect can be observed comparing the porosity (P%) exhibited by specimens a, b, c, and d in Fig. 3.1 and Table 3.1 frozen at 2 °C/min with their counterparts e, f, g, and h frozen at 25 °C/min. These results are consistent with previous work for the same materials and similar processing conditions [54] [55] [56] [57] [58].

Sample	Solid loading(wt.%)	Freezing rate (°C/min)	Porosity(%)	Mean d_{pHg}(μm)	Mean d_{pIA}(μm)	Mean wall thickness(μm)
a	50%	2	69,5%	19,1	20,0 $\pm$ 8,5	11,2 $\pm$ 4,5
b	55%	2	64,2%	17,5	17,7 $\pm$ 6,7	14,7 $\pm$ 6,2
c	60%	2	60,4%	14,2	13,9 $\pm$ 5,5	15,8 $\pm$ 6,8
d	65%	2	52,5%	8,3	13,7 $\pm$ 4,8	19,1 $\pm$ 8,2
e	50%	25	70,4%	5,4	4,7 $\pm$ 1,9	3,6 $\pm$ 1,5
f	55%	25	65,2%	4,3	4,3 $\pm$ 1,7	3,9 $\pm$ 1,6
g	60%	25	60,7%	3,9	4,1 $\pm$ 1,7	5,2 $\pm$ 2,2
h	65%	25	51,5%	2,9	3,1 $\pm$ 1,2	3,0 $\pm$ 1,3

Table 3.1: Summary of the most relevant pore descriptors and their respective ice-templating conditions. d_{pHg} and d_{pIA} correspond to the mean pore size obtained by mercury porosimetry and image analysis respectively. At least two specimens have been evaluated per condition in both characterization techniques, mercury porosimetry and image analysis.

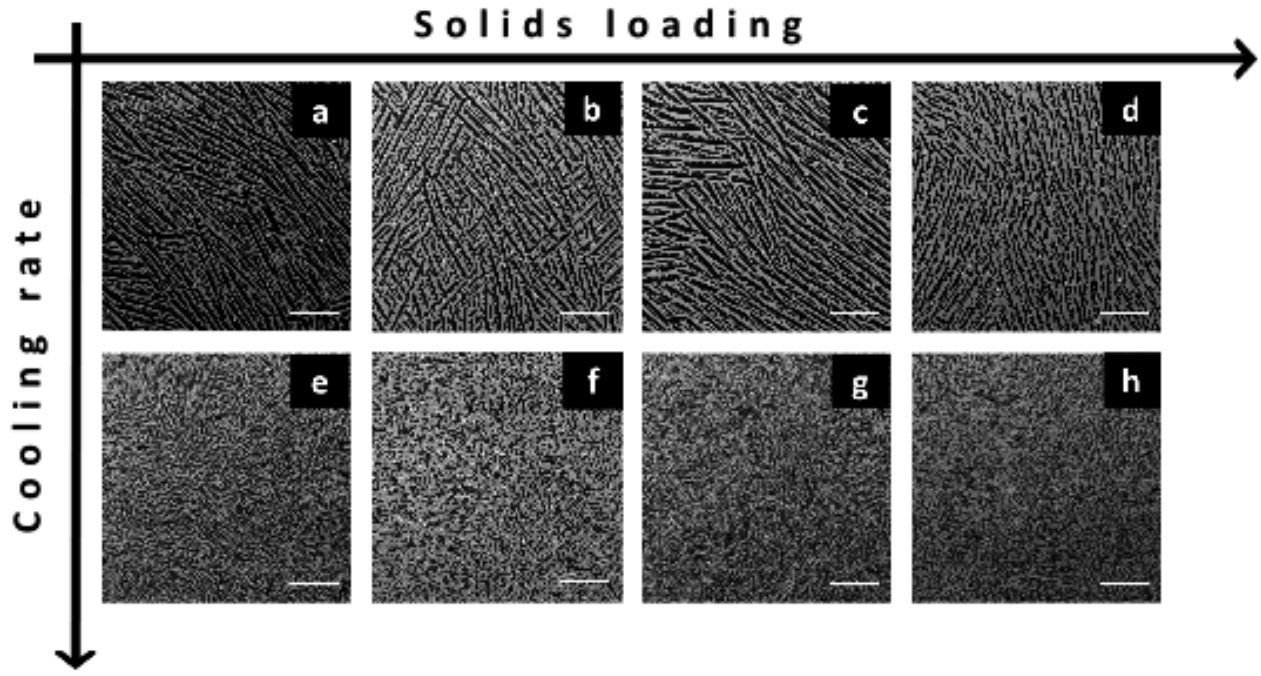

Figure 3.1: Ice templated microstructures obtained at different conditions a) 50 wt.% and 2 °C/min, b) 60 wt.% and 2 °C/min, c) 65 wt.% and 2 °C/min, d) 50 wt.% and 25 °C/min, e) 60 wt.% and 25 °C/min, f) 65 wt.% and 25 °C/min. Scale bars: 300 μm

Besides solids loading, pore volume can also be tailored by the sintering temperature. Obviously, increasing the sintering temperature decreases the total pore volume. However, the description of the phenomena is much more complex than that, since we must consider both types of porosity (between the walls and inside the walls) present in ice-templated materials and understand how they evolve with sintering temperature. This

topic will be addressed in more detail in Section 4.3.2.

3.2 Pore size

For ice-templated materials, freezing rate mainly controls the pore size. As Table 3.1 shows, samples frozen at 2 °C/min (samples a, b, c, and d) exhibit a mean pore size between 10 and 20 μm, while the samples frozen at 25 °C/min (samples e, f, g, and h) have an average size in the range of 3-5 μm. When a colloidal suspension is frozen faster, the magnitude of supercooling ahead of the ice front increases and the tip radius of the ice crystals decreases, thus creating a finer microstructure [46]. Pore size evaluation was performed using two different techniques: image analysis and mercury porosimetry. Both give comparable results in all the experimental conditions with the exception of the specimen "d". The most likely reason is because increasing the particle concentration in the solution increases the probability to create volumetric defects as bottle-necks or closed pores that will affect the measurement by mercury porosimetry but not necessarily in the image analysis.

However, freezing rate is not the only parameter affecting the pore size. Since crystal dimensions are determined by the solidification kinetics of the solvent and the temperature gradient, any parameter that could modify it such as variations in pH, particle size, or additives may have a direct impact on pore size [59]. In addition to these parameters, the initial solid loading of the slurry also affects the pore size. However, this is based on a physical effect rather than a kinetic one. When the solids loading increases there are more particle being rejected by the solidification front and thus limiting ice crystal growth. As shows Fig. 3.2 Samples with 50 wt.% and 55 wt.% solids loading (samples a and b) exhibit a similar bimodal distribution, with two predominant peaks at 25 μm and 15 μm. Both peaks can be correlated with the pores left by the primary ice crystals (25 μm) and the smaller sencondary dendrites (15 μm) [39]. When the solids loading increases, the ice crystal growth is hindered by the high concentration of particles to be rejected and thus the remaining pores become smaller and more homogeneous in size.

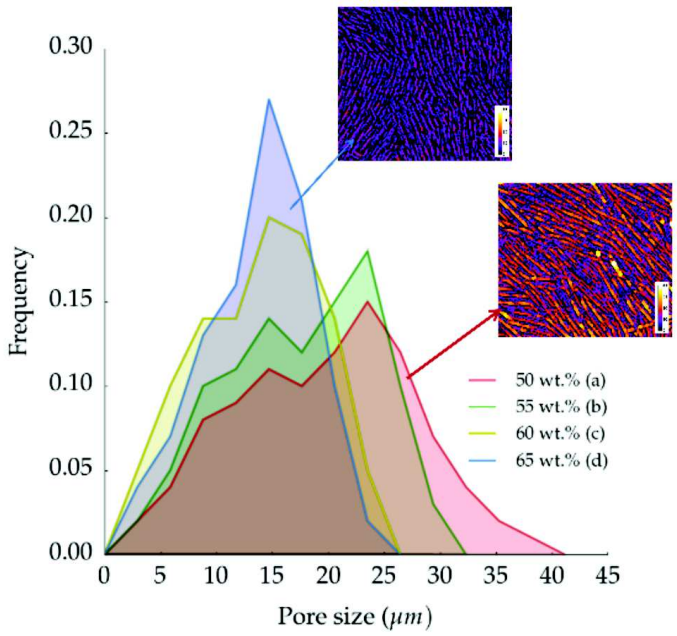

Figure 3.2: Pore size distributions obtained by image analysis for 50 wt.% (red), 55 wt.% (green), 60 wt.% (yellow), and 65 wt.% (blue)

3.3 Wall thickness

Wall thickness can also be controlled by sample processing conditions. Increasing the freezing rate decreases the thickness of the ceramic walls caused by the shrinking space available between the growing crystals. The other parameter that plays an important role in controlling the wall thickness is solids loading, Table 3.1. This effect is not surprising if we consider that when the solids loading increases there are more particles being rejected and packed by the ice crystals. Fig 3.3-A shows how the mean wall thickness becomes larger and the distribution broader when the solids loading increases. In contrast, this behavior seems to be less important when the freezing rate increases. Specimens frozen at 25 °C/min (Fig 3.3-B) have a similar distribution independent of the solids loading and the mean wall thickness remains roughly constant.

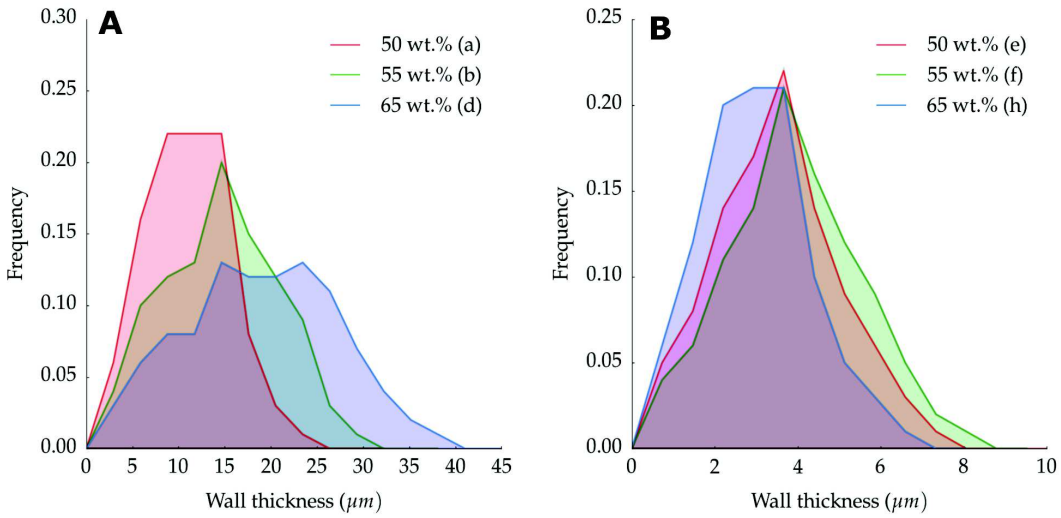

Figure 3.3: Pore size distribution obtained by image analysis of ice templated samples frozen at A) 2 °C/min B) 25 °C/min.

Wall thickness and pore size seem to be directly related. Most publications use the parameter wavelength (λ = pore+wall) to characterize ice templated materials. However, as reported by Lichtner et al. [44], the rate of variation for both microstructural parameters is not equal. In order to identify the dependence of solids loading on the final microstructure, wall thickness and pore size have been plotted separately (Fig. 3.4). In this case, for an increasing solids loading, the pore size decreases roughly 50% slower than the increase in wall thickness. The reason for this variation is because both phenomena are principally controlled by two independent mechanisms:

- **1)** size of the ice crystals (and thus the remaining porosity) is highly sensitive to the solidification speed.
- **2)** wall thickness is mainly determined by the amount and level of densification of particles stacked in between the aforementioned crystals

Therefore, we can tailor the wall thickness through the solids loading and sintering temperature while holding pore size approximately constant adjusting the cooling rate. Also, we conclude that λ, as reported in most literature on ice-templating, is not a sufficient parameter to unambiguously characterize the microstructure.

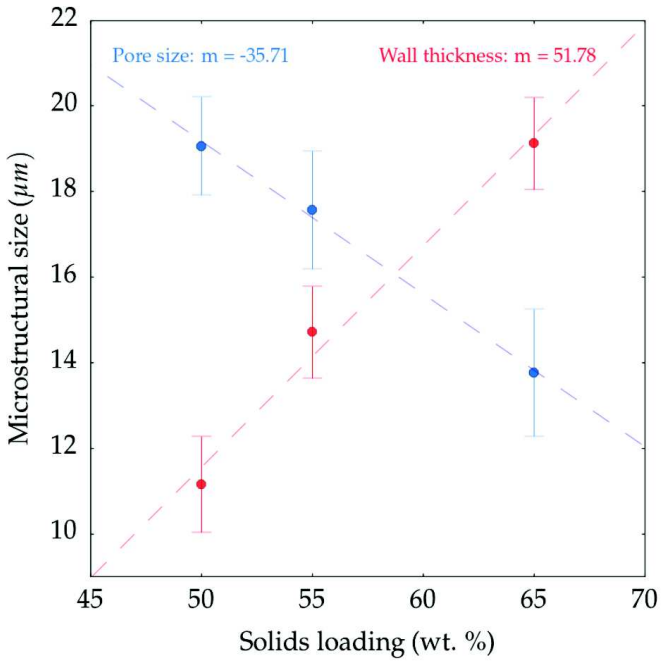

Figure 3.4: Wall thickness and pore size dependency on solids loading. Samples were frozen at 2 °C/min and both microstructural dimensions obtained by image analysis. *m* corresponds to the slope of the trendline.

3.4 Pore shape

Pore morphology is primarily defined by the nature of the solvent [60]. Many solvents have been used before: water [46] [61], camphene [62] [54] [55] [63], TBA, [64] [65] [66], cyclohexane [67]. In the case of water, pores usually exhibit a lamellar morphology, (Fig 3.1). However, the addition of components such as glycerol [37] [68], polystyrene [62], or sucrose [37] can modify the pore size and shape.

The addition of zirconium acetate (ZRA) turns the pore morphology into a honeycomb-like structure with smooth surfaces [51]. Even though the pore morphology changes, the fundamental mechanism for pore formation remains unaltered, and therefore, it is possible to control the pore morphology independently of the total pore volume. However, the addition of ZRA modifies the pore size distribution, even if the solids loading and the freezing rate used are identical to samples processed without ZRA, as Fig. 3.5 shows.

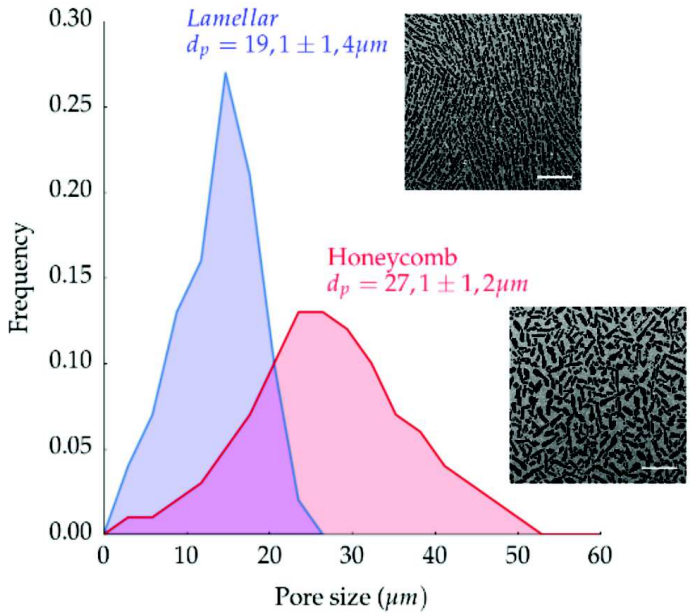

Figure 3.5: Pore size distribution of ice templated structures with ZRA (honeycomb) and without (lamellar). Solids loading used was 65 wt.% and freezing rate 2 °C/min in both cases. Scale bar = 300 μm

In this chapter we covered the most important aspects controlling pore microstructure of ice-templated materials. We identified solids loading, sintering temperature, freezing rate, and additives as the main experimental parameters tailoring total pore volume, pore size, wall thickness, and morphology. In the subsequent chapters the microstructural characterization will be further addressed with special emphasis on the structural features relevant for each chapter's topic.

Chapter 4

Mechanical properties and failure behavior of unidirectional porous materials

Contents

Strength of porous ceramics is usually increased by decreasing the total pore volume, even though it may degrade other functional properties. Morphological parameters such as pore size, shape, or tortuosity can become crucial to maximize the performance while maintaining high strength. For example, a significant improvement in strength can be achieved by engineering anisotropic structures to mechanically reinforce the direction of the main stress. This strategy is used extensively in natural materials such as trabecular bone, cork, or wood [9]. However, most of the techniques conventionally used to produce macroporous ceramics with aligned porosity do not offer this level of flexibility.

Ice-templating provides independent control of the pore architecture (pore volume, size, and morphology) through initial solids loading, cooling rate, or additives. Therefore, ice-templating, as described in Chapters 2 and 3, is used to ptoduce the unidirectional porous ceramics tested here.

As predicted by Gibson and Ashby [10] [20] [69], the architecture greatly determines the mechanical response. Identifying the failure mechanisms that govern fracture can lead to more optimized architectures and better performances. However, ice-templated materials have more complex structures than the models proposed in [10] [20] [69]. Recently, different groups studied the mechanical properties of ice-templated materials based on their pore structure. For example, Ojuva et al. [70] investigated the effect of solids loading and freezing temperature on zeolite materials and related the compressive strength to the pore aspect ratio. Porter et al. [59] found a similar result in TiO_2 by controlling the pore size through the polyethylene glycol (PEG) viscosity, pH, and isopropanol alcohol (IPA) concentration. Hunger et al. [71] described the mechanical behavior of a chitosan-hydroxiapatite composite using an hybrid model accounting for the unidirectional pores and the porosity in the walls. However, these studies are limited to a narrow porosity range (>80%) and a compiling work describing the microstructural effects on compressive strength of unidirectional porous materials is still lacking.

Our objective in this chapter is to characterize the compressive strength of ice-templated ceramics in a broad porosity range and link their mechanical behavior to the architecture. Also, we will discuss the effects of pore volume, size, and shape on the failure mechanisms, to assess the validity of the Ashby models for the prediction of the compressive strength of unidirectional porous materials.

4.1 Microstructures evaluated

We used the knowledge gathered in Chapter 3 to process ice-templated materials with a controlled pore volume, size, and shape. For the sake of comparison, Fig. 4.1 shows representative microstructures at a given pore volume (around 51%) and Fig. 4.2 shows their pore size distributions. Although all of them were ice-templated with the same solids loading, and hence same total pore volume, variations in the experimental conditions such as cooling rate (Fig. 4.1-b) and additives (Fig. 4.1-c) caused the differences in the pore size distributions.

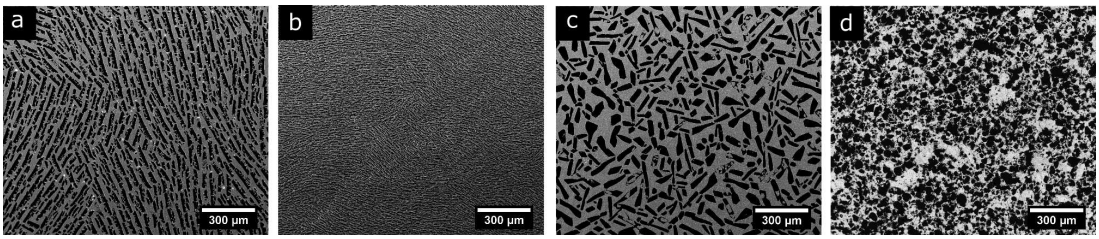

Figure 4.1: Micrographs of ice-templated samples a) frozen at 2°C/min, b) frozen at 25°C/min, c) frozen at 2°C/min with zirconium acetate (ZRA), and d) made by pore formers. In all cases the sintering temperature was 1400°C and the total pore volume was around 51%.

Additionally, a set of samples with isotropic porosity (Fig. 4.1-d) was also prepared by

organic burn-out to assess the effect of pore directionality. These specimens were prepared following the processing protocol typically used in these type of materials. Since the macroporosity obtained by this technique is a replica of the organic part originally mixed with the ceramic powder, the total pore volume is controlled by the organic-ceramic ratio. Pores are homogeneously dispersed with no preferential orientation, leaving an isotropic material. The processing parameters (volume and size of organic, and sintering temperature) were adjusted to obtained a total pore volume and mean pore size comparable to sample Fig. 4.1-a. However, Fig. 4.2 shows that the pore size distribution is remarkably broader in the isotropic samples compared with the ice-templated.

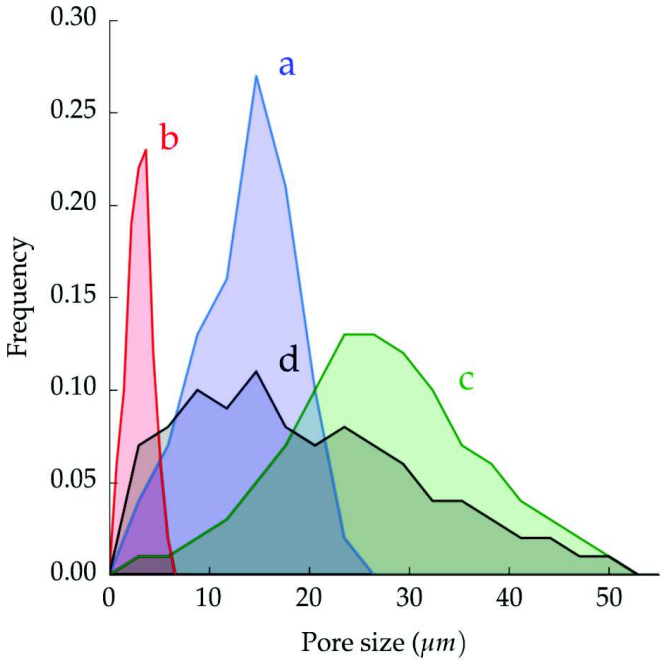

Figure 4.2: Pore size distribution obtained by image analysis of samples shown in Fig. 4.1.

4.2 Prediction by mechanical models

The most widely used models to predict the mechanical response of cellular materials were developed by Gibson and Ashby [10] [69]. The models differentiate between three morphologies: open-cell, closed-cell, and honeycomb (Fig. 4.4). Although they have been applied to different mechanical properties such as fracture toughness, creep, or Young modulus, this work only covers the compressive strength described by:

- Closed-cell (brittle crushing)

$$\sigma = \sigma_p \left(C_6 \left(\phi \frac{\rho^*}{\rho_0} \right) + C_6'' \left(1 - \phi \right) \frac{\rho^*}{\rho_s} \right) \tag{4.1}$$

where $C_6 = 0.65$ and $C_6'' = 1$ are geometric constants determined empirically, ϕ represents the solid fraction in the edges, ρ_s and ρ^* are the apparent density of the dense and cellular material respectively, and σ_p the modulus of rupture of the solid material within the walls.

- Open-cell (brittle crushing)

$$\sigma = \sigma_0 C_4 \left(\frac{\rho^*}{\rho_0}\right)^{3/2} \tag{4.2}$$

with $C_4 = 0.2$, and where σ_p, ρ_s, and ρ^* have the same meaning as in the closed-cell model.

- Honeycomb (out of plane)

$$\sigma = 6E_s \left(\frac{\rho^*}{\rho_0}\right)^3 \tag{4.3}$$

where E_s is the Young's modulus of the corresponding dense material, and ρ_s and ρ^* are again the apparent density of the dense and cellular material respectively.

Fig. 4.4 shows the normalized compressive strength of the ice templated and pore formers samples processed in this work along with those obtained by other processing methods (replica, foaming, and pore formers) [32]. In all cases, the strength was normalized by the flexural strength of the bulk material because bending has been identified as the main failure mechanism in cellular materials within the porosity range studied [72]. This normalization allows us to isolate the effect of pore microstructure as we assess the mechanical models.

Fig. 4.4 also shows that the strength of specimens processed by either foaming or pore formers fell in the broad range predicted by the closed (Eq. 4.1) and open cell models (Eq. 4.2). However, the samples obtained by the replica method always have a lower strength value than that predicted by Eq. 4.2 due to the presence of microstructural defects in the struts. The burn-out of the organic template creates this type of flaw that weakens the structure [73].

On the other hand, ice-templated architectures are better described by the honeycomb out-of-plane model (Eq. 4.3). Unlike the compressive strength of cellular materials, Eq. 4.3 is normalized by the Young modulus of the bulk material. Fig. 4.3 shows a broken ice-templated sample that failed perpendicular to the external load at the middle of the specimen, where the stresses reach the maximum value, and indicative of a buckling fracture. The combination of anisotropic porosity with interlocking struts between the main walls, characteristic of the ice-templated materials, prevent the lateral motion and the shear stresses. This structure becomes more prone to collapse by buckling of the walls instead of localized bending as it was identified in foams [10] [74] [75]. Buckling

also has been reported to be the main failure mechanism in different ice-templated materials [70] [71] and in other unidirectional porous materials processed by wood pyrolisis [76], extrusion [77], or 3D printing [78].

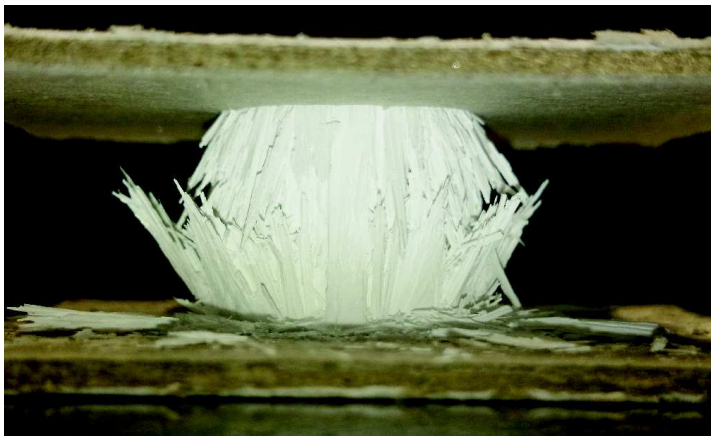

Figure 4.3: Detail of a buckling fracture in an ice-templated sample with 50 wt.% solids loading, frozen at 2°C/min, and honeycomb pore morphology.

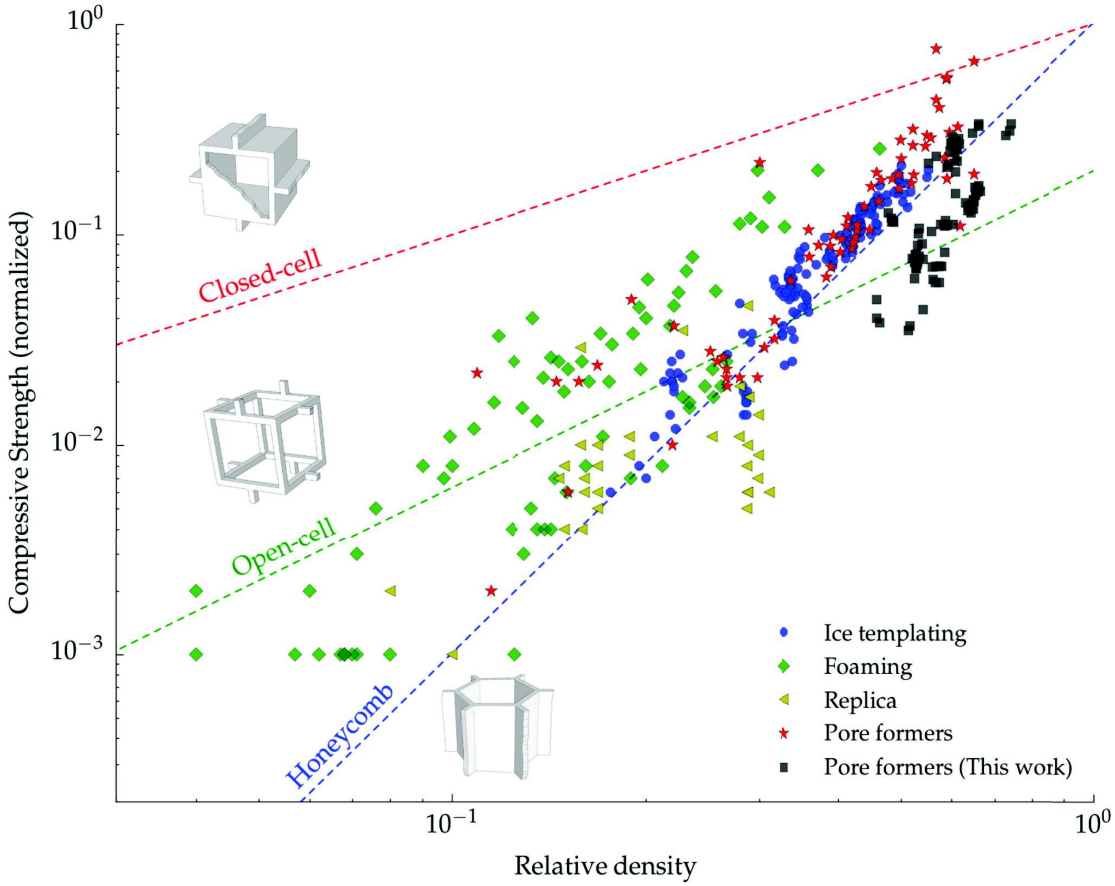

Figure 4.4: Normalized compressive strength versus relative density for different macroporous ceramics. Open-cell and closed-cell models were normalized by the flexural strength of the bulk material, unlike Honeycomb out-of-plane model that was normalized by the Young modulus of the fully dense material. The solid lines represent the models proposed by Ashby: Closed-cell (red) Eq. 4.1, Open-cell (green) Eq. 4.2, and Honeycomb out-of-plane (blue) Eq. 4.3. Blue points correspond to ice-templated samples processed in this work and the rest of the experimental points have been extracted from [32].

Fig. 4.5 shows the compressive strength obtained experimentally versus the strength predicted by Eq. 4.3 for three sets of ice templated samples: lamellar frozen at 2°C/min (Fig. 4.1-a), lamellar frozen at 25°C/min (Fig. 4.1-b), and honeycomb frozen at 2°C/min (Fig. 4.1-c). The model describes the compressive behavior remarkably well for both pore shapes. Although the addition of zirconium acetate modifies the pore morphology towards a honeycomb structure, the ceramic walls are still continuous and oriented parallel along the direction of the load, and therefore the predominant failure mechanism is still buckling. As we showed previously [3], when the continuity of the walls decreases, like in the dendritic porosity created when camphene is used as a solvent, Eq. 4.3 is not a good descriptor of the strength. The validity of the model is thus mainly determined by the directionality and continuity of the walls rather than their cross sections. Nevertheless, the Gibson and Ashby models were initially derived from the response of an idealized unit cell to a stress and do not consider microstructural effects such as particle

size, microstructure of the struts, interaction between pores, or pore size. The effects of microstructure can be observed in Fig. 4.5 where Eq. 4.3 underestimates the strength of ice-templated samples with smaller pores (3-5 μm). This effect is particularly remarkable at high relative density where the amount of energy stored during compression is higher and materials tend to be more brittle. In contrast, at low values of relative density, the total pore volume and the presence of microstructural defects increase and favor the progressive damage by buckling of the struts and the fit by Eq. 4.3 becomes more accurate.

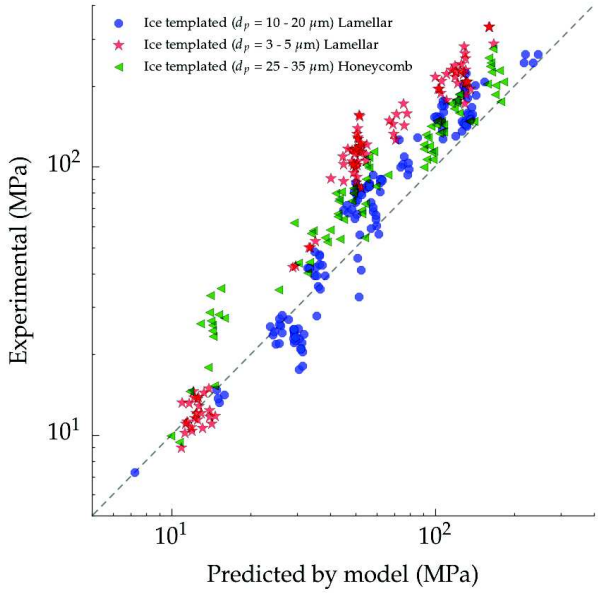

Figure 4.5: Parity plot comparing the experimental and the theoretical strength predicted by Eq. 4.3. The three sets of samples have been ice-templated at: 2°C/min with lamellar morphology (blue), 2°C/min with honeycomb morphology (green), and 25°C/min with lamellar morphology (red).

4.3 Compression tests

Compressive strength is the most reported mechanical property for ice-templated materials due to its simplicity in testing and sample preparation. Nonetheless, it is difficult to compare with the results in the literature because structures are notably different in terms of size, morphology, directionality, and even microstructure of the walls. However, it is possible to point out several trends common in the majority of samples.

4.3.1 Effect of solids loading, pore size, and pore morphology

Representative stress-strain curves recorded during the compression test are shown in the inset of Fig. 4.6 for three ice templated samples with different pore volumes, an average pore size of 10-20 μm, and a lamellar shape. All specimens were tested with

the pores aligned in the direction of the applied load. The P(%)=45% and 62% samples exhibited an initial linear stage up to a sudden rupture, typical of brittle behavior. In contrast, samples with higher porosity (P(%)=71%) presented a cellular-like rupture commonly observed in ceramic foams: after an initial elastic phase, the stress reaches a steady value caused by the progressive collapse of the struts [9].

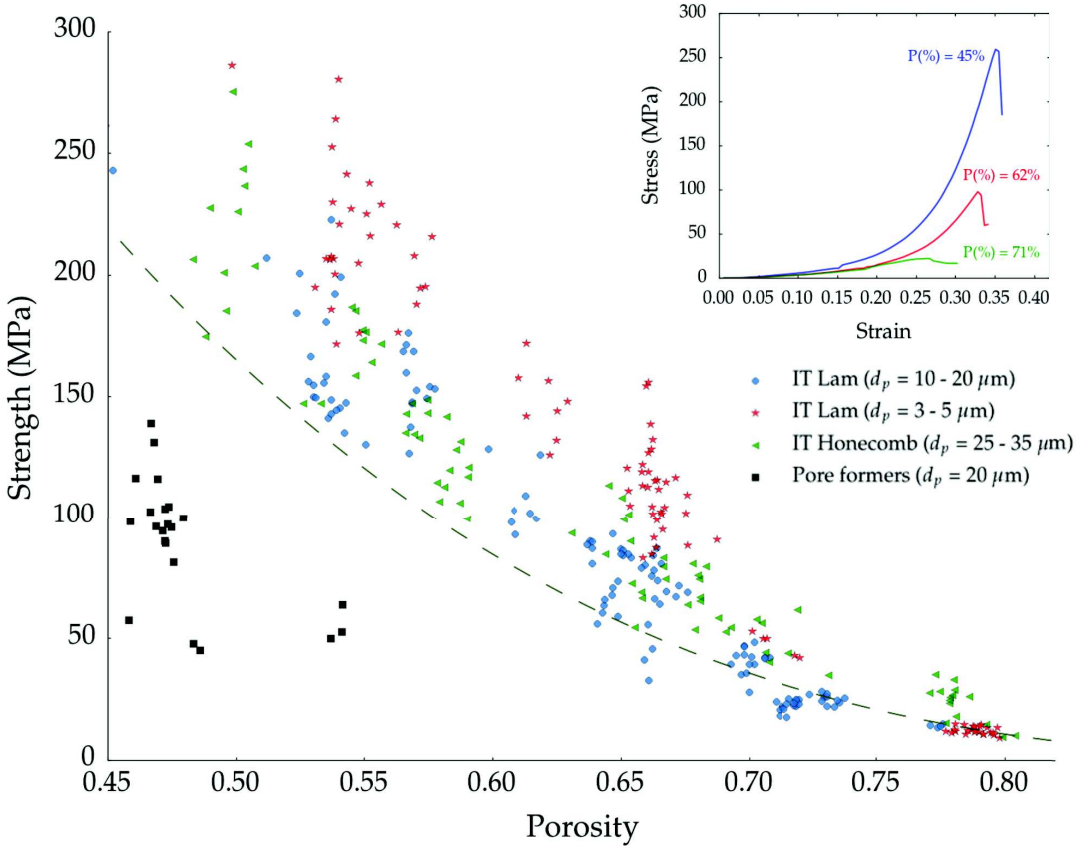

Figure 4.6: Compressive strength dependence on porosity in ice templated for samples frozen at 2 °C/min (blue), 25 °C/min (red), and with a honeycomb morphology (green). Isotropic samples made in this work by sacrificial method are also represented (black). The dashed line corresponds to the Honeycomb out-of-plane model shown in Eq. 4.3.

Fig. 4.6 also shows the effect of total pore volume (from 45% to 80%), size (3-5 μm and 10-20 μm), shape (lamellar and honeycomb), and directionality (ice-templated and pore formers) on compressive strength. As expected, when the total pore volume decreases the compressive strength increases independent of the pore microstructure and architecture.

Although samples with isotropic porosity have lower strength than the ice-templated ones, we must be careful to evaluate the particular role of pore directionality. As Fig. 4.4 shows, the structures that fail by buckling (honeycomb out-of-plane) tend to collapse at higher strength than those that fail by localized bending or shear (open-cell) at relatively low porosity content. The parallel alignment of the walls with the load al-

lows a more optimal distribution of the stresses and prevents the bending of the struts at lower loads. Therefore, we can hypothesize than the optimized microstructure of ice-templated materials explains this strength increment. However, there are other microstructural factors that also can play an important role on the mechanical performance of the isotropic samples such as the broader pore distribution (Fig. 4.2). The presence of thicker isolated walls and larger pores are features that certainly might impact the strength through the existence of weaker points and stress concentrators.

Samples with lamellar and honeycomb structure followed a similar trend, and therefore compressive strength seems to be unaffected by the pore morphology. In contrast, samples with smaller pore size have a higher strength than their counterparts with larger pores and similar pore volume. This effect becomes less important when the pore volume increases, even reaching a point (around 75%) where the strength seems unaffected by the pore size. Although the influence of pore size has been extensively reported in different types of porous ceramics [59] [57] [79] [80] [81], the main cause of this behavior is unclear and it might result from a combination of factors. One of the main contributions could be related with the reduction of the volume of the struts. For a constant pore volume, a decrease in pore size leads to a wall thickness reduction, affecting the probability of finding a catastrophic defect and the strength [82]. The strength of ceramics is strongly related with the volume of the material solicited, it is therefore more convenient to describe their mechanical properties based on the distribution of the solid parts (struts) rather than the organization of the voids (pores). For this reason it is more accurate to refer this strengthening effect as a wall thickness effect instead of pore size. A second contribution could be related with the pore organization perpendicular to the solidification front. Samples frozen at higher cooling rates exhibited a higher degree of connectivity that aids preventing walls from buckling and/or shearing. [**?**].

Interestingly, when the pore volume increases the experimental strength values tend to those predicted by the honeycomb out-of-plane model, regardless of the pore structure. This behavior might be related with the transition between failure mechanisms (brittle and cellular-like fracture) [72]. When the pore volume increases above a certain value (typically above 60%), samples tend to fail progressively after the local buckling of the struts (Fig. 4.7-b) and pore shape and size become secondary parameters to optimize to increase the strength. When the pore volume decreases, the material fails in a brittle manner with cracks propagating parallel to the load (Fig. 4.7-a), and microstructural parameters like wall thickness distribution are of primary importance to increase the strength with no further reduction on the pore volume.

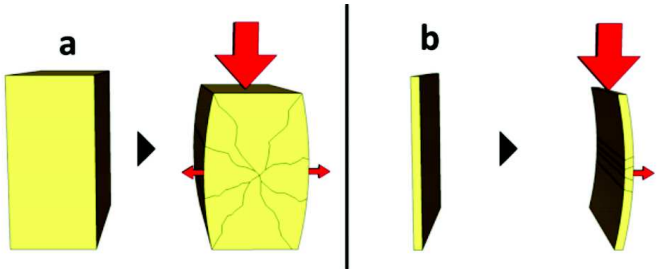

Figure 4.7: Representation of the different failure mode of the walls. a) Brittle fracture observed at low pore volume and b) Buckling fracture observed at high pore volume. Image extracted from [83].

Finally, we assessed whether the compressive behavior of unidirectional porous materials is caused by the pore structure and it is not simply a consequence of the material choice. To answer this question we followed the same ice-templating process and mechanical characterization in a second material, in this case $Ca(Ti,Fe)O_3$ CTF. Fig. 4.8 shows the variation of normalized compressive strength with porosity for both materials. Specimens ice-templated with CTF as raw material followed the same trend as YSZ. This observation rules out the possibility that the failure mechanism previously described is caused by an intrinsic effect of the material choice. Instead, the fact that CTF follows the same trend confirms that the overall trends in strength are governed by the pore architecture. Further, it also validates the use of YSZ as a model material where the results can be extrapolated to other material systems.

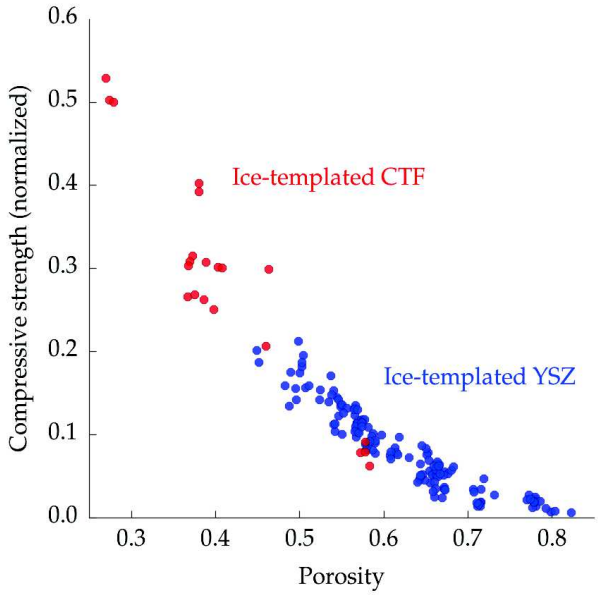

Figure 4.8: Compressive strength dependence on porosity for ice-templated samples frozen at 2°C/min in YSZ (blue) and CTF (red). The strength data was normalized by the flexural strength of the respective bulk material

4.3.2 Effect of sintering temperature

Total pore volume can also be tailored by the sintering temperature. Fig. 4.9-A shows the effect of solids loading and sintering temperature on total pore volume P(%). Although, both parameters can modify P(%), the nature of the variation is different in each case. The spaces between the walls (interlamellar porosity) are determined for the most part by the ice templating process and it is a direct consequence of the solids loading and the sublimation of the ice crystals. Alternatively, porosity in the ceramic walls (intralamellar porosity) is mainly determined by the densification within the walls and therefore controlled by the sintering temperature. The SEM micrographs in Fig. 4.9-A show the microstructural evolution in the walls when the sintering temperature increases from 1300°C to 1400°C for a given solids loading (65 wt.%). At 1300°C (Fig. 4.9-a) the residual porosity was estimated by image analysis to be around 24%, significantly higher compared to the 12% of the samples sintered at 1400°C (Fig. 4.9-c).

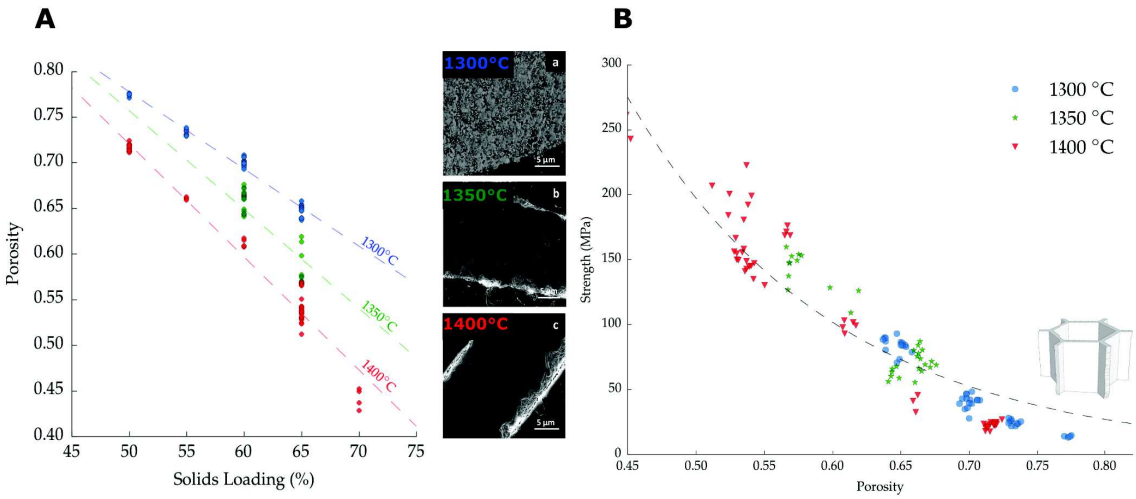

Figure 4.9: (A) Effect of solid loading and sintering temperature on % porosity and evolution of wall densification. (B) Relation between compressive strength and total pore volume for ice-templated samples frozen at 2 °C/min, with a pore size in the range of 10-20 μm, and sintered at different temperatures (1300-1400°C). Dashed line represents the honeycomb out-of-plane model, Eq. 4.3.

The higher densification of the walls at 1400°C increases the observed shrinkage. Samples sintered at 1300°C exhibited a radial shrinkage of 17%, significantly lower than the 21% obtained at 1400°C. At higher sintering temperatures, the densification of the walls drives the shrinkage of macropores and therefore the pore size distribution becomes narrower. This behavior can be observed in the image analysis performed at samples sintered at 1400°C and 1300°C and shown in Fig. 4.10.

Interestingly, the relative reduction of pore volume caused by the sintering temperature is remarkably different depending on the initial wall thickness, and hence the particle concentration used. For example, samples in Fig. 4.9-A with 65 wt.% exhibit a porosity

reduction around 20% when the sintering temperature increases from 1300°C to 1400°C. In contrast, at 50 wt.% solids loading the reduction of the total porosity is around 8% for the same variation in temperature.

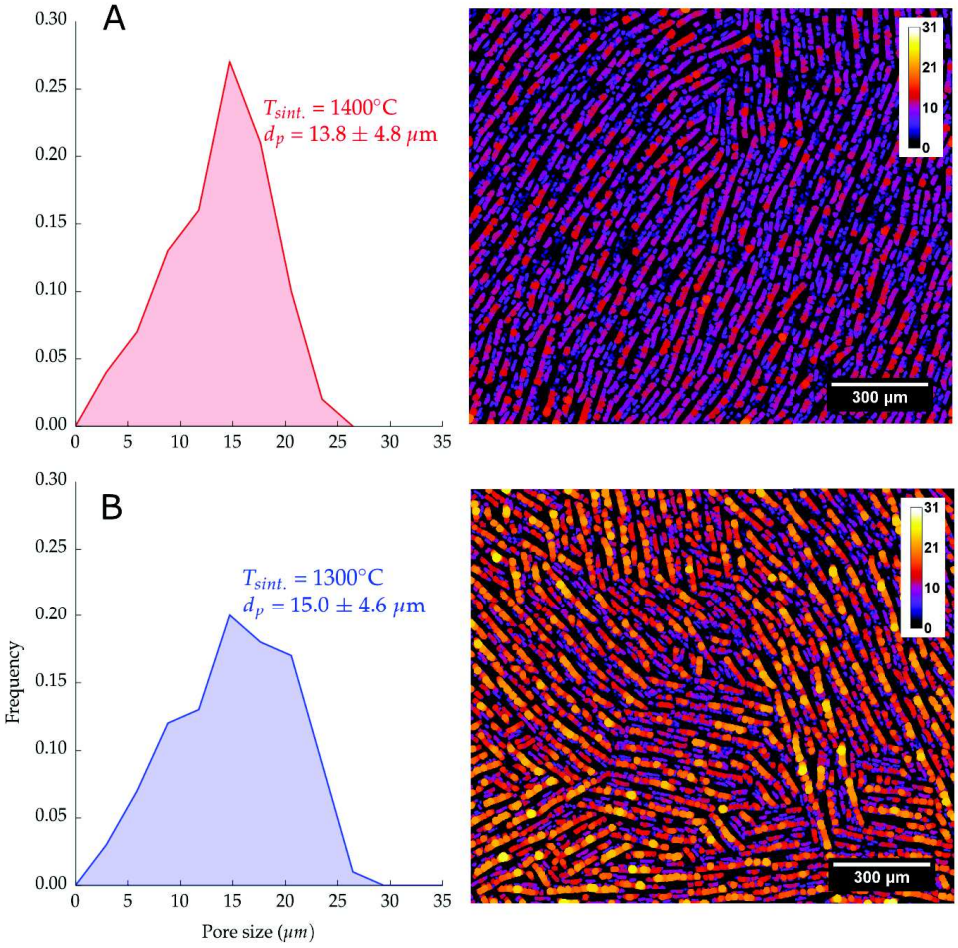

Figure 4.10: Image analysis showing the pore size population of ice templated samples frozen at 2 °C/min, 65 wt.% solids loading and sintering temperature A) 1400°C B) 1300°C.

However, no additional increment in the strength has been observed caused by the reduction on the residual porosity in the walls at a given total pore volume, (Fig. 4.9-B). All the samples, independently of the sintering temperature, followed the same relationship between strength and porosity as predicted by Eq. 4.3. This suggests that the compressive strength of ice-templated materials is determined mainly by the total pore volume, rather than the strength of the individual struts. This result is contrary with Li et al. [84], that reports an exclusive effect of interlamellar porosity on the strength of ice-templated materials.

4.3.3 Anisotropic strength

Ice templated materials are characterized by an anisotropic strength behavior originated by their highly directional porosity. Fig. 4.11 shows the stress-strain curves obtained for two representative samples with the same total porosity and pore size but loaded parallel and perpendicularly to the pores. While the first has the typical brittle behavior described previously, the former exhibits an initial linear state followed by a progressive crushing of the struts, similarly as it has been observed in cellular materials. Unlike parallel samples where the majority of the walls withstand the load, in the perpendicular direction the ceramic bridges between the struts play the most important role.

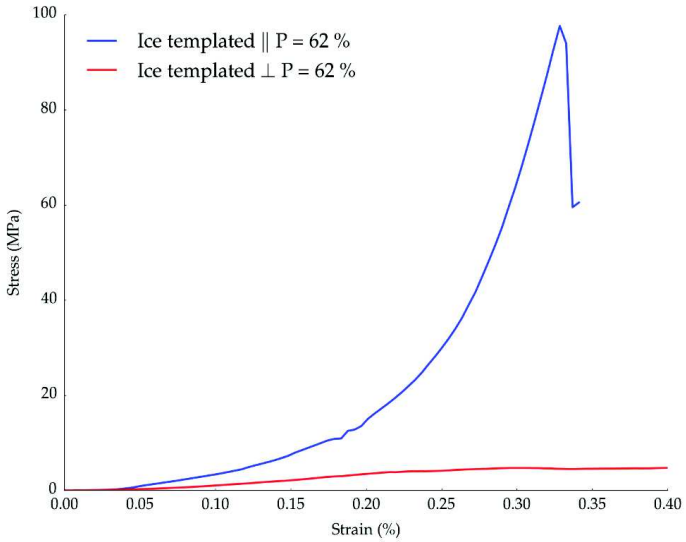

Figure 4.11: Representative stress-strain curves for two ice-templated specimens loaded parallel (blue) and perpendicular (red) to the pores. In both cases freezing temperature was 2°C/min. The solids loading, and hence porosity, is the same in both cases highlighting the high anisotropic behavior.

Fig. 4.12 shows the crushing strength in ice templated samples measured in both directions. As expected, samples tested perpendicularly exhibit lower values of strength (almost one order of magnitude) compared with their counterparts loaded in the strong direction. Also, the increase in resistance obtained by decreasing the porosity is less important than the parallel direction. The reason is because reducing the solids loading does not increment substantially the perpendicular living cross section in the same way as it does in the parallel one. One possible solution to reinforce the weak direction might be increasing further the connectivity between walls using additives. This strategy would increase the strength without a significant impact in the total porosity [37].

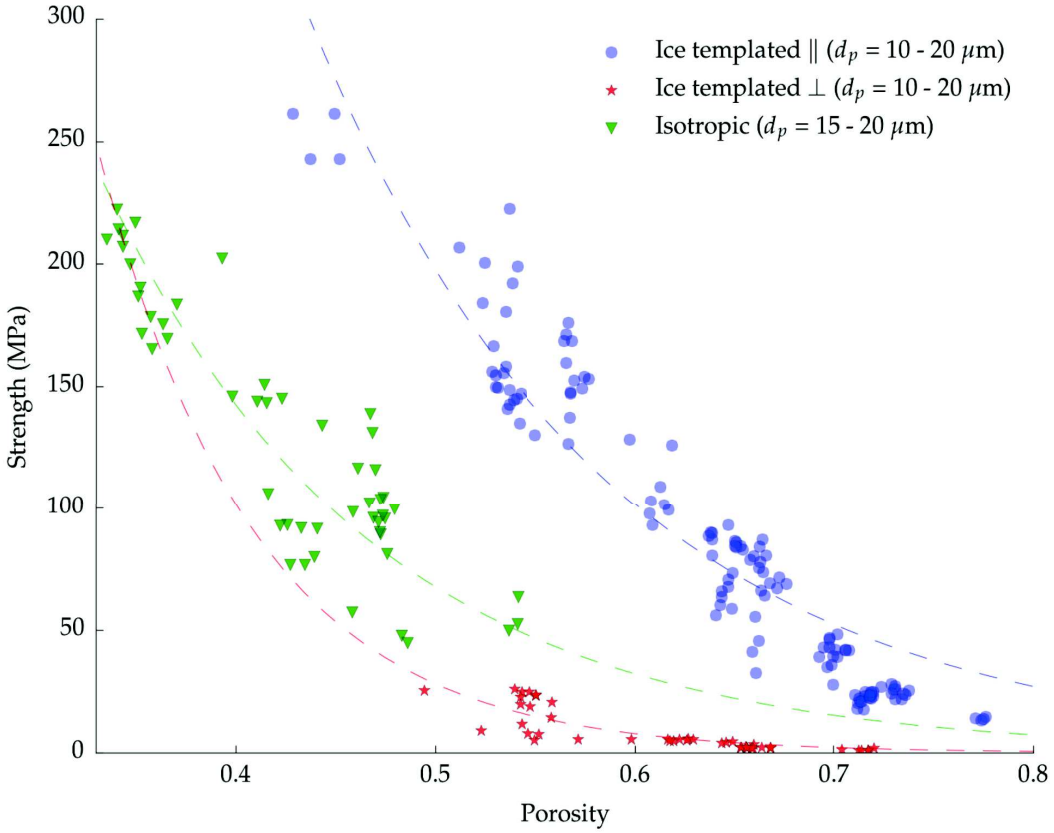

Figure 4.12: Effect of pore anisotropy in compressive strength. Ice-templated samples with pores parallel to the load (blue), perpendicular (red), and samples with isotropic porosity obtained by pore former (green). Dashed lines represents the exponential fit.

4.4 Mechanical reliability

4.4.1 Why is reliability important?

For brittle solids like ceramics, the mean strength is not an adequate predictor of performances because there is an inherent variability of strengths measured across seemingly identical samples. This variability is caused by the random nature of defects created during processing, handling, or service. Since the strength of a material is described by a distribution rather than a single value, it is necessary to characterize it using a probabilistic approach. This is particularly important in applications like SOFC or OTM where hundreds or thousands of individual macroporous elements must be combined and the failure of a single element could cause the entire module to fail.

Although different models have been proposed to describe the strength of brittle materials [85] [86], the Weibull analysis is the most extensively used [87]. It is based on the assumption that the catastrophic failure of the material is triggered by the weakest

defect (i.e. *weakest link hypothesis*), and that these defects have probabilistic population densities in real materials that result in probabilistic strength distributions. One of the main implications of this assumption is that reducing the population of flaws, for example by reducing the sample size, will inevitably lead to an increase in strength (i.e. *size effect*). Characterizing the strength distribution of a ceramic material and linking it to processing parameters and microstructural features is therefore of primary importance for industrial application [88]. This is particularly important for macroporous ceramics because the mean strength of the materials is reduced by introducing the porosity that enables the desired functional properties.

The reliability of macroporous ceramics has been characterized for materials processed by different techniques like partial sintering [89], organic template [90], or robocasting [81] [91]. However the particular impact of porosity on Weibull modulus is still not fully understood and frequently assumed to be the same as strength. The main problem is that most of the techniques do not provide an independent control of the different features of the porous microstructure and therefore can lead to a biased conclusions. For example, increasing pore volume frequently causes an increase in the pore size hindering the assessment of the individual effect of each parameter.

As it has been discussed in section 4.3, the strength of ice-templated materials has been extensively studied. However there is a lack of studies measuring their reliability. The only work that evaluates this parameter was performed by Ojuva et al. [70] in ice-templated zeolites. They measured the effect of solids loading and cooling rate on Weibull modulus and estimate the probability of survival. However, the reduced number of samples tested per condition hinders a clear interpretation of the results and a further link between microstructure and reliability.

The purpose of this section is to determine the main microstructural parameters that control the reliability and strength of unidirectional porous materials. A Weibull analysis was applied to the compressive strength data gathered in section 4.3 and, afterwards, the suitability to characterize the fracture behavior by this method will be discussed.

4.4.2 Weibull analysis

Fig. 4.13 shows the cross sections of the ice-templated samples representative of each group studied. Table 4.1 summarizes the most important structural features and the experimental conditions used. Fig. 4.13-b (*S2* in Table 4.1) was used as a reference material to evaluate the impact on reliability caused by microstructure variations such as total pore volume (Fig. 4.13-a and S1), pore size (Fig. 4.13-c and S3), porosity in the walls (Fig. 4.13-d and S4), and pore morphology (Fig. 4.13-e and S5).

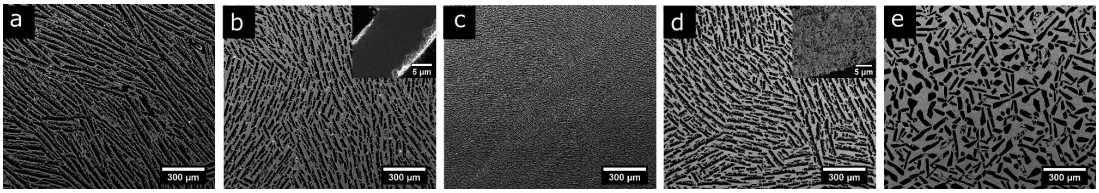

Figure 4.13: SEM micrographs obtained under the conditions specified in Table 4.1. a) *S1*, b) *S2*, c) *S3*, d) *S4*, and e) *S5*.

Ref.	Samples	Solids loading(wt.%)	$P(\%)_{total}$	$P(\%)_{inter}$	$P(\%)_{intra}$	Morphology	Freezing rate	Sintering temperature	Mean d_p (μm)	Mean WT (μm)
S1	21	50	$71,7 \pm 0,4$	$59,7 \pm 0,4$	$12,0 \pm 0,6$	Lamellar	2°C/min	1400°C	$20,0 \pm 8,5$	$11,2 \pm 4,5$
S2	23	65	$53,7 \pm 1,6$	$40,8 \pm 2,1$	$12,9 \pm 2,6$	Lamellar	2°C/min	1400°C	$13,7 \pm 4,8$	$19,1 \pm 8,2$
S3	15	65	$54,5 \pm 1,2$	$40,0 \pm 0,8$	$14,5 \pm 1,4$	Lamellar	25°C/min	1400°C	$3,1 \pm 1,2$	$3,0 \pm 1,3$
S4	15	65	$70,5 \pm 0,4$	$46,4 \pm 0,6$	$24,1 \pm 0,7$	Lamellar	2°C/min	1300°C	$15,0 \pm 5,6$	$17,1 \pm 8,1$
S5	20	65	$53,1 \pm 0,7$	$39,1 \pm 1,7$	$14,0 \pm 1,8$	Honeycomb	2°C/min	1400°C	$27,3 \pm 9,8$	$37,2 \pm 16,7$

Table 4.1: Summary of the most relevant structural features of images in Fig. 4.13. d_p represents the pore size and WT the wall thickness, both obtained by image analysis.

Table 4.2 reports the mean wall thickness (WT) of the samples along with the results of the two different curve fitting procedures applied, ordinary least squares (OLS) and Bayesian fit (MCMC). Fig. 4.14 shows the experimental strength values obtained for each group of samples and the ordinary squared fit (OLS) to the data. The values of R^2_{ols} obtained for all the groups are higher than 0,85 and P-values of the OLS fits were 0,00 and are not reported in the table. The combination of null P-value$_{ols}$ and $R^2_{ols} > 0,85$ indicates that the data is well described by the linearized form of Eq. 2.3 for all samples. This observation implies that the fracture behavior of this type of materials is adequately described by the Weibull stastical approach. It may also imply that the underlying *weakest link hypothesis* may apply to these materials. Although the *weakest link hypothesis* assumes that the density of flaws has to be low enough to neglect the interaction between pores [92] in dense materials, our observations are in agreement with several authors [93] [94] also reporting that the Weibull distribution successfully describes the scattering of strength in macroporous ceramics even at high porosity (around 60%) [95].

Ref.	Mean WT (μm)	$\bar{\sigma}$ (MPa)	m_{ols}	m_{Bayes}	$\sigma_{0\,ols}$ (MPa)	$\sigma_{0\,Bayes}$ (MPa)	R^2_{ols}	P_{Bayes}
S1	$11,2 \pm 4,5$	$22,9 \pm 2,5$	$10,7 \pm 0,5$	$11,6 \pm 0,4$	23,8	$23,7 \pm 0,1$	0,96	0,796
S2	$19,1 \pm 8,2$	$170,2 \pm 22,0$	$9,0 \pm 0,8$	$8,4 \pm 0,5$	178,9	$176,9 \pm 1,0$	0,85	0,816
S3	$3,0 \pm 1,3$	$198,2 \pm 16,9$	$13,2 \pm 1,2$	$12,7 \pm 0,8$	202,2	$206,3 \pm 0,8$	0,91	0,514
S4	$17,1 \pm 8,1$	$40,3 \pm 5,0$	$8,7 \pm 0,6$	$9,2 \pm 0,5$	43,4	$43,0 \pm 0,2$	0,95	0,264
S5	$37,2 \pm 16,7$	$122,0 \pm 21,5$	$6,6 \pm 0,5$	$5,9 \pm 0,3$	133,3	$129,3 \pm 1,1$	0,91	0,777

Table 4.2: Summary of the results of the different curve fitting procedures (OLS and Bayes)

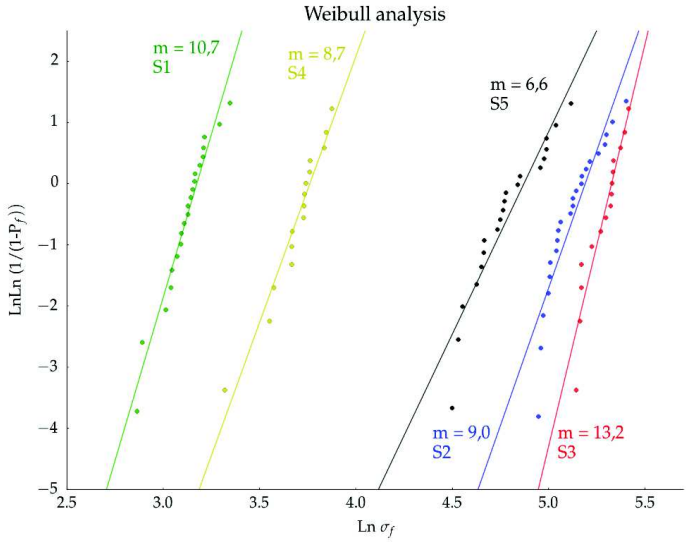

Figure 4.14: Weibull strength distributions of groups described in Table 4.2. The solid line represents the OLS fit to the data.

Fig. 4.15 shows the probability of failure (P_f) measured by Eq. 2.3 and using the Weibull parameters σ_0 and m obtained through OLS and Bayesian fits (Table 4.2). The Bayesian P-value was used as an indicator of the fit and it is reported in Table 4.2. By definition Bayesian P-values range between 0 and 1 and values >0,975 or < 0,025 indicate a poor fit to the data. In this case, the measured Bayesian P-values fall outside this range and indicate that the model and modeled m and σ_0 parameters fit the data well and can be used in the prediction of the P_f of this materials.

As Fig. 4.15 shows, when the Weibull modulus increases, the slope of the P_f function becomes higher and the stress range between low and high probability of failure shrinks. This narrowing effect means that the material is more reliable, i.e. the statistical spread of sample strengths is relatively narrow around the mean value of strength distribution. This means these samples can be used in operational conditions close to the measured mean strength. Nevertheless, it is important to point out that the reduction in the stress range is refereed as the relative reduction between the maximum and minimum strength and not to the absolute number.

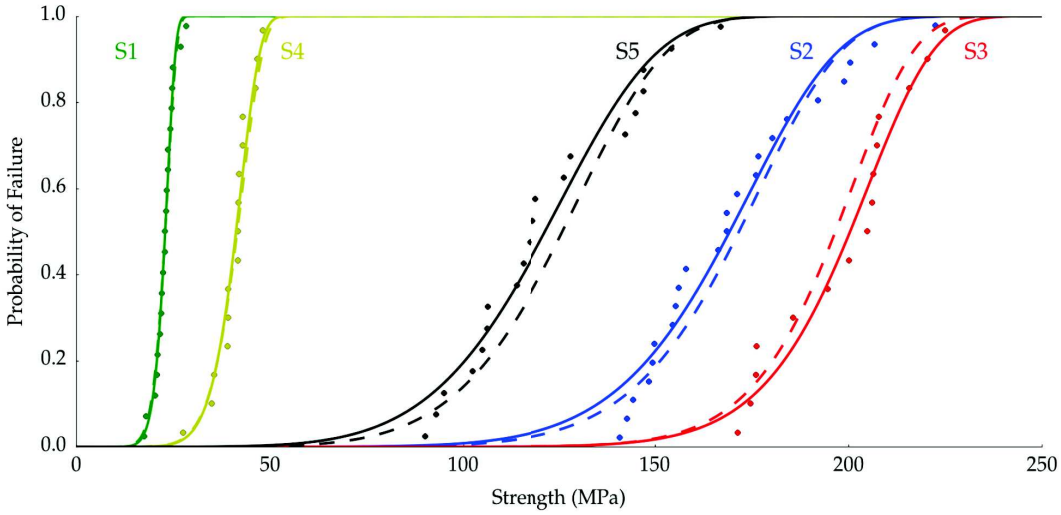

Figure 4.15: Probability of failure prediction based on the parameters σ_0 and m shown in Table 4.2. The dotted lines are based on the OLS fitted parameters and the solid lines use parameters from the nonlinear Bayesian fit.

The set of samples with the smallest pore size (*S3* in Table 4.2) exhibited the highest mean strength (198,2 MPa). The effect of increasing strength with decreasing pore size has been reported in other ice-templated materials [37] [70] [59] and in other types of cellular structures [72] [80] [96] [97] [98] [99]. Brezny et al. [82] proposed that one of the main contributions is caused by the reduction of the volume of the struts and, thus, affecting the probability to find a catastrophic defect. *S2*, *S3* and *S5* in Table 4.1 have a comparable $P(\%)_{inter}$ and $P(\%)_{intra}$ because they have been sintered at the same temperature and the solids loading of the initial slurry was also the same. However, the mean pore size (d_p) was modified by either decreasing the freezing rate (*S3*) or changing the pore morphology (*S5*). Since the $P(\%)_{total}$ is similar in the three groups, the specimens with larger pores must also exhibit a broader wall thickness distribution.

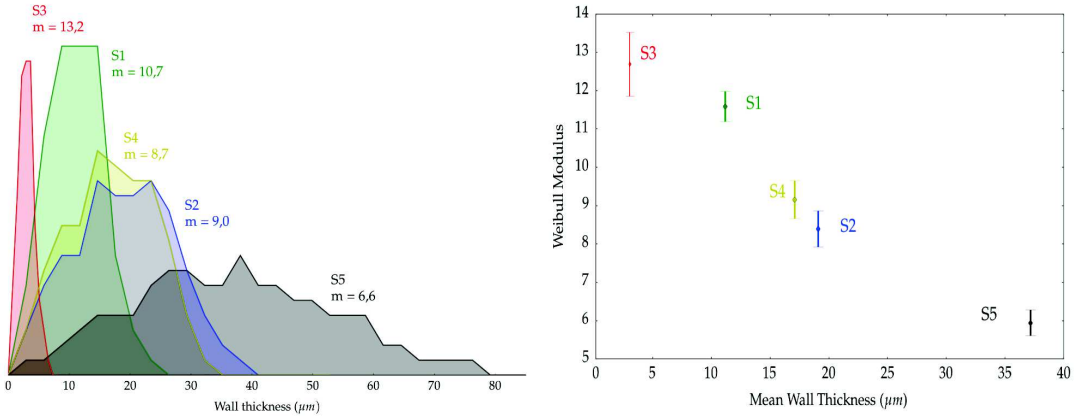

Figure 4.16: Wall thickness distribution of samples shown in Fig. 4.13 and representative of groups in Table 4.2. (Inset) Weibull modulus as a function of wall thickness. The Weibull modulus and credibility interval are taken from the Bayesian nonlinear fitting procedure.

As Table 4.2 and Fig. 4.16 show, a decrease in the mean wall thickness causes an increase in the Weibull modulus. This behavior is consistent with the classical Weibull approach (*weakest link theory*) that states that the relationship between the strength of two brittle samples, σ_1 and σ_2, with different volumes, V_1 and V_2, is related with the Weibull modulus *m*, Eq. 4.4 [100].

$$\frac{\sigma_1}{\sigma_2} = \left(\frac{V_2}{V_1}\right)^{1/m} \tag{4.4}$$

The Weibull modulus can be tailored by the individual volume of the struts. Fig. 4.16 shows that shrinking the wall thickness distribution leads to an increase of the reliability of the ice-templated samples, regardless of the processing conditions used. This control over the Weibull modulus could be achieved by either solids loading (*S1*), freezing rate (*S3*), sintering temperature (*S4*), or additives in the initial slurry (*S5*). Interestingly, *S2* and *S4* have a similar wall thickness distribution and Weibull modulus, although the percentage of porosity in the walls ($P(\%)_{intra}$) is almost the double, 12,9% and 24,1%.

However, an increase in Weibull modulus does not necessarily lead to a higher strength. *S1* and *S4* have the same total pore volume $P(\%)_{total}$, but the percentage of $P(\%)_{inter}$ and $P(\%)_{intra}$ were modified adjusting the solids loading and sintering temperature. Although *S1* has a higher reliability and $P(\%)_{intra}$ than *S4*, its mean strength is still lower (23,8 MPa and 43,4 MPa respectively). This behavior suggests that the strength of the individual struts is less important in the overall strength than the percentage of interlamellar porosity $P(\%)_{inter}$.

There is a fundamental difference between Weibull modulus and strength. While the latter positions a value in the strength distribution (i.e. $\bar{\sigma}$ is strength with a $P_f = 50\%$ and σ_0 at $P_f = 63\%$), the former determines the spread of the distribution and sometimes is refereed to as a shape parameter. Thus, the strength and reliability are independent properties that might be controlled separately [101].

The effect of higher Weibull modulus at lower wall thickness has been reported by Sabree et al. [102] in four-point-bending and Seeber et al. [103] in compression and three-point-bending. However, Cordell et al. [104] observed a different effect of pore size distribution depending on the deformation mechanism; the reliability increased in samples with smaller pore size for bending while for compression the reliability decreased with decreasing pore size.

Chapter 5

Gas permeability and pressure drop of unidirectional porous materials

Contents

The microstructural effects on permeability of porous ceramics have been extensively studied in different cellular structures. Innocentini et al. [33] compared the effect of pore volume and size in materials processed by replica and gel casting. Biasetto et al. [105] conducted a similar study on porous ceramics obtained by organic burn-out. However, although the tortuosity reduction has a beneficial effect on the gas flow, the literature on unidirectional porous materials, and particularly ice-templated, is scarce. The only exceptions are the work done by Fukushima et al. [5] and Pekor et al. [4]. These studies pointed out the importance of freezing conditions and additives as the main parameters to control in order to maximize the permeability. However, there is no reference on the effect of other fundamental parameters such as pore volume and morphology on permeability. This chapter intends to provide a deeper understanding on how to enhance permeability in ice templated materials by controlling pore volume, size, and morphology.

5.1 Microstructural characterization

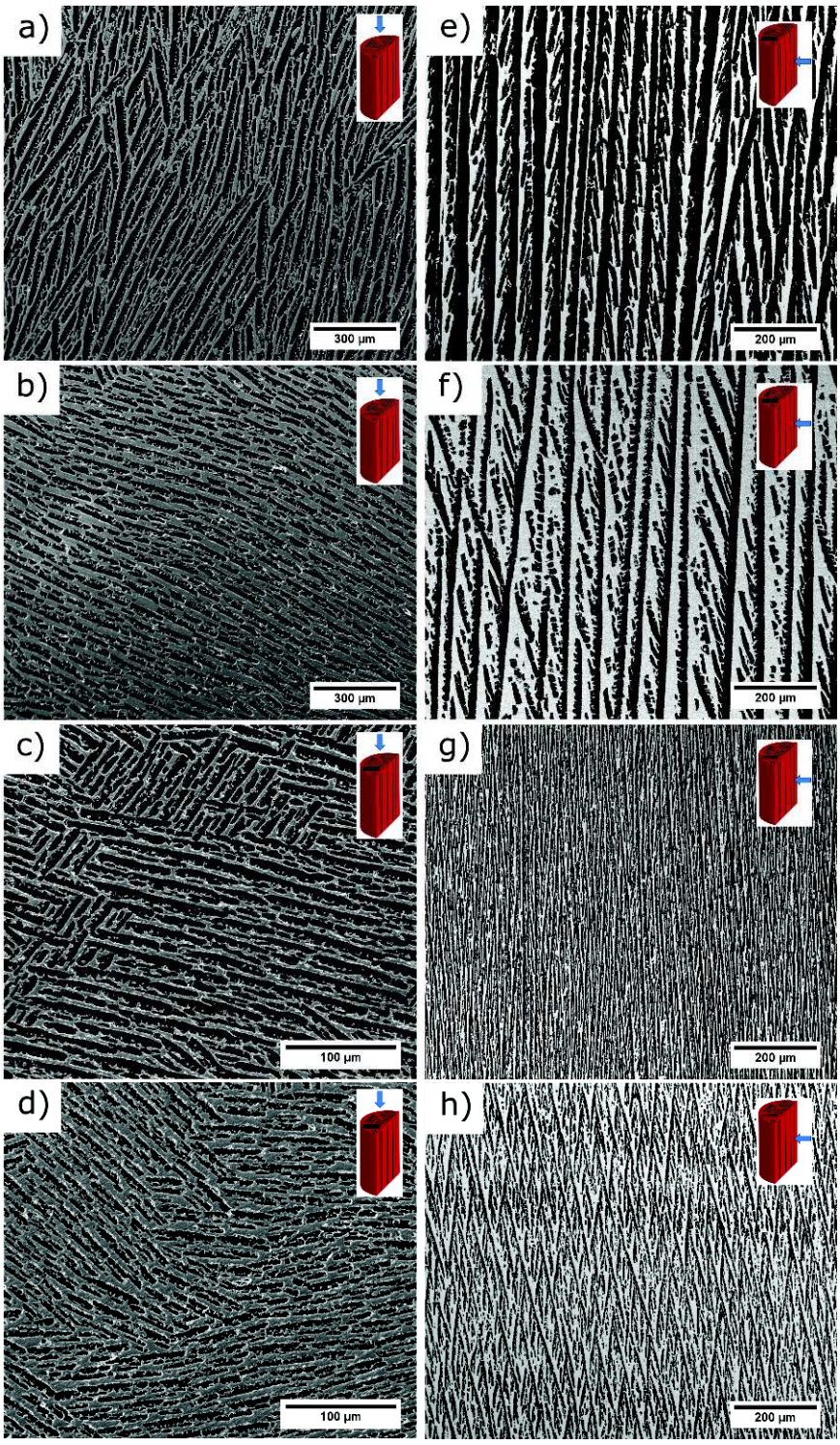

Figure 5.1: Ice templated microstructures of samples shown in Table 5.1. Sections perpendicular to the freezing direction: a) P1 b) P4 c) P5 d) P8 and parallel e) P1 f) P4 g) P5 h) P8

Fig. 5.1(a-d) shows cross sections perpendicular to the solidification front for the samples P1, P4, P5, and P8 in Table 5.1. All of them exhibit a lamellar pore morphology characteristic of ice templated samples with water used as a solvent. The total pore volume and pore size were almost independently controlled by the initial solids loading and pore size respectively. Fig. 5.1-a and 5.1-b show the microstructures obtained in two samples frozen at identical cooling rate (2 °C/min) but different solids loading (50 wt.% and 65 wt.%). As described in Chapter 3, the modification of the solids loading causes a variation on the relative density of the samples, and the total pore volume changes accordingly. Increasing the solids loading from 50% to 65% causes a decrease in total pore volume from 72% to 54%. The same effect has also been observed at higher freezing rate, Fig. 5.1-c and Fig. 5.1-d, but the pore size obtained was smaller. For example, when freezing temperature increased from 2 °C/min to 25 °C/min, mean pore size (d_p) decreased from 20,0 $\pm$ 8,5 μm to 4,7 $\pm$ 1,9.

Table 5.1 also highlights the effect of solids loading on pore size. Specimens ice-templated with 50 wt.% solids loading exhibit a pore size remarkably larger (20,0 $\pm$ 8,5 μm) than those ice-templated with 65 wt.% (13,7 $\pm$ 4,8 μm). Although the pore size reduction caused by the solids loading holds a second order of importance compared with the cooling rate, it is important to consider it because certainly will affect the permeability.

Sample	Solids loading(wt.%)	Cooling rate(°C/min)	Porosity(%)	Mean $d_{pHg}(\mu m)$	Mean $d_{pIA}(\mu m)$	k_1 (m^2)	R^2
P1	50%	2	72%	19,1	20,0 $\pm$ 8,5	1.39×10^{-11}	0,999
P2	55%	2	67%	17,5	17,7 $\pm$ 6,7	9.44×10^{-12}	0,999
P3	60%	2	60%	14,2	13,9 $\pm$ 5,5	5.95×10^{-12}	0,999
P4	65%	2	54%	8,3	13,7 $\pm$ 4,8	2.17×10^{-12}	0,998
P5	50%	25	72%	5,4	4,7 $\pm$ 1,9	1.08×10^{-13}	0,999
P6	55%	25	68%	4,3	4,3 $\pm$ 1,7	7.99×10^{-14}	0,999
P7	60%	25	60%	3,9	4,1 $\pm$ 1,7	4.27×10^{-14}	0,999
P8	65%	25	55%	2,9	3,1 $\pm$ 1,2	2.36×10^{-14}	0,999

Table 5.1: Summary of main physical characterization of ice templated samples. d_{pHg} and d_{pIA} refer to the mean pore size measured by mercury porosimetry and image analysis respectively. R^2 correspond to the correlation coefficient of the lines shown in Fig. 5.3.

Fig. 5.1(e-h) shows the microstructures of the same ice templated samples parallel to the solidification front. In all cases, pores are continuous with an almost constant cross-section, independently of the solids loading (Fig. 5.1-e and 5.1-f) and cooling rate (Fig. 5.1-g and 5.1-h). All the samples exhibited the characteristic dendritic growth of ice-templated materials. These secondary arms are originated from the mismatch between imposed and preferred crystal growth [6]. During the steady-state regime, the ice-crystals grow slightly tilted respect to the direction of the imposed thermal gradient, Fig. 5.2. This tilting exposes one side of the crystal to the macroscopic temperature gradient and induces the dendritic growth. This effect explains why only one side of the main crystals have sencondary arms and the other one is flat. The dendritic growth entrap the ceramic particles between themselves creating a second type of porosity, usually

smaller, after removing the ice. The presence of these dendrites is independent of the freezing rate and the solids loading of the initial slurry within the investigated range.

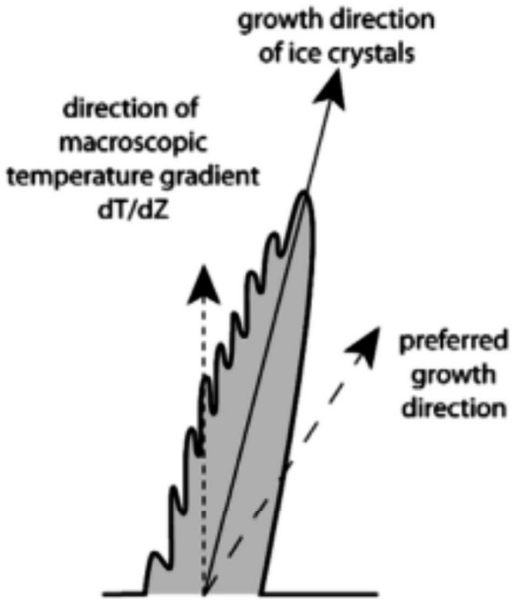

Figure 5.2: Representation of the dendritic growth of ice crystals [6].

5.2 Pressure drop and permeability

Fig. 5.3 shows the variation of pressure drop (ΔP) with air velocity (ν_s) for the specimens P1-P8 decribed in Table 5.1. Increasing ν_s leads to increase ΔP. However, the different slopes exhibited by all groups highlight the importance of pore volume and pore size on the gas flow resistance and hence pressure drop.

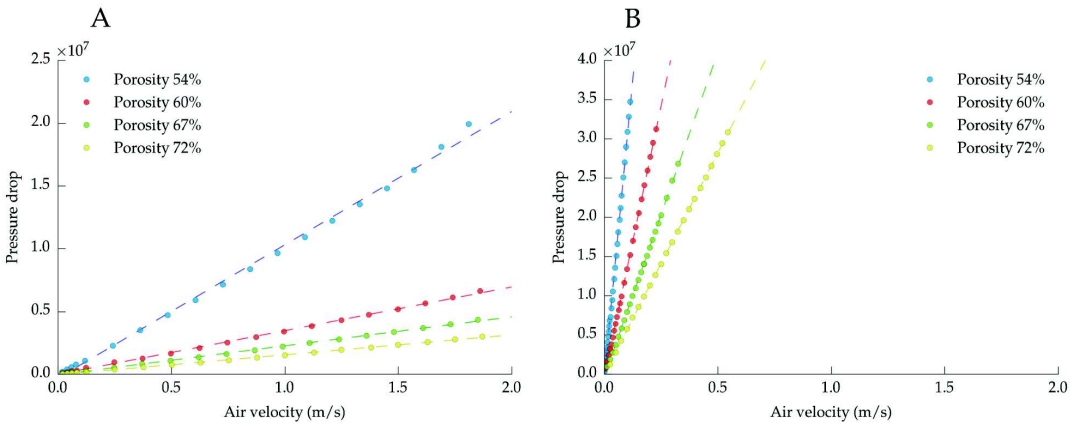

Figure 5.3: Pressure drop measurement versus air velocity for different porosities for ice templated samples frozen at A) 2 °C/min B) 25 °C/min.

Interestingly, the eight sets of experiments followed a linear relationship between ΔP and ν_s. This behavior can be explained based on the complex nature of the Forchheimer equation. The first term ($\mu\nu_s/k_1$) in Eq. 2.5 considers the viscous energy losses caused by the friction between fluid layers, and the second term ($\rho\nu_s^2/k_2$) accounts for the inertial effects created by turbulances and variations in the direction and acceleration of the fluid [106]. The excellent linear correlation coefficient (R^2=0,998) found in all conditions makes us think that all the tests were performed in viscous flow regime and thus, the determination of permeability is only subjected to the reduced form of Eq. 2.5 i.e. Darcy's law Eq. 5.1:

$$\frac{\Delta P}{L} = \frac{{P_i}^2 - {P_o}^2}{2P_oL} = \frac{\mu}{k_1}\nu_s \tag{5.1}$$

To assess this hypothesis we evaluate the fraction of the flow that corresponds to viscous flow ($\Delta P_{Darcian}$) based on the Forchheimer number (F_0) as follows [13], where the symbols are the same as used in Eq. 2.5:

$$F_0 = (\frac{\rho\nu_s}{\mu})(\frac{k_1}{k_2}) \tag{5.2}$$

$$\frac{\Delta P_{Darcian}}{\Delta P_{Total}} = \frac{1}{1+F_0} \tag{5.3}$$

The effects of pore size and pore volume on $\Delta P_{Darcian}$ are shown in Fig. 5.4. In all the samples the percentage of viscous flow is above 85% and therefore the contribution of turbulent flow on the total pressure drop is negligible. This observation supports the initial hypothesis that the permeability of ice-templated materials, within the studied conditions, can be characterized just using Eq. 5.1. Nevertheless, careful considerations should be made if k_1 is intended to be applied in systems with higher air flow. In these conditions the inertial effects and turbulences become important and both constants (k_1 and k_2) are required to describe the parabolic behavior [22].

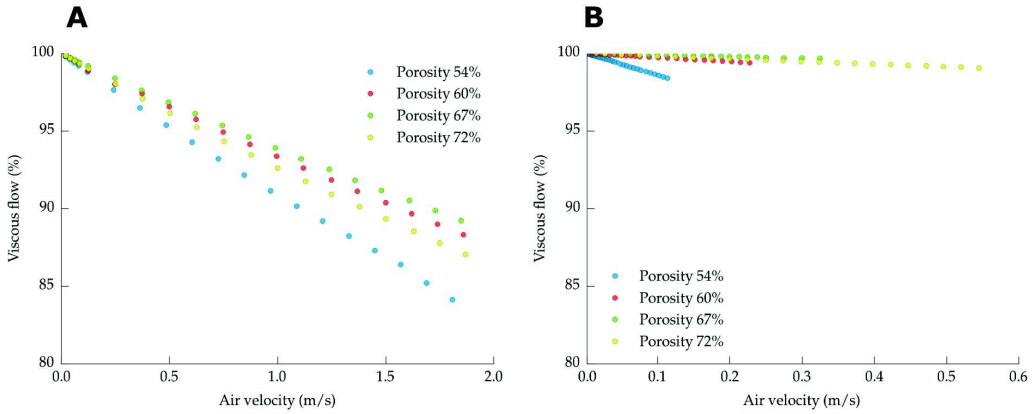

Figure 5.4: Variation of percentage of viscous flow versus air velocity for different porosities in ice templated samples frozen at A) 2 °C/min B) 25 °C/min.

Fig. 5.5 and Table 5.1 show the effect of initial solids loading and cooling rate on permeability. Decreasing the solids loading causes an increase in k_1 that can be correlated with an increase in total pore volume. Moreover, it has to be considered the additional effect of larger pore sizes when the solids loading increases. On the other hand, the specimens frozen faster are remarkably less permeable. The main explanation for this behavior relies on the important reduction in pore size observed at these freezing conditions. The fact that the permeability drop is around two orders of magnitude in samples with the same total pore volume, emphasizes the great importance of pore size to maximize the fluid flow without increasing the pressure drop in an exaggerated manner.

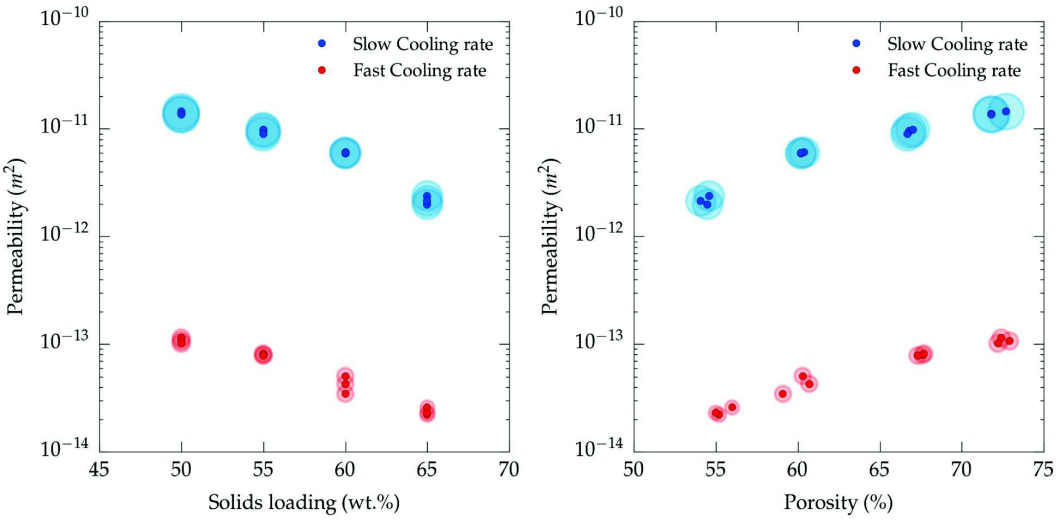

Figure 5.5: Effect of solids loading and freezing rate on permeability. Experimental and morphological parameters are specified in Table 5.1. Marker size is proportional to pore size.

The values obtained in this work are in agreement with those found in the literature

for ice templated samples with similar microstructure. Pekor et al. [4] reported a permeability of 1.0×10^{-11} m^2 for ice templated alumina with 70% porosity and pore size around 17 μm. Fukushima et al. [5] obtained a slightly higher k_1 (2.27×10^{-11} m^2) for a SiC prepared by gelation freezing method but with a remarkably higher pore volume and pore size (86% and 34 μm).

As Fig. 5.6 shows, the permeability exhibited by ice templated materials falls in the wide range exhibited by gelcasted foams and much lower than those typically exhibited by reticulated foams. However, the total pore volume, and more importantly the pore size of this type of cellular materials, is much higher compared with those obtained by ice templating. For example, Innocentini et al. [33] reported a k_1 of 1.5×10^{-10} m^2 for a a porous alumina processed by replica method with 70% porosity and 200 μm pore size and a permeability of 5×10^{-11} m^2 for a porous alumina prepared by gelcasting with the same pore volume and 125 μm pore size .

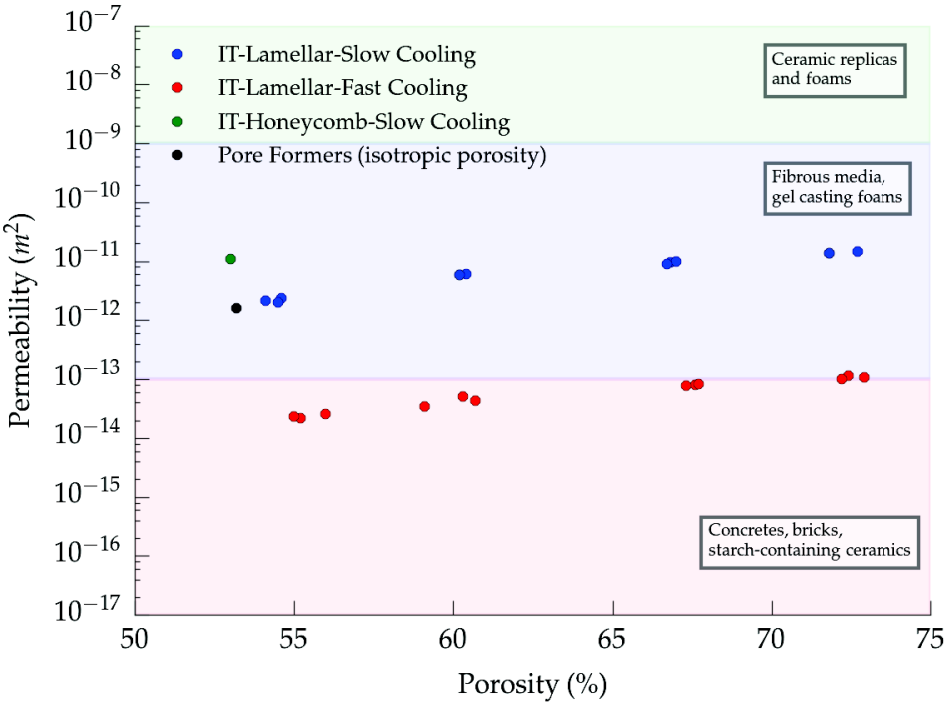

Figure 5.6: Comparison of the permeabilities that can be achieved by the most common processing techniques [13].

Two additional groups of specimens with different pore architectures were prepared to evaluate the effect of pore directionality and morphology on permeability. The first group consists of samples with isotropic porosity processed by organic pore formers, and the second group comprises ice-templated samples with zirconium acetate (ZRA) added to the original slurry. As it was explained in Chapter 3, the addition of ZRA turns the pore morphology into a honeycomb-like structure with smooth surfaces. This structure

posses a larger mean pore size than the typical lamellar ice-templated morphology at similar total pore volume, (Fig. 5.7). This variation in pore size distribution causes an increase in permeability of almost one order of magnitude, as shown in Fig. 5.6. In contrast, the specimens processed by pore formers have a similar permeability as the ice-templated specimens with lamellar morphology and therefore an apparent no effect of pore tortuosity, Fig. 5.6. However, although the mean pore size is similar in both samples, the distribution tend to be more spread in materials processed by pore formers. The presence of these big pore clusters might facilitate the air flow through the samples and consequently mask the effect of directionality. Although the presence of larger isolated pores certainly increases the permeability, they can become stress concentrators and affect the mechanical integrity of the system.

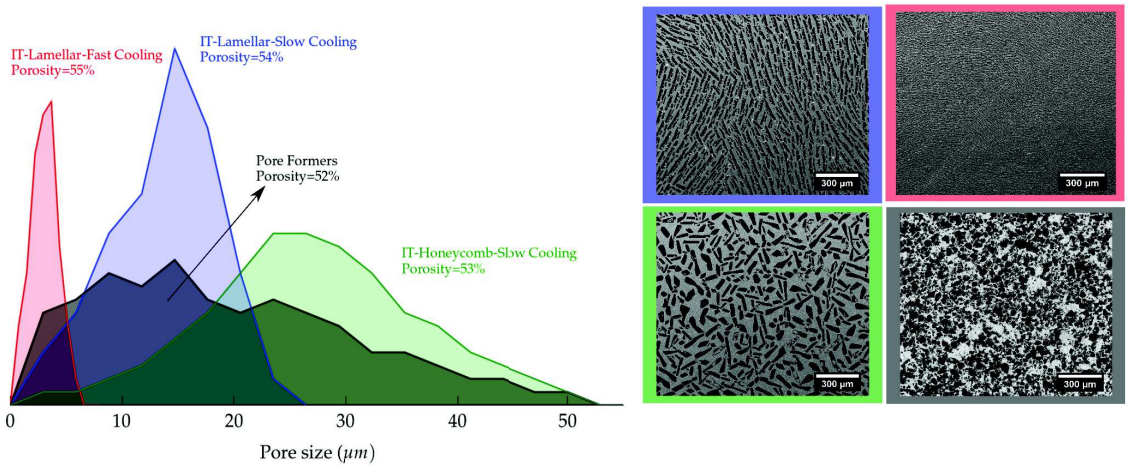

Figure 5.7: Pore size distribution of different ice-templated structures compared with sacrificial method (pore formers).

Most of the important industrial applications involving porous materials are subjected to a trade-off between permeability and strength [107]. Since both properties are inversely related to total pore volume, other strategies different than increasing/decreasing this parameter are necessary to improve both properties simultaneously. Fig. 5.8 shows the effect of microstructural variations in permeability and strength at constant porosity (around 54%). The ice-templated specimens with smaller pore size have the highest strength although they also exhibited the lowest permeability, so this strategy does not seem to be the most optimal to follow. Alternatively, ice-templated samples frozen at slow cooling rate have a similar permeability compared with the samples prepared by pore formers. However, as it was previously explained in section 4.3.1, the increase in permeability achieved by isotropic samples by broadening the pore size distribution has a detrimental impact on strength. Nevertheless, the best compromise between strength and permeability was obtained in ice-templated samples with honeycomb morphology. Although the larger pore size certainly reduces the strength, it is not as important as

the improvement in permeability, and even reached permeability values comparable to ice-templated samples with lamellar morphology and 72% pore volume.

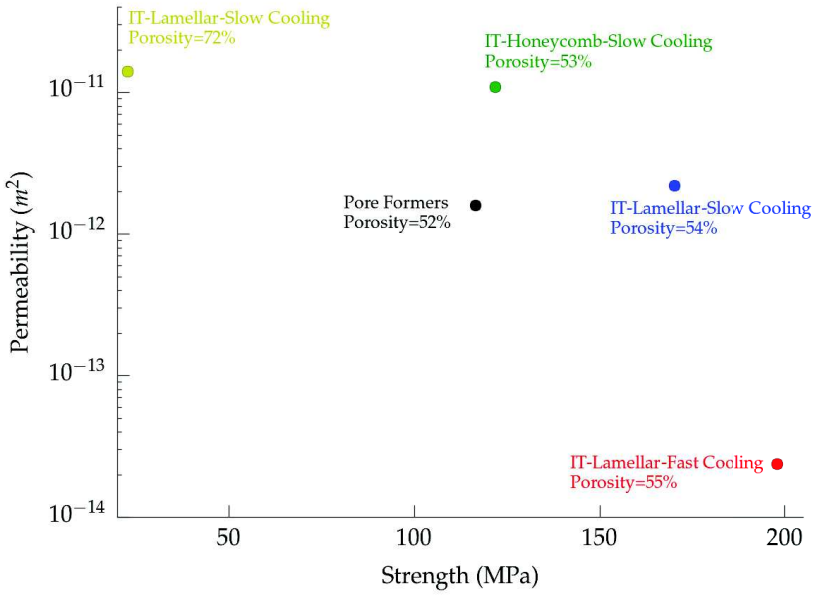

Figure 5.8: Compressive strength and permeability of ice-templated (IT) and sacrificial (Pore formers) samples processed in this work. Pore size distributions are shown in Fig. 5.7

5.3 Prediction by models

Most of the models used to predict the permeability constants (k_1 and k_2) are extracted from correlations originally developed for granular beds and are dependent on the volumetric void fraction (ϵ), and the equivalent particle size (d_p). The most common expression was developed by Ergun [108] (Eq. 5.4) and it has been extensively applied to all types of porous media [109] [28] [26].

$$k_1 = \frac{\epsilon^3 {d_p}^2}{150(1-\epsilon)^2} \tag{5.4}$$

However, this approach exhibits some complications to be used in cellular materials due to the difficulties to extract the characteristic parameter that could replace the particle size (d_p). One solution consists on replacing d_p by an equivalent pore size (d_c) [27] and then, k_1 and k_2 can be rewritten as:

$$k_1 = \frac{2,25}{150}\epsilon {d_c}^2 \tag{5.5}$$

The experimental values of k_1 for ice-templated samples frozen at 2°C/min and 25°C/min were compared with those predicted by Eq. 5.5. Since the evaluation of permeability by

Ergun's equations is highly sensitive to the equivalent pore size (d_c), the assessment of the model was conducted with the pore sizes measured by image analysis and mercury porosimetry. As Fig. 5.9-Left shows, all the experimental points diverge constantly with the prediction of the Ergun model (dashed line) independently of the technique used to characterize the pore size. The only exceptions are the specimens frozen at slow cooling rate and lower permeability which seemingly exhibited a better fitting when the pore size was obtained by image analysis. However, this result clearly deviates from the tendency displayed by the other samples and can be attributed to the increasing presence closed pores found at high solids loading (P4 in Table 5.1).

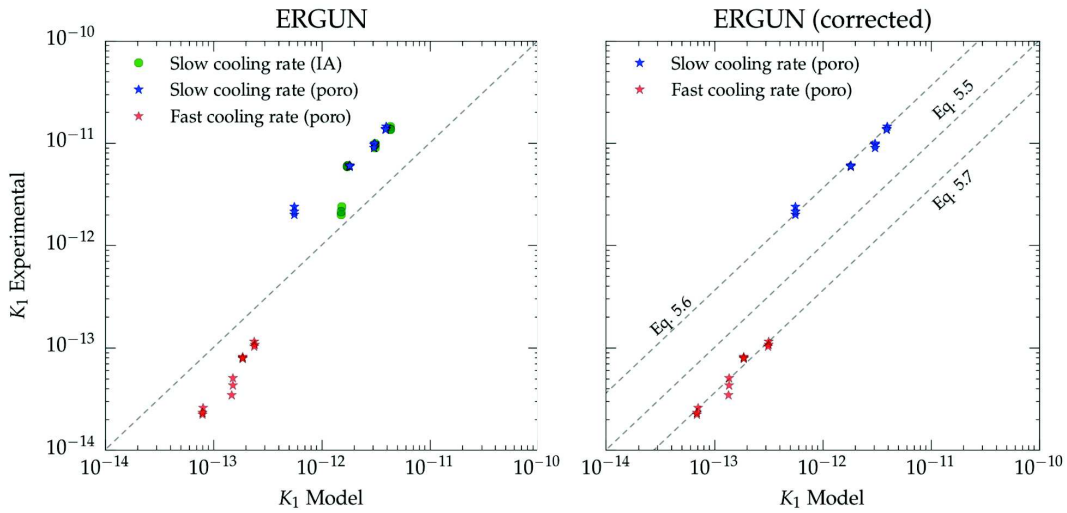

Figure 5.9: Comparison between the experimental permeability data and the values predicted by Ergun Equation (left) and Ergun modified (right). Two different methods were used to evaluated the pore size, image analysis (IA) and mercury porosimetry (poro)

The main factor that explains the deviation between experimental and calculated values of k_1 relies on the semi-empirical nature of Ergun expression. The value of 150 in Eq. 5.5 was determined originally on different experiments on highly tortuous media and thus, it might not be valid for radically different porous structures i.e. unidirectional porous materials. Nevertheless, since it is an expression broadly used and for the sake of comparison, we corrected the original Ergun equation (Eq. 5.5) to represent the experimental data obtained in this work (Fig. 5.9-Right). Eq. 5.6 describes the permeability of samples frozen at 2°C/min and Eq. 5.7 for samples frozen at 25°C/min.

$$k_1 = \frac{2,25}{42}\epsilon {d_c}^2 \tag{5.6}$$

$$k_1 = \frac{2,25}{407}\epsilon {d_c}^2 \tag{5.7}$$

The microstructure of ice-templated materials resemble more to a capillary system where pores are aligned parallel to the gas flow than a porous granular media. The maximum permeability in an ideal capillary model is described by Eq. 5.8 [29]

$$K_{capillary} = \frac{\phi d_p^2}{\tau 32} \tag{5.8}$$

where ϕ, d_p, and τ are porosity, pore size, and tortuosity respectively.

The capillary permeability ($K_{capillary}$) of ice templated samples was calculated based on the measurements of porosity and pore size obtained by mercury porosimetry shown in Table 5.1 and using Eq. 5.8. Fig. 5.10 shows the experimental values of k_1 compared with those predicted by the model. The permeability of ice templated samples frozen at slow cooling rate (2 °C/min) is close to the maximum obtained when $\tau = 1$. This result indicates that the porosity of these samples is almost continuous and the capillary model is thus a good permeability descriptor. However, the permeability of ice-templated materials is not always predicted by the ideal case of Eq. 5.8 and τ=1. For example, the best fit of specimens frozen faster (25 °C/min) is exhibited around $\tau = 5$. Usually, in isotropic porous materials, tortuosity tends to decrease when pore volume increases [110]. Unlike in isotropic samples, tortuosity of ice-templated materials remains constant in a broad porosity range (50%-70%) but is instead controlled by pore size.

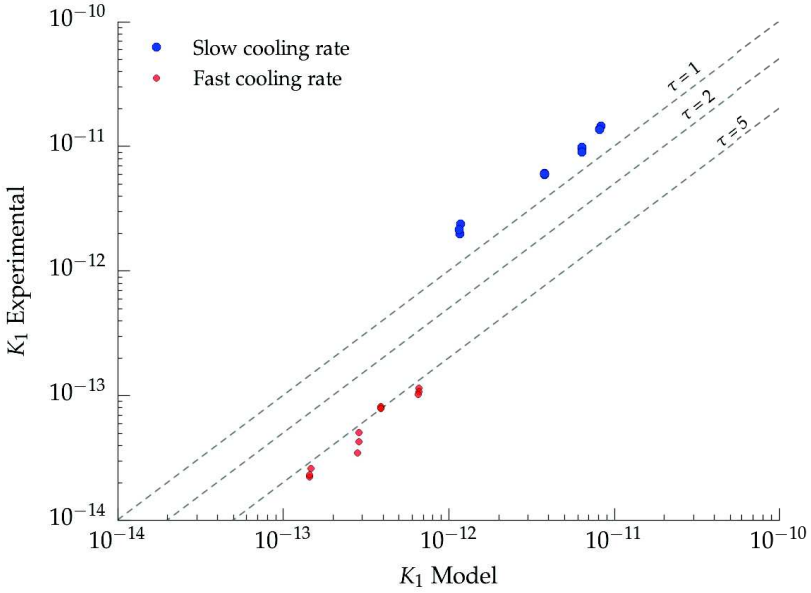

Figure 5.10: Comparison between the experimental permeability data and the values predicted by the capillary model

Chapter 6

Fabrication of ice-templated tubes: Microstructure, strength, and permeability

Contents

Typically, tubular porous substrates are prepared by: extrusion [111] [112], slip casting [113], centrifugal casting [114], or isostatic pressing [115]. However, these techniques rely on increasing the total pore volume and pore size to achieve the required permeability, at expenses of decreasing the mechanical properties. Therefore, it is necessary to explore other strategies such as an optimized pore shape or reduced tortuosity to improve permeability and strength simultaneously.

As we showed in previous sections, an architectured porosity, like the one created in ice-templating, is a feasible strategy to enhance both properties simultaneously. Nonetheless, to produce tubes with unidirectional radial porosity by ice-templating seems more an engineering problem to solve. The literature on ice-templated tubes is still scarce. Moon et al. [116] used an external metallic mold with a central PTFE rod to induce the thermal gradient required to aligned the porosity. They studied the effect of solids loading and freezing temperature on the microstructure and the feasibility to deposit an external dense layer. Liu et al. [65] used a similar set-up to evaluate the impact of

solids loading, pore size, and particle size on compressive strength, and nitrogen and water flux. However, the difficulties to demold the tubes after the entire solidification is still one of the main drawbacks of this set-up that limits a further industrial application. Moreover, a more detailed mechanical characterization is still missing in this type of porous materials.

In this chapter, we propose a novel method to produce ice-templated tubes based on a rotational freezing. We investigate the impact of pore volume, size, and tube thickness on mechanical properties using an o-ring test, four-point bending, and crush test. Furthermore, we studied the effect of the same morphological parameters on permeability to assess the applicability of these materials as a membrane supports.

6.1 Microstructure control

Fig. 6.1 schematically depicts the process that occurs during the rotational freezing. The tube rotation spreads the slurry across the inner surface of the mold. Then, the freezing oil is pumped in the container and the slurry in contact with the mold solidifies almost instantly. The freezing rate at this initial stage is very high due to the high heat transfer between the copper mold and the slurry. Afterwards, the velocity of the solidification front undergoes an abrupt decrease, until it reaches a steady state with an approximate constant value. As a consequence of this difference in the freezing kinetics, ice-templated tubes exhibited two clearly differentiated pore morphologies, random and lamellar porosity, similarly as in ice-templated monoliths [117]. The external layer with random porosity is generated when the velocity of the solidification front is too high for the ice crystals grow with a preferential orientation and thus they are not able to rearrange the ceramic particles (Fig. 6.2-a). Alternatively, when the steady state is finally reached, the ice crystal grow continuously following the thermal gradient (i.e. in this case the radial direction) and the pore morphology becomes lamellar (Fig. 6.2-b). The constant rotation of the system maintains the remaining liquid in contact with the frozen part and provides the slurry required to continue with the ice-templating process until the entire solidification of the tube.

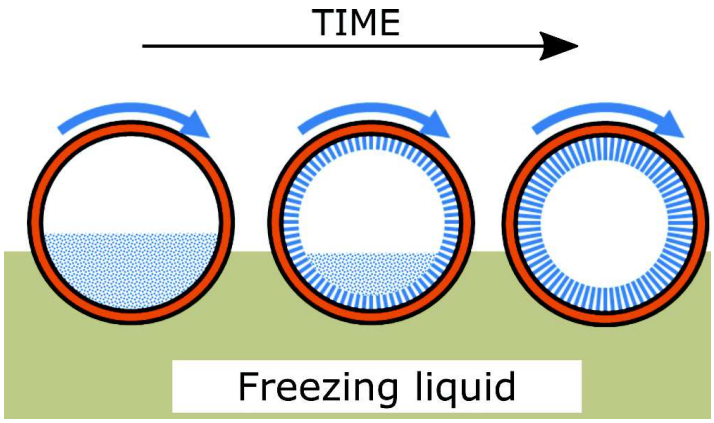

Figure 6.1: Schematic of the rotational freezing process.

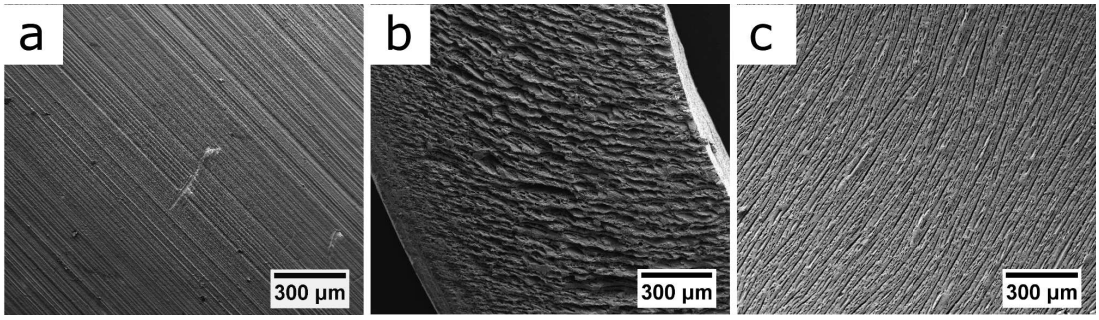

Figure 6.2: SEM micrographs of different locations of an ice-templated tube with a 65 wt.% solids loading, frozen at -30°C, and 20 ml. A) Top view of the external layer B) Cross section of the tube and C) Top view of the inner surface.

To a first approximation, pore volume and size control between ice-templated tubes and monoliths are identical. Total pore volume is still tailored by solids loading, and pore size is adjusted by cooling rate, Fig. 6.3. Table 6.1 reports these microstructural features and the experimental conditions used.

Solids loading(wt.%)	Porosity(%)	Freezing Temperature (°C)	Mean d_p (μm)
65	49,1	-80	3,3
55	66,3	-80	6,8
50	69,6	-80	7,3
65	45,0	-30	6,2
55	64,1	-30	10,6
50	68,4	-30	14,6

Table 6.1: Summary of the effect of solids loading and freezing temperature on porosity and mean pore size (d_p). Porosity and d_p obtained by mercury intrusion porosimetry.

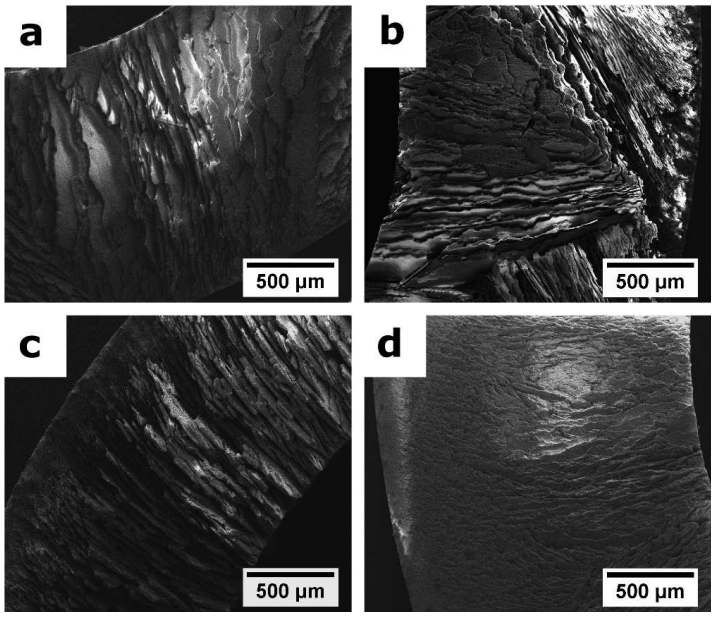

Figure 6.3: Detail of the radial porosity of ice-templated tubes sections reported in Table 6.1. a) 50 wt.% solids loading and freezing temperature -30°C, b) 50 wt.% solids loading and freezing temperature -80°C, c) 65 wt.% solids loading and freezing temperature -30°C, and d) 65 wt.% solids loading and freezing temperature -80°C. In all cases the volume of slurry used was 20ml.

The dashed line in Fig. 6.4 represents the relationship between solids loading and porosity obtained previously in ice-templated monoliths (Fig. 4.9). The perfect match between both indicates that the total pore volume is dictated exclusively by the solids loading of the initial slurry, independently of the mold used. Since the pore volume measurements were taken in different locations of the tube, it also indicates that the pore volume is homogeneously distributed through whole tube.

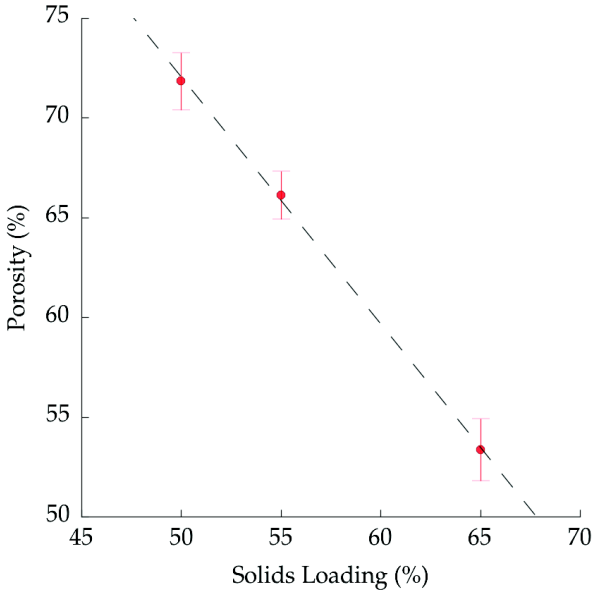

Figure 6.4: Variation of porosity as a function of the solids loading of the slurry. Dashed line represents the the relationship between solids loading and porosity obtained in a previous work for ice-templated YSZ monoliths (cite mech. props. article).

Fig. 6.5 shows a top view of three ice-templated tubes with a different amount of slurry initially poured into the mold (20, 18, and 16 ml). A decrease in the volume of slurry causes a reduction on the overall thickness of the tube because there is less material to be ice-templated. The thickness of the tubes after sintering were 2.0, 1.8, and 1.6 mm for a volume of slurry of 20, 18, and 16 ml.

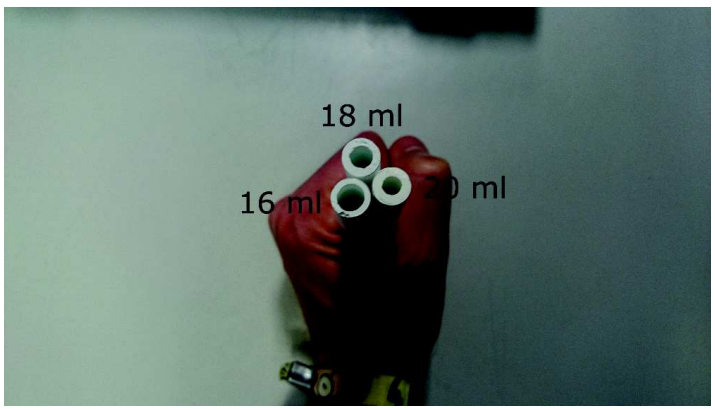

Figure 6.5: Detail of the thickness variation by changing the initial amount of slurry.

6.2 Mechanical properties

Tubular materials in real applications may be subjected to a complex stress field that do not resemble the ideal case obtained in a compressive test. Therefore, extrapolations

from simple crush testing of monoliths should be complimented by a more exhaustive mechanical characterization of the tubes. Here, we investigate the strength of tubular ice-templated materials in a biaxial stress state, o-ring test and four-point bending, and by axial compression.

6.2.1 O-Ring test

Fig. 6.6 shows two representative load-displacement curves for samples frozen at -80°C and -30°C. In both cases, the fracture behavior is described by an initial linear stage followed by two consecutive load drops. When the ring is subjected to a diametrical compression i.e. like in the O-ring test, the maximum tensile stresses (σ_{max}) are located on the intersection between the inner diameter and the loading plane [118] and can be determined by Eq. 6.1.

$$\sigma_{max} = 1,8\frac{Pr_a}{ht}(1 + \frac{t}{3r_a}) \tag{6.1}$$

where *P* is the maximum load, *t* the tube thickness, *h* the width of the ring, and r_a the average radius $(r_{ext} - r_{int})/2$

This load corresponds to the first peak in the load-displacement curve and it was used to describe the strength of the rings. The second peak corresponds to the fracture of the two remaining "*half rings*", originated by the tension developed on the transverse diameter of the outer periphery. Both types of cracks are shown in Fig. 6.6.

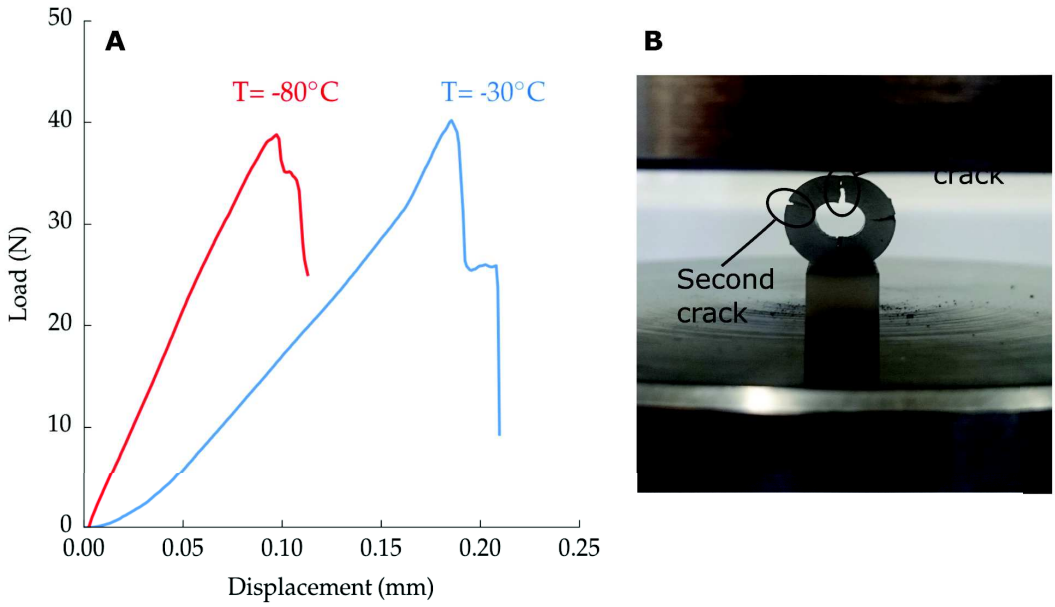

Figure 6.6: A) Representative load-displacement curves of two rings obtained from tubes with a 65% solids loading and frozen at -80°C (red) and -30°C (blue). B) Detail of the characteristic fracture in a O-ring test with the two types of cracks highlighted.

Fig. 6.7 shows the effect of pore volume on strength for samples frozen at -80°C and -30°C. As expected, rings with higher pore volume exhibited a lower strength. Moreover, samples frozen at a lower temperature (-80°C) have a smaller pore size and therefore should exhibited an increase in strength as shown in Chapter 4 [74]. However, the large scattering of the strength data makes it difficult to conclude whether this effect is seen here. There are two contributions for the existence of this spread. First, the probabilistic nature of the strength in ceramics [92], and second (and more likely) the eccentricity of the inner diameter. One of the main drawbacks of the tubes obtained by rotational freezing is the lack of accuracy to control the thickness of the tube, and the subsequent presence of geometrical defects such as eccentricity (Fig. 6.8-A) or warping during sintering (Fig. 6.8-B). As it was discussed by Kwok et al. [119], these types of geometrical imperfections induce an asymmetry in the stress field that have a deleterious effect on the flexural strength, and in this case hide the pore size effect.

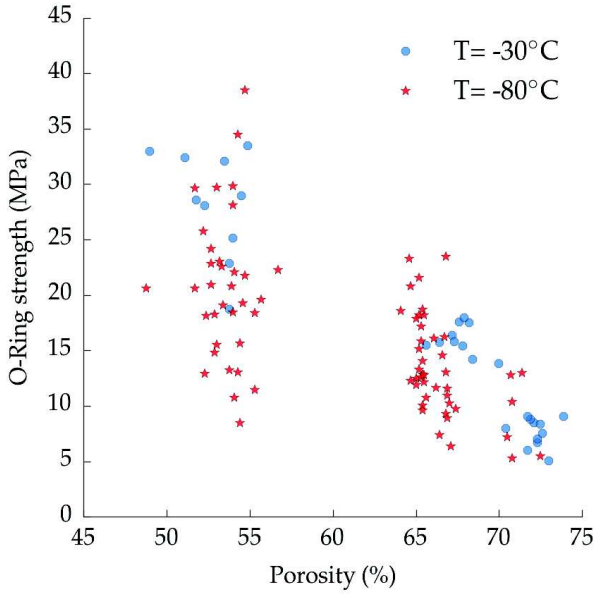

Figure 6.7: Effect of porosity and freezing temperature on radial crushing strength obtained by O-ring test.

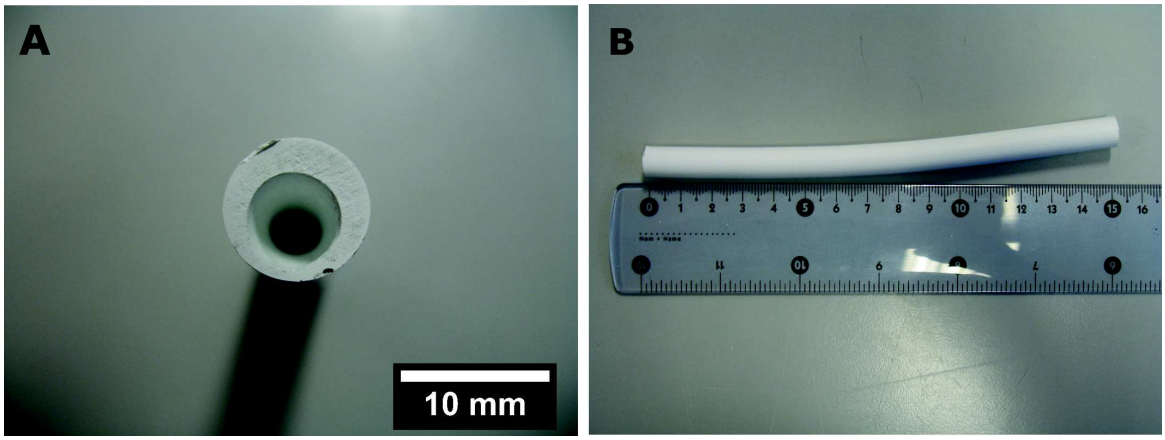

Figure 6.8: Details of the geometrical defects found in tubes made by rotational freezing. A) eccentricity, B) warping.

6.2.2 Four-point bending

Tubular components in real industrial applications are subjected to bending moments that affect their mechanical stability. Therefore, flexural strength characterization is a required step before any further application. Recently, the use of four-point bending tests have been extended to semi-cylindrical tubes [120]. Although the quantification of the stress field in this sample shape is more complex than in regular bars, in both cases the maximum stress (σ_{max}) can be well approximated by the axial stress at the middle point (M) between the two inner supports [53]. The test was considered invalid when the crack propagated outside the supports, usually on the contact point between

the sample and the external support. When the crack pattern resulted in a succesful test, the maximum stress was calculated by:

$$\sigma_{max} = \frac{Pay_c}{I} \tag{6.2}$$

where *P* is the maximum load, *a* is the distance between the load and the support, y_c is the distance between *M* and the centroid of the specimen cross section along the y-axis, and *I* is the second moment of inertia of the cross section. For a semi-circular annulus, y_c and *I* are expressed as:

$$I = \frac{\pi}{8}(R^4 - {R_i}^4) - \frac{8}{9\pi}\frac{(R^3 - {R_i}^3)^2}{R^2 - {R_i}^2} \tag{6.3}$$

and

$$y_c = R - \frac{4}{3\pi}\frac{R^3 - {R_i}^3}{R^2 - {R_i}^2} \tag{6.4}$$

where *R* and R_{int} are the external and internal radius respectively.

Here, we modified the solids loading, freezing temperature, and volume of the slurry initially poured into the mold to obtain ice-templated tubes with different pore volume, pore size, and thickness respectively. Fig. 6.9 shows the effect of each parameter on the flexural strength.

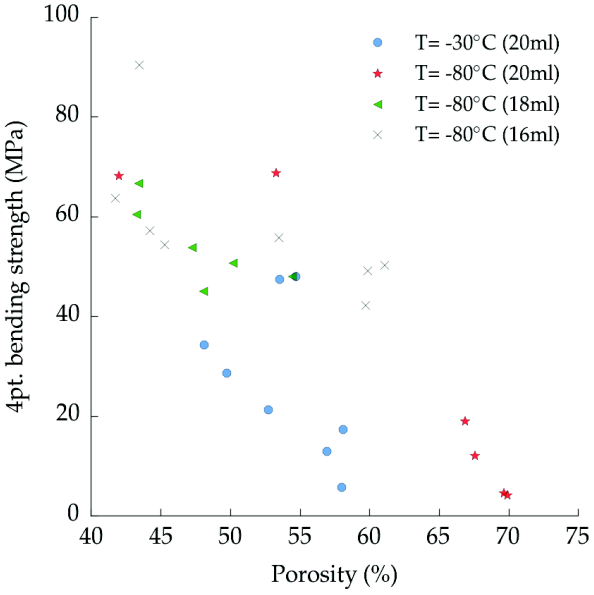

Figure 6.9: Effect of porosity, freezing temperature, and volume of slurry on flexural strength obtained by four-point bending.

In all conditions, when the solids loading increases the total pore volume of the sample decreases, causing an increase in strength. Unlike in the diametrical compression, in four-point bending we did observe an increase on strength with pore size. We attributed this effect to the increasing amount of ceramic struts between the adjacent walls observed at lower freezing temperatures [37]. When the half ice-templated tube is bent, the external midpoint is subjected to tensile forces. Since the porosity is perpendicular to this tensile forces, the strength of the tube is determined by the resistance of the structure to opening the pores which is resisted by interlocked walls.

In contrast, it became more difficult to discern the effect of tube thickness on flexural strength. Although, the mean thickness of the tube can be controlled by the amount of slurry, rotational freezing does not provide a perfect control of thickness, and large mismatches (<1mm) are found in the same tube (Fig. 6.10). These discrepancies invalidate any conclusion with the intention to relate thickness with strength.

Figure 6.10: Detail of the thickness inhomogeneity in a four-point bending sample.

6.2.3 Compression test

Little compressive strength data of tube sections have been reported. The parameters investigated here were the same as in the four-point bending test, and the results are reported in Fig. 6.11. When the tube is loaded in the axial direction, pores are perpendicular to the load and ceramic bridges between the walls prevent the buckling of the structure. Similarly to the four-point bending, specimens frozen at lower temperature exhibited a higher strength due to the higher number of connections between walls. Again, the variability in the tube thickness for a given amount of slurry prevents to discern the effect on compressive strength, and consequently the results are not conclusive.

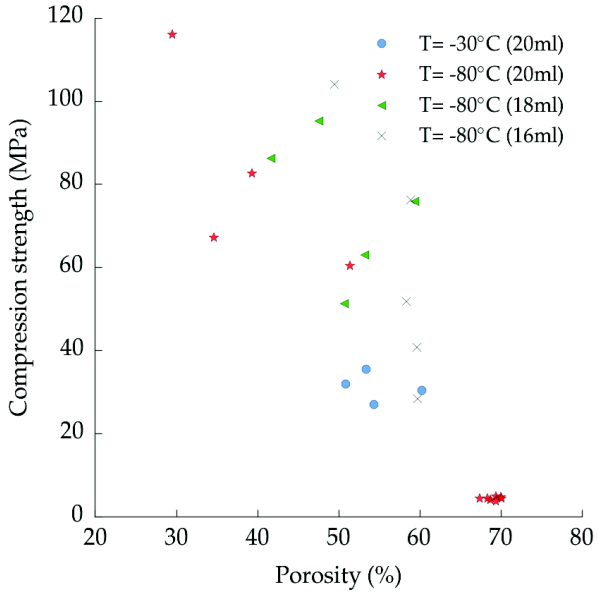

Figure 6.11: Effect of porosity, freezing temperature, and volume of slurry on axial strength obtained by compression test.

6.3 Permeability

Tubes obtained with different solids loading, freezing temperature, and volume of slurry poured into the mold were tested to evaluate the independent impact of pore volume, pore size, and tube thickness respectively on permeability, Fig. 6.12. In all cases pressure drop (ΔP) exhibits a linear dependence with air velocity (ν_s) and, thus, permeability can be calculated from their slopes according to the Darcy's law (Eq. 5.1) instead of the Forchheimer equation [22].

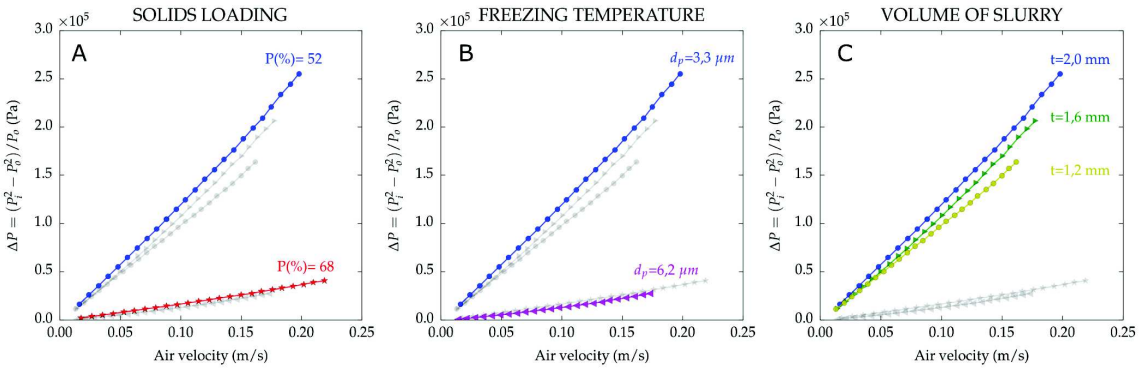

Figure 6.12: Effect of experimental conditions on pressure drop. A) 65% and 50% solids loading, B) -80°C and -30°C, and C) 20, 18, and 16ml poured initially on the mold. Values specified in Table 6.2.

Permeability values (k_1), experimental conditions, and the most relevant pore descrip-

tors are specified in Table 6.2. When pore volume increases due to the solids loading reduction, there is less resistance to the airflow and permeability increases accordingly, (Fig. 6.12-A). Also, a higher pore volume leads to increase the mean pore size, enhancing even further this effect. When the tubes are frozen using a constant solids loading and lower temperature, the total pore volume remains invariant and the pore size reduces, affecting the permeability. Fig. 6.12-B show how the specimen frozen at -80°C exhibits a smaller pore size (3,3 μm) and lower permeability (2,80$\times 10^{-14}$ m^2). Interestingly, the sample frozen at higher temperature (-30°C), pore size of 6,2 μm, and 52% porosity in Fig. 6.12-B has a comparable permeability (and hence pressure drop) to the sample frozen at -80°C, pore size 7,3 μm, and porosity 68% in Fig. 6.12-A. This result emphasizes the importance of pore size over pore volume as the critical parameter to tailor permeability. This observation is in agreement with the Hagen-Poiseuille equation that predicts a gas flow dependence (i.e. in a viscous flow) proportional to the pore volume compared with the square exhibited by pore size [29]. Finally, permeability can also be controlled by the volume of slurry initially poured into the mold, Fig. 6.12-C. When the volume of slurry decreases, the thickness of the tube decreases as well and the tube becomes more permeable due to the reduction of the pathway to evacuate the air.

Solids loading(wt.%)	Porosity(%)	Freezing Temperature (°C)	Mean d_p (μm)	V_{Slurry} (ml)	Thickness (mm)	k_1 (m^2)
65	52	-80	3,3	20	2,0	2,80$\times 10^{-14}$
50	68	-80	7,3	20	2,0*	2,96$\times 10^{-13}$
65	50	-30	6,2	20	2,0*	2,20$\times 10^{-13}$
65	50	-80	3,3**	18	1,6	2,40$\times 10^{-14}$
65	49	-80	3,3**	16	1,2	1,59$\times 10^{-14}$

Table 6.2: Summary of the main experimental conditions and the effects on porosity, mean pore size (d_p), and permeability (m^2).** mean pore size and * thickness of the tube not measured but considered equivalent to the sample frozen at -80°C, 65% solids loading, and 20 ml of volume of slurry (V_{Slurry}).

In Chapter 5, we measured the air permeability of ice-templeted monoliths without the porous isotropic layer. The permeability obtained in the present section (2,80$\times 10^{-14}$ m^2) is in agreement with those found in the monoliths for a similar pore size (3,3 μm) and pore volume (52 %) in section 5.1, therefore suggesting that the gas flow behavior of ice-templating tubes is ruled by the permeability of the part with unidirectional porosity instead of the isotropic one. Nonetheless, a more exhaustive study is required to validate this hypothesis.

Chapter 7

Conclusions and outlooks

7.1 Mechanical properties

This work reveals that the compressive behavior of unidirectional porous ceramics can be predicted by the honeycomb out-of-plane Ashby model in a wide porosity range, from 50% to 80%. However, the use of the model is limited to structures with a continuous array of unidirectional walls where buckling is the main failure mode. Further improvements of the model considering microstructural effects on the strength like the pore size reduction could lead to more accurate predictions.

Also, the mechanical reliability of ice-templated specimens was measured in compression in different pore structures through a Weibull analysis. Two fundamentally different fitting methods (OLS and Bayesian) have been successfully applied and give similar values for both m and σ_0. Further, the diagnostic parameters (R^2 and P-value) for both fitting methods indicate that the data is well described by Eq (2.3). Although the applicability of this method can be questioned due to the interactions between pores, we conclude from these results that the Weibull model and its underlying assumption that a single type of flaw dominates fracture behavior is valid for our samples.

We also observed that in ice-templated materials, strength and reliability (m) are properties that can be controlled independently. Weibull modulus exhibited a strong dependency on wall thickness caused by the reduction on the probability to find a catastrophic defect. Alternatively, the strength is mainly determined by the interlamellar porosity.

The possibility to aim for an specific strength (through $P(\%)_{inter}$) and tailor the Weibull modulus (through the wall thickness distribution) is a useful tool for porous materials in load bearing applications where it is required to combine a high reliability with mechanical stability. The capacity of ice-templating to tailor the percentage of inter- and intralamellar porosity individually provides a microstructural control that might be applied in biomedical and energy applications where both types of porosity are required [121]

[79] [122].

In addition, ice-templating exhibits a high versatility to quasi independently control the main pore descriptors (volume, size, and morphology). The possibility to aim for a specific porosity, and hence strength, (through the solids loading) and tailor the densification of the walls (through the sintering temperature) is a powerful tool to adjust the specific surface area of the walls while keeping a constant pore volume. This flexibility can be useful in applications like SOFC cathodes or tissue engineering scaffolds, where a sufficient amount of macroporosity (interlamellar porosity) is required to guide the flow of the fluid, coupled with intralamellar porosity to improve conversion efficiency [123] or cell proliferation [104].

7.2 Gas permeability

The gas permeability of ice-templated materials was evaluated as a function of different morphological parameters such as pore volume, size, and morphology. The results showed that pore size is the main parameter controlling the pressure drop and therefore of capital importance to increase the permeability of porous materials without a detrimental effect on the mechanical stability. Based on this knowledge we produced ice-templated samples with a 53% pore volume and a permeability equivalent to 72% pore volume. This reduction on total pore volume allowed to obtained samples with a high resistance coupled with a high permeability, two properties seemingly inversely related. The flexibility of ice-templating to control the microstructure allows us to tailor the mechanical and gas flow properties almost independently and consequently could be of potential application in products such as filters or catalytic supports. Finally, we also demonstrate that the permeability of unidirectional porous materials can be described by the capillary model in a wide porosity range. However, this study only covers the laminar regime and a deeper understanding of the microstructural effects of on a turbulent flow is still required in this type of material.

7.3 Ice-templated tubes

We developed a set-up to produce ice-templated tubes with an accurate control on pore volume, pore size, and overall thickness. Mechanical testing results showed a clear impact of pore volume and size on flexural and compressive strength, but results from radial crushing were inconclusive. Furthermore, the geometrical imperfections of the tube (eccentricity and warping) hinder the evaluation of tube thickness on mechanical properties. On the other hand, the permeability of tubes was successfully characterized, and we observed a high dependence on pore size. Therefore, higher performance of the

ice-templated tubular supports, particularly mechanical properties, is inevitably linked to a better control of the thickness of the tubes.

In addition, the formation of a hierarchical microstructure obtained with this set-up could be beneficial in applications such as SOFC, OTM, and water filtration, as it was reported by Moon et al. [116]. The external layer with finer and non-oriented porosity can facilitate the deposit of a dense layer and also increase the electrochemical reaction sites, while the unidirectional lamellar porosity allows the gas or liquid flow without an exaggerated increase in pressure drop.

7.4 Future work and perspectives

The work done in this thesis showed that it is possible to combine high permeability and strength through the optimization of the pore architecture. However, it just covered the porous substrate, and a lot of work still has to be done before the application of these anisotropic supports in OTM. Here, we summarize the most important points to address.

- **Screening for possible application.** With this thesis we provide a more detailed description of the microstructural effects on strength, reliability, and gas flow by identifying the appropriate models to describe the phenomena. This deeper understanding intends to provide a kind of toolbox for any application that require high mechanical stability and high permeability. Future work can be addressed using these guidelines and target microstructures for specific applications with porous materials.

- **Investigate an asymmetric membrane.** It is still necessary to deposit a dense layer on top of the ice-templated support to measure the oxygen permeation. In this way, we can assess the performance of the entire membrane in similar conditions to real applications. In the next few months, preliminary tests will be performed in CTF ice-templated supports.

- Additionally, we developed an experimental technique to produce asymmetric membranes with unidirectional porosity in one step. The technique is based on a regular ice-templating process with a modification of the cooling surface in contact with the slurry. Although the first tests are promising, as it shows Fig. 7.1, there are important drawbacks to be tackled such as homogeneity and tightness of the dense layer.

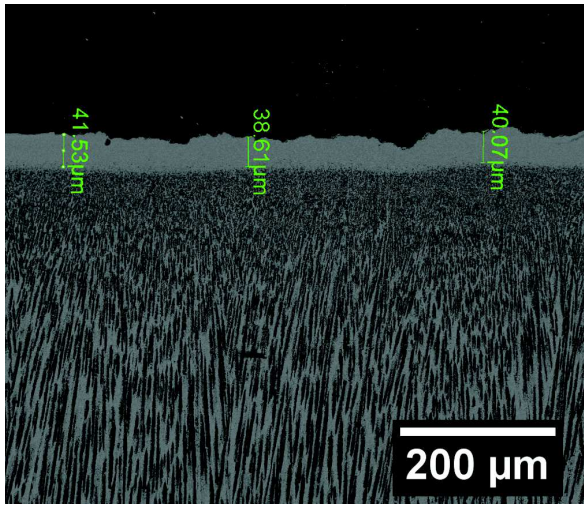

Figure 7.1: Cross section of an ice-templated support with a dense layer obtained in one-step.

- **Creep measuments.** Since these membranes are subjected to stresses at high temperature for long periods of time, creep becomes a major problem to solve. Literature on creep of porous materials is scarce, and in ice-templated nonexistent. A deeper understanding of the microstructural parameters that govern creep would be useful for applications any application that involves porous materials working at high temperature.

- **Improve strength in the weak direction.** In this work we have taken advantage of the high anisotropy exhibited by ice-templated materials. However, in some cases, like in a biaxial stress field, it is necessary to provide a minimum strength perpendicular to the pores. As it was pointed out in the section about mechanical properties, one possible solution could be increase the ceramic bridges between the principal walls to reinforce the structure and postpone buckling failure to higher stresses. The strategy to achieve this level of architectural control involve to explore new slurry formulations as it shows Fig. 7.2 where acetic acid and sucrose were used as an additives.

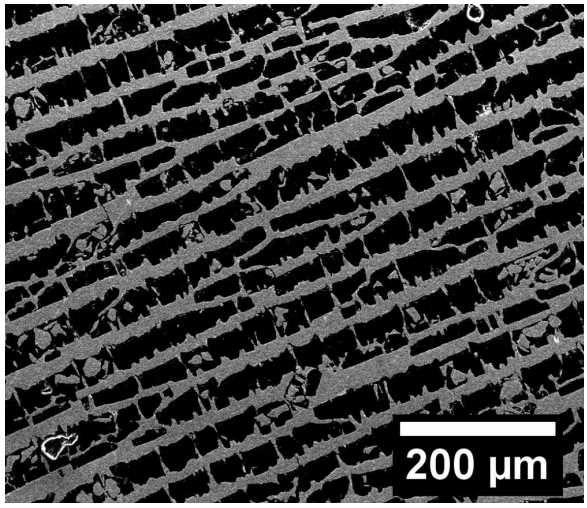

Figure 7.2: Detail of the increased population of ceramic bridges between the main struts.

- **Thickness control in ice-templated tubes.** One of the main drawbacks in the technique developed to ice-templated tubes (i.e. rotational freezing) is the lack of thickness control through the tube. Improvements on the set-up or modifications in the slurry composition (like increase the viscosity) could lead to a more accurate control on the thickness and thus, a better characterization of the tubes.

Bibliography

[1] P. Colombo, C. Vakifahmetoglu, and S. Costacurta. Fabrication of ceramic components with hierarchical porosity. *Journal of Materials Science*, 45(20):5425–5455, 2010.

[2] S. Baumann, W. A. Meulenberg, and H. P. Buchkremer. Manufacturing strategies for asymmetric ceramic membranes for efficient separation of oxygen from air. *Journal of the European Ceramic Society*, 33(7):1251–1261, 2013.

[3] S. Deville and A. J. Stevenson. Mapping ceramics research and its evolution. pages 1–15, 2015.

[4] C. Pekor, B. Groth, and I. Nettleship. The Effect of Polyvinyl Alcohol on the Microstructure and Permeability of Freeze-Cast Alumina. *Journal of the American Ceramic Society*, 93(1):115–120, 2010.

[5] M. Fukushima, M. Nakata, Y. Zhou, T. Ohji, and Y. Yoshizawa. Fabrication and properties of ultra highly porous silicon carbide by the gelation-freezing method. *Journal of the European Ceramic Society*, 30(14):2889–2896, 2010.

[6] S. Deville, E. Saiz, and A. P. Tomsia. Ice-templated porous alumina structures. *Acta Materialia*, 55(6):1965–1974, 2007.

[7] G. L. Messing and A. J. Stevenson. Materials science: Toward pore-free ceramics. *Science*, 322(5900):383–384, 2008.

[8] P. Colombo. In Praise of Pores. *Science*, 32(October):381–383, 2008.

[9] L. J. Gibson and M. F. Ashby. *Cellular solids. Structure and properties*. 1997.

[10] M. F. Ashby. The Mechanical Properties of Cellular Solids. *Metallurgical Transactions A*, 14(September):1755–1769, 1983.

[11] R. W. Rice. *Porosity of Ceramics*. 1998.

[12] R. W. Rice and W. R. Grace. Evaluation and extension of physical property-porosity models based on minimum solid area. *Journal of Materials Science*, 31:102–118, 1996.

[13] P. Colombo and M. Scheffer. *Cellular Ceramics: Structucture, Manufacturing, Properties and Applications*. Wiley Online Library, 2005.

[14] F. Lipperman, M. Ryvkin, and M. B. Fuchs. Fracture toughness of two-dimensional cellular material with periodic microstructure. *International Journal of Fracture*, 146(4):279–290, 2007.

[15] M. Vural and G. Ravichandran. Microstructural aspects and modeling of failure in naturally occurring porous composites. *Mechanics of Materials*, 35(3-5):523–536, 2003.

[16] A. P. Roberts and E. J. Garboczi. Elastic Properties of Model Porous Ceramics. *Journal of the American Ceramic Society*, 83(12):3041–3048, 2000.

[17] D. Jauffrès, C. L. Martin, A. Lichtner, and R. K. Bordia. Simulation of the toughness of partially sintered ceramics with realistic microstructures. *Acta Materialia*, 60(12):4685–4694, 2012.

[18] Z. Chen, X. Wang, F. Giuliani, and A. Atkinson. Microstructural characteristics and elastic modulus of porous solids. *Acta Materialia*, 89:268–277, 2015.

[19] R. W. Rice. Evaluating Porosity Parameters for Porosity-Property Relations. *Journal of the American Ceramic Society*, 76(7):1801–1808, 1993.

[20] L. J. Gibson. Modelling the Mechanical Behavior of Cellular Materials. *Materials Science and Engineering*, A110:1–36, 1989.

[21] M. F. Ashby. The properties of foams and lattices. *Phil. Trans. R. Soc. A*, 364:15–30, 2006.

[22] M. D. M. Innocentini, V. R. Salvini, and V. C. Pandolfelli. Assessment of Forchheimers Equation to Predict the Permeability of Ceramic Foams. *Journal of the American Ceramic Society*, 82(7):1945–1948, 1999.

[23] W. Sobieski and A. Trykozko. Sensitivity Aspects of Forchheimers Approximation. *Transport in Porous Media*, 89(2):155–164, 2011.

[24] D. Edouard, M. Lacroix, C. P. Huu, and F. Luck. Pressure drop modeling on SOLID foam: State-of-the art correlation. *Chemical Engineering Journal*, 144(2):299–311, 2008.

[25] J. Ahmed, C. Pham-Huu, and D. Edouard. A predictive model based on tortuosity for pressure drop estimation in slim and fat foams. *Chemical Engineering Science*, 66(20):4771–4779, 2011.

[26] E. A. Moreira, M. D. M. Innocentini, and J. R. Coury. Permeability of ceramic foams to compressible and incompressible flow. *Journal of the European Ceramic Society*, 24(10-11):3209–3218, 2004.

[27] M. D. M. Innocentini, V. R. Salvini, A. Macedo, and V. C. Pandolfelli. Prediction of Ceramic Foams Permeability Using Ergun Equation. *Materials Research*, 2(4):283–289, 1999.

[28] J. Comiti and M. Renaud. A new model for determining mean structure parameters of fixed beds from pressure drop measurements: application to beds packed with parallelepipedal particles. *Chemical Engineering Science*, 44(7):1539–1545, 1989.

[29] T. Ohji and M. Fukushima. Macro-porous ceramics: processing and properties. *International Materials Reviews*, 57(2):115–131, 2012.

[30] M. Fukushima, Y. Zhou, H. Miyazaki, Y. Yoshizawa, K. Hirao, Y. Iwamoto, S. Yamazaki, and T. Nagano. Microstructural characterization of porous silicon carbide membrane support with and without alumina additive. *Journal of the American Ceramic Society*, 89(5):1523–1529, 2006.

[31] Z. Deng, Ji. Yang, Y. Beppu, M. Ando, and T. Ohji. Effect of Agglomeration on Mechanical Properties of Porous Zirconia Fabricated by Partial Sintering. *Journal of the American Ceramic Society*, 85(8):1961–1965, 2002.

[32] A. R. Studart, U. T. Gonzenbach, E. Tervoort, and L. J. Gauckler. Processing Routes to Macroporous Ceramics: A Review. *Journal of the American Ceramic Society*, 89(6):1771–1789, 2006.

[33] M. D. M. Innocentini, P. Sepulveda, V. R. Salvini, V. C. Pandolfelli, and R. Coury. Permeability and Structure of Cellular Ceramics : A Comparison between Two Preparation Techniques. *Journal of the American Ceramic Society*, 81(12):3349–3352, 1998.

[34] K. Okada, T. Isobe, K. Katsumata, Y. Kameshima, A. Nakajima, and K. J. D. MacKenzie. Porous ceramics mimicking nature - preparation and properties of microstructures with unidirectionally oriented pores. *Science and Technology of Advanced Materials*, 12(6):064701, 2011.

[35] J. Dittmann and N. Willenbacher. Micro Structural Investigations and Mechanical Properties of Macro Porous Ceramic Materials from Capillary Suspensions. *Journal of the American Ceramic Society*, pages 1–6, 2014.

[36] S. Deville. Freeze-Casting of Porous Ceramics: A Review of Current Achievements and Issues. *Advanced Engineering Materials*, 10(3):155–169, 2008.

[37] E. Munch, E. Saiz, A. P. Tomsia, and S. Deville. Architectural Control of Freeze-Cast Ceramics Through Additives and Templating. *Journal of the American Ceramic Society*, 92(7):1534–1539, 2009.

[38] S. Deville, E. Maire, A. Lasalle, A. Bogner, C. Gauthier, J. Leloup, and C. Guizard. In Situ X-Ray Radiography and Tomography Observations of the Solidification of Aqueous Alumina Particle Suspensions-Part I: Initial Instants. *Journal of the American Ceramic Society*, 92(11):2489–2496, 2009.

[39] N. O. Shanti, K. Araki, and J. W. Halloran. Particle Redistribution During Dendritic Solidification of Particle Suspensions. *Journal of the American Ceramic Society*, 89(8):2444–2447, 2006.

[40] S. Deville, E. Saiz, and A. P. Tomsia. Freeze casting of hydroxyapatite scaffolds for bone tissue engineering. *Biomaterials*, 27(32):5480–9, 2006.

[41] S. Deville, E. Maire, A. Lasalle, A. Bogner, C. Gauthier, J. Leloup, and C. Guizard. In Situ X-Ray Radiography and Tomography Observations of the Solidification of Aqueous Alumina Particles Suspensions. Part II: Steady State. *Journal of the American Ceramic Society*, 92(11):2497–2503, 2009.

[42] J. Chen, G. Liu, and T. W. Button. Mechanical properties of porous TiO2 ceramics fabricated by freeze casting process. *Advances in Applied Ceramics*, 112(7):436–441, 2013.

[43] Y. Zhang, K. Zhou, J. Zeng, and D. Zhang. Control of pore structures and sizes in freeze cast ceramics. *Advances in Applied Ceramics*, 112(7):405–411, 2013.

[44] A. Z. Lichtner, D. Jauffrès, C. L. Martin, and R. K. Bordia. Processing of Hierarchical and Anisotropic Porosity LSM-YSZ Composites. *Journal of the American Ceramic Society*, 9, 2013.

[45] Sylvain Deville. Freeze-Casting of Porous Ceramics: A Review of Current Achievements and Issues. *Advanced Engineering Materials*, 10(3):155–169, mar 2008.

[46] S. Deville, E. Saiz, R. K. Nalla, and A. P. Tomsia. Freezing as a path to build complex composites. *Science*, 311(5760):515–8, 2006.

[47] S. M. Hashim, A. R. Mohamed, and S. Bhatia. Current status of ceramic-based membranes for oxygen separation from air. *Advances in colloid and interface science*, 160:88–100, 2010.

[48] P. Knauth and H. L. Tuller. Solid-State Ionics : Roots , Status , and Future Prospects. *Journal of the American Ceramic Society*, 85(7):1654–1680, 2002.

[49] J. Sunarso, S. Baumann, J. M. Serra, W. A. Meulenberg, S. Liu, Y. S. Lin, and J. C. D. da Costa. Mixed ionic electronic conducting (MIEC) ceramic-based membranes for oxygen separation. *Journal of Membrane Science*, 320:13–41, 2008.

[50] X. Chang, C. Zhang, Y. He, X. Dong, W. Jin, and N. Xu. A Comparative Study of the Performance of Symmetric and Asymmetric Mixed-conducting Membranes. *Chinese Journal of Chemical Engineering*, 17(4):562–570, jan 2009.

[51] S. Deville, C. Viazzi, and C. Guizard. Ice-structuring mechanism for zirconium acetate. *Langmuir*, 28(42):14892–8, 2012.

[52] J. Schindelin, I. Arganda-Carreras, E. Frise, V. Kaynig, M. Longair, T. Pietzsch, S. Preibisch, C. Rueden, S. Saalfeld, B. Schmid, J. Y. Tinevez, D. J. White, V. Hartenstein, K. Eliceiri, P. Tomancak, and A. Cardona. Fiji: an open-source platform for biological-image analysis. *Nature methods*, 9(7):676–82, 2012.

[53] K. Kwok, L. Kiesel, H. L. Frandsen, M. Søgaard, and P. V. Hendriksen. Strength characterization of tubular ceramic materials by flexure of semi-cylindrical specimens. *Journal of the European Ceramic Society*, 34(5):1423–1432, 2014.

[54] J. Han, C. Hong, X. Zhang, J. Du, and W. Zhang. Highly porous ZrO2 ceramics fabricated by a camphene-based freeze-casting route: Microstructure and properties. *Journal of the European Ceramic Society*, 30(1):53–60, 2010.

[55] C. Hong, X. Zhang, J. Han, J. Du, and W. Han. Ultra-high-porosity zirconia ceramics fabricated by novel room-temperature freeze-casting. *Scripta Materialia*, 60(7):563–566, 2009.

[56] L. Hu and C. A. Wang. Effect of sintering temperature on compressive strength of porous yttria-stabilized zirconia ceramics. *Ceramics International*, 36(5):1697–1701, 2010.

[57] K. Zuo, Y. Zeng, and D. Jiang. Properties of Microstructure-Controllable Porous Yttria-Stabilized Ziroconia Ceramics Fabricated by Freeze Casting. *International Journal of Applied Ceramic Technology*, 5(2):198–203, 2008.

[58] G. Liu and T. W. Button. The effect of particle size in freeze casting of porous alumina-zirconia composite. *Ceramics International*, 39(7):8507–8512, 2013.

[59] M. M. Porter, R. Imperio, M. Wen, M. A. Meyers, and J. McKittrick. Bioinspired Scaffolds with Varying Pore Architectures and Mechanical Properties. *Advanced Functional Materials*, 24(14):1978–1987, 2014.

[60] S. Deville. Freeze-Casting of Porous Biomaterials: Structure, Properties and Opportunities. *Materials*, 3(3):1913–1927, 2010.

[61] T. Fukasawa, Z. Y. Deng, M. Ando, T. Ohji, and Y. Goto. Pore structure of porous ceramics synthesized from water-based slurry by freeze-dry process. *Journal of Materials Science*, 36(10):2523–2527, 2001.

[62] Y. H. Koh, I. K. Jun, J. J. Sun, and H. E. Kim. In situ Fabrication of a Dense/Porous Bi-layered Ceramic Composite using Freeze Casting of a Ceramic-Camphene Slurry. *Journal of the American Ceramic Society*, 89(2):763–766, 2006.

[63] K. Araki and J. W. Halloran. New freeze-casting technique for ceramics with sublimable vehicles. *Journal of the American Ceramic Society*, 87(10):1859–1863, 2004.

[64] L. Hu, C. A. Wang, Y. Huang, C. Sun, S. Lu, and Z. Hu. Control of pore channel size during freeze casting of porous YSZ ceramics with unidirectionally aligned channels using different freezing temperatures. *Journal of the European Ceramic Society*, 30(16):3389–3396, 2010.

[65] R. Liu, J. Yuan, and C. A. Wang. A novel way to fabricate tubular porous mullite membrane supports by TBA-based freezing casting method. *Journal of the European Ceramic Society*, 2013.

[66] R. Chen, C. A. Wang, Y. Huang, L. Ma, and W. Lin. Ceramics with special porous structures fabricated by freeze-gelcasting: Using tert-butyl alcohol as a template. *Journal of the American Ceramic Society*, 90(11):3478–3484, 2007.

[67] M. Naviroj, S. M. Miller, P. Colombo, and K. T. Faber. Directionally aligned macroporous SiOC via freeze casting of preceramic polymers. *Journal of the European Ceramic Society*, 35(8):2225–2232, 2015.

[68] S. W. Sofie. Fabrication of Functionally Graded and Aligned Porosity in Thin Ceramic Substrates With the Novel Freeze?Tape-Casting Process. *Journal of the American Ceramic Society*, 90(7):2024–2031, 2007.

[69] J. Zhang and M. F. Ashby. The out-of-plane properties of honeycombs. *International Journal of Mechanical Sciences*, 34(6):475–489, 1992.

[70] A. Ojuva, M. Järveläinen, M. Bauer, L. Keskinen, M. Valkonen, F. Akhtar, E. Levänen, and L. Bergström. Mechanical performance and CO 2 uptake of ion-exchanged zeolite A structured by freeze-casting. *Journal of the European Ceramic Society*, 35(9):2607–2618, 2015.

[71] P. M. Hunger, A. E. Donius, and U. G. K. Wegst. Structure-property-processing correlations in freeze-cast composite scaffolds. *Acta biomaterialia*, 9(5):6338–48, 2013.

[72] S. Meille, M. Lombardi, J. Chevalier, and L. Montanaro. Mechanical properties of porous ceramics in compression : On the transition between elastic , brittle , and cellular behavior. *Journal of the European Ceramic Society*, 32(15):3959–3967, 2012.

[73] W. Acchar, F. B. M. Souza, E. G. Ramalho, and W. L. Torquato. Mechanical characterization of cellular ceramics. *Materials Science and Engineering: A*, 513-514:340–343, 2009.

[74] R. Brezny and D.J. Green. Factors Controlling the Fracture Resistance of Brittle Cellular Materials. *Journal of the American Ceramic Society*, 74(5):1061–1065, 1991.

[75] C. Q. Dam, R. Brezny, and D. J. Green. Compressive behavior and deformation-mode map of an open. *Journal of Materials Research*, 5(1):163–171, 1990.

[76] C. R. Rambo, T. Andrade, T. Fey, H. Sieber, E. Martinelli, and P. Greil. Microcellular Al2O3 Ceramics from Wood for Filter Applications. *Journal of the American Ceramic Society*, 91(3):852–859, 2008.

[77] T. Isobe, Y. Kameshima, A. Nakajima, K. Okada, and Y. Hotta. Gas permeability and mechanical properties of porous alumina ceramics with unidirectionally aligned pores. *Journal of the European Ceramic Society*, 27(1):53–59, 2007.

[78] J. Bauer, S. Hengsbach, I. Tesari, R. Schwaiger, and O. Kraft. High-strength cellular ceramic composites with 3D microarchitecture. *Proceedings of the National Academy of Sciences*, 111(7):2453–2458, 2014.

[79] Q. Fu, E. Saiz, M. N. Rahaman, and A. P. Tomsia. Toward Strong and Tough Glass and Ceramic Scaffolds for Bone Repair. *Advanced Functional Materials*, pages 1–16, 2013.

[80] P. Colombo. Macro- and micro-cellular porous ceramics from preceramic polymers. *Composites Science and Technology*, 63(16):2353–2359, 2003.

[81] M. Genet, M. Houmard, S. Eslava, E. Saiz, and A. P. Tomsia. A two-scale Weibull approach to the failure of porous ceramic structures made by robocasting: Possibilities and limits. *Journal of the European Ceramic Society*, 33(4):679–688, 2012.

[82] R. Brezny and D. J. Green. The effect of cell size on the mechanical behavior of cellular materials. *Acta Metallurgica et Materialia*, 38(12):2517–2526, 1990.

[83] A. Z. Lichtner, D. Roussel, D. Jauffrès, C. L. Martin, and R. K. Bordia. Effect of Macro-Pore Anisotropy on the Mechanical Properties of Porous Ceramics. *Journal of the American Ceramic Society*, pages 1–9, 2015.

[84] A. Ojuva. *Processing and performance of zeolites for efficient carbon dioxide separation*. PhD thesis, 2015.

[85] W. Li, M. M. Porter, E. A. Olevsky, R. M. German, and J. Mckittrick. Sintering of bi-porous titanium dioxide scaffolds: Experimentation, modeling and simulation. *Materials Science & Engineering A*, 636(11):148–156, 2015.

[86] C. Lu, R. Danzer, and F. Fischer. Fracture statistics of brittle materials: Weibull or normal distribution. *Physical Review E*, 65(6):067102, 2002.

[87] R. H. Doremus. Fracture statistics: A comparison of the normal, weibull, and type i extreme value distributions. *Journal of applied physics*, 54(1):193–198, 1983.

[88] W. Weibull. A Statistical Distribution Function of Wide Applicability. *Journal of Applied Mechanics*, page 7, 1951.

[89] F. F. Lange. Powder Processing Science and Technology for Increased Reliability. *Journal of the American Ceramic Society*, 72(1):3–15, 1989.

[90] X. Fan, E. D. Case, I. Gheorghita, and M. J. Baumann. Weibull modulus and fracture strength of highly porous hydroxyapatite. *Journal of the mechanical behavior of biomedical materials*, 20:283–95, 2013.

[91] X. Zhu, D. Jiang, and S. Tan. Preparation of silicon carbide reticulated porous ceramics. *Materials Science and Engineering A*, 323(1-2):232–238, 2002.

[92] P. Miranda, A. Pajares, E. Saiz, A. P. Tomsia, and F. Guiberteau. Mechanical properties of calcium phosphate scaffolds fabricated by robocasting. *Journal of Biomedical Materials Research - Part A*, 85(1):218–227, 2008.

[93] R. Danzer. A general strength distribution function for brittle materials. *Journal of the European Ceramic Society*, 10(6):461–472, 1992.

[94] F. Pernot, P. Etienne, F. Boschet, and L. Datas. Weibull Parameters and the Tensile Strength of Porous Phosphate Glass-Ceramics. *Journal of the American Ceramic Society*, 48(3):641–648, 1999.

[95] S. C. Nanjangud, R. Brezny, and D. J. Green. Strength and Young‘s Modulus Behavior of a Partially Sintered Porous Alumina. *Journal of the American Ceramic Society*, 78(1):266–268, 1995.

[96] X. Fan, E. D. Case, F. Ren, Y. Shu, and M. J. Baumann. Part I: porosity dependence of the Weibull modulus for hydroxyapatite and other brittle materials. *Journal of the mechanical behavior of biomedical materials*, 8:21–36, 2012.

[97] R. Brezny and D. J. Green. Fracture Behavior of Open-Cell Ceramics. *Journal of American Ceramic Society*, 72(7):1145–1152, 1989.

[98] K. Miled, K. Sab, and R. Le Roy. Particle size effect on EPS lightweight concrete compressive strength: Experimental investigation and modelling. *Mechanics of Materials*, 39(3):222–240, 2007.

[99] D. M Liu. Influence of Porosity and Pore Size on the Compressive Strength of Porous Hydroxyapatite Ceramic. *Ceramics International*, 23:135–139, 1997.

[100] J. C. Le Huec, T. Schaeverbeke, D. Clement, J. Faber, and A. Le Rebeller. Influence of porosity on the mechanical resistance of hydroxyapatite ceramics under compressive stress. *Biomaterials*, 16(2):113–8, 1995.

[101] Y. M. Chiang, W. D. Kingery, and D. P. Birnie. *Physical ceramics: principles for ceramic science and engineering*. J. Wiley, 1997.

[102] X. Fan, E. D. Case, F. Ren, Y. Shu, and M. J. Baumann. Part II: fracture strength and elastic modulus as a function of porosity for hydroxyapatite and other brittle materials. *Journal of the mechanical behavior of biomedical materials*, 8:99–110, 2012.

[103] I. Sabree, J. E. Gough, and B. Derby. Mechanical properties of porous ceramic scaffolds: Influence of internal dimensions. *Ceramics International*, 41(7):8425–8432, 2015.

[104] B. S. M. Seeber, U. T. Gonzenbach, and L. J. Gauckler. Mechanical properties of highly porous alumina foams. *Journal of Materials Research*, 28(17):1–7, 2013.

[105] J. M. Cordell, M. L. Vogl, and A. J. Wagoner Johnson. The influence of micropore size on the mechanical properties of bulk hydroxyapatite and hydroxyapatite scaffolds. *Journal of the Mechanical Behavior of Biomedical Materials*, 2(5):560–570, 2009.

[106] L. Biasetto, P. Colombo, M. D. M. Innocentini, and S. Mullens. Gas Permeability of Microcellular Ceramic Foams. *Ind. Eng. Chem. Res.*, 46:3366–3372, 2007.

[107] M. D. M. Innocentini, R. K. Faleiros, R. Pisani, I. Thijs, J. Luyten, and S. Mullens. Permeability of porous gelcast scaffolds for bone tissue engineering. *Journal of Porous Materials*, 17(5):615–627, 2010.

[108] W. Acchar, E. G. Ramalho, F. B. M. Souza, W. L. Torquato, V. P. Rodrigues, and M. D. M. Innocentini. Characterization of cellular ceramics for high-temperature applications. *Journal of Materials Science*, 43(19):6556–6561, 2008.

[109] S. Ergun. Fluid flow through packed columns. *Chemical engineering progress*, 48, 1952.

[110] M. Lacroix, P. Nguyen, D. Schweich, C. Pham Huu, S. Savin-Poncet, and D. Edouard. Pressure drop measurements and modeling on SiC foams. *Chemical Engineering Science*, 62(12):3259–3267, 2007.

[111] Z. Hu and K. Lu. Evolution of Pores and Tortuosity During Sintering. *Journal of the American Ceramic Society*, 4:n/a–n/a, 2014.

[112] Y. Zhou, M. Fukushima, H. Miyazaki, Y. Yoshizawa, K. Hirao, Y. Iwamoto, and K. Sato. Preparation and characterization of tubular porous silicon carbide membrane supports. *Journal of Membrane Science*, 369(1-2):112–118, 2011.

[113] Y. Dong, X. Feng, D. Dong, S. Wang, J. Yang, J. Gao, X. Liu, and G. Meng. Elaboration and chemical corrosion resistance of tubular macro-porous cordierite ceramic membrane supports. *Journal of Membrane Science*, 304(1-2):65–75, 2007.

[114] M. B. Choi, D. K. Lim, S. Y. Jeon, H. S. Kim, and S. J. Song. Oxygen permeation properties of bscf5582 tubular membrane fabricated by the slip casting method. *Ceramics International*, 38(3):1867–1872, 2012.

[115] K. H. Kim, S. J. Cho, K. J. Yoon, J. J. Kim, J. W. Ha, and D. I. Chun. Centrifugal casting of alumina tube for membrane application. *Journal of Membrane Science*, 199(1):69–74, 2002.

[116] Y. Dong, J. Zhou, B. Lin, Y. Wang, S. Wang, L. Miao, Y. Lang, X. Liu, and G. Meng. Reaction-sintered porous mineral-based mullite ceramic membrane supports made from recycled materials. *Journal of hazardous materials*, 172(1):180–186, 2009.

[117] J. W. Moon, H. J. Hwang, M. Awano, and K. Maeda. Preparation of NiO-YSZ tubular support with radially aligned pore channels. *Materials Letters*, 57:1428–1434, 2003.

[118] S. Deville, E. Maire, A. Lasalle, A. Bogner, C. Gauthier, J. Leloup, and C. Guizard. Influence of particle size on ice nucleation and growth during the ice-templating process. *Journal of the American Ceramic Society*, 93(9):2507–2510, 2010.

[119] J. A. Hudson. Tensile strength and the ring test. *International Journal of Rock Mechanics and Mining Sciences & Geomechanics Abstracts*, 6(1):91–97, 1969.

[120] K. Kwok, H. L. Frandsen, M. Søgaard, and P. V. Hendriksen. Mechanical reliability of geometrically imperfect tubular oxygen transport membranes. *Journal of Membrane Science*, 470:80–89, 2014.

[121] K. Kwok, H. L. Frandsen, M. Søgaard, and P. V. Hendriksen. Stress analysis and fail-safe design of bilayered tubular supported ceramic membranes. *Journal of Membrane Science*, 453:253–262, 2014.

[122] A. J. Wagoner-Johnson and B. A. Herschler. A review of the mechanical behavior of CaP and CaP/polymer composites for applications in bone replacement and repair. *Acta biomaterialia*, 7(1):16–30, 2011.

[123] D. L. Douglas and H. A. Liebhafsky. Fuel cells: History, operation, and applications. *Physics Today*, 13(6):26–30, 2009.

[124] E. S. Greene, W. K.S. Chiu, and M. G. Medeiros. Mass transfer in graded microstructure solid oxide fuel cell electrodes. *Journal of Power Sources*, 161(1):225–231, 2006.

List of Figures

List of Tables